Magnetocaloric Materials

Jeppesen, Stinus

Publication date:
2008

Document Version
Publisher's PDF, also known as Version of record

Risø DTU
National Laboratory
for Sustainable Energy

Magnetocaloric Materials

Stinus Jeppesen

Risø-PhD-43(EN)

Risø National Laboratory for Sustainable Energy
Technical University of Denmark
Roskilde, Denmark
Publication date October 2008

Author: Stinus Jeppesen
Title: Magnetocaloric Materials
Division: Fuel Cells and Solid State Chemistry Division

This thesis is submitted in partial fulfillment of the requirements for the Ph.D. degree at The University of Copenhagen

Abstract:
New and improved magnetocaloric materials are one of the cornerstones in the development of room temperature magnetic refrigeration. Magnetic refrigeration has been used since the 1930's in cryogenic applications, but has since the discovery of room temperature refrigerants received enormous attention. This Ph.D. work has been mainly concerned with developing a new technique to characterize the magnetocaloric effect (MCE) and using this technique in the investigations on new and improved magnetocaloric materials. For this purpose a novel differential scanning calorimeter (DSC) with applied magnetic fields was developed for measuring heat capacity as function of magnetic field. Measurements using the developed DSC demonstrate a very high sensitivity, fast measurements and good agreement with results obtained by other techniques.
Furthermore, two material systems have been described in this work. Both systems take basis in the mixed-valence manganite system $La_{1-x}Ca_xMnO_3$ well known from research on colossal magnetoresistance (CMR). The mixed-valence manganite crystallizes in the perovskite structure of general formula ABO_3. The first material system is designed to investigate the influence of low level Cu doping on the B-site. Six different samples were prepared with over-stoichiometric compositions $La_{0.67}Ca_{0.33}Mn_{1.05}Cu_xO_3$, x=0, 1, 2, 3, 4 and 5%. All compositions crystallized well in the same perovskite structure, but the morphology of the samples changed drastically with doping. Investigation on the magnetocaloric properties revealed that small levels of Cu up to around 3% could improve the magnetocaloric performance of the materials. Furthermore, Cu could be used to tune the temperature interval without deteriorating the MCE, which is a much desired characteristic for potential use in magnetic refrigerators.
A less comprehensive part of the work has been concerned with the investigation of doping on the A-site in the structure. The possibility of substituting the lanthanum content of the material with a lanthanide mix (Ln) consisting of La, Ce, Nd and Pr was investigated due to the potential of making more cost-effective materials.
Four samples with compositions $(La_{1-x}Ln_x)_{0.67}Ca_{0.33}Mn_{1.05}O_3$ with x=0, 0.33, 0.67 and 1.00, were synthesized to investigate the effect on the magnetocaloric properties. It was found that the perovskite structure could be maintained even at the highest level of doping (x=1.00), and that the maximum magnetic entropy change, ΔS_M, quantifying the magnetocaloric effect was actually enhanced to an optimum at x=0.67. Furthermore, the relative cooling power (RCP) was calculated for this series, and it was demonstrated that RCP increases continuously with doping and reaches the highest value in the composition, where the entire lanthanum content has been replaced by the lanthanide mix. These observations make promise of compositions, which could be competitive both in terms of cost-effectiveness and MCE. The work on the latter materials have been disclosed in a US and UK patent application.

Published on www.risoe.dtu.dk in February 2010

Risø-PhD-43(EN)
October 2008

ISBN 978-87-550-3706-9

Group's own reg. no.: 1960004-00
(psp number)

Sponsorship:
Risø National Laboratory

Cover :

Pages: 172
Tables: 4
References: 93

Information Service Department
Risø National Laboratory for
Sustainable Energy
Technical University of Denmark
P.O.Box 49
DK-4000 Roskilde
Denmark
Telephone +45 46774004
bibl@risoe.dk
Fax +45 46774013
www.risoe.dtu.dk

Magnetocaloric Materials

Stinus Jeppesen

University of Copenhagen

&

Fuel Cells and Solid State Chemistry Division
Risø DTU

October 2008

Published by:
Risø DTU

Fuel Cells and Solid State Chemistry Division
Risø DTU
The Technical University of Denmark - DTU
Building 228, P.O. Box 49
DK-4000 Roskilde
Denmark
Tel +45 4677 5800
Fax +45 4677 5858
web: http://www.risoe.dtu.dk

Publication Reference Data:
Jeppesen, S.
Magnetocaloric Materials.
Ph.D. Thesis
Risø DTU, Fuel Cells and Solid State Chemistry Division
The Technical University of Denmark - DTU
October 2008
Report number. Risø-PhD-43(EN)
ISBN 978-87-550-3706-9
Keywords: magnetic refrigeration, magnetocaloric materials, differential scanning colorimetry, experimental validation.

Preface

This thesis was prepared at the Fuel Cells and Solid State Chemistry Division of Denmark (DTU) and submitted in partial fulfillment of the requirements for obtaining the Ph.D. degree at the Niels Bohr Institute, University of Copenhagen. The work was financed by Risø National Laboratory and lasted from January 2005 to October 2008.
The Ph.D. project was supervised by Prof. Robert Feidenhans'l from the Niels Bohr Institute, University of Copenhagen, Prof. S. Linderoth, Dr. N. H. Pryds and Dr. L. Theil Kuhn from the Fuel Cells and Solid State Chemistry Division, Risø, DTU.
The thesis describes the development of a new measuring technique that allows to perform differential scanning calorimetry measurements (DSC) of magnetocaloric materials in applied magnetic fields. These measurements are performed in order to evaluate the magnetocaloric effect (MCE) of materials intended to be used in room-temperature magnetic refrigeration devices. The thesis furthermore describes the class of ceramic materials called mixed-valence manganites of which two specific series of compositions have been synthesized and characterized using different characterization techniques. One of the composition series has been disclosed in a patent application filed to the US and UK Patent Offices.
I owe my supervisors Prof. S. Linderoth, Dr. N. H. Pryds and Dr. L. Theil Kuhn and Prof. Robert Feidenhans'l a dept of gratitude for their strong support and encouragement throughout the recent years. I would also like to especially thank my "co-supervisor" Dr. C.R.H. Bahl for countless discussions and help on a wide variety of issues concerning this work. I would also like to thank the magnetic refrigeration group my nearest colleagues Anders, Thomas, Jørgen, Kristian, Britt, Inge, Kaspar, Kurt, Niels and Jesper, the great technicians and

engineers Jens, Jørgen, Ole, Carsten, Niels and Bjørn, my helpers in the lab Charlotte, Ebtisam and Annelise, my scientific helpers Christos, Karsten, Mogens, Nikos, Finn Willy, Ming, Peter and Anders.
For help on preparation of the manuscript I would like to thank Britt, Katrine, Luise, Nini, Christian, Søren, Mohan and Niels.
Finally, I would like to extend my deepest gratitude to my family especially my wife Katrine for being very understanding and patient during the stressed periods of the past three years maybe particularly the last couple of months. Since both of our boys were born into their father being a Ph.D. student, I guess they don't know any better, but they certainly still supported me more than I can describe here.

Stinus Jeppesen, Roskilde, September 2007

Abstract

New and improved magnetocaloric materials are one of the cornerstones in the development of room temperature magnetic refrigeration. Magnetic refrigeration has been used since the 1930's in cryogenic applications, but has since the discovery of room temperature refrigerants received enormous attention. This Ph.D. work has mainly been concerned with developing a new technique to characterize the magnetocaloric effect and using this technique in the investigations on new and improved magnetocaloric materials. For this purpose a novel differential scanning calorimeter (DSC) with applied magnetic fields was developed for measuring heat capacity as function of magnetic field. Measurements using the developed DSC demonstrate a very high sensitivity, fast measurements and good agreement with results obtained by other techniques.

Furthermore, two material systems have been described in this work. Both systems take basis in the mixed-valence manganite system $La_{1-x}Ca_xMnO_3$ well known from research on colossal magnetoresistance (CMR). The mixed-valence manganite crystallize in the perovskite structure of general formula ABO_3. The first material system is designed to investigate the influence of low level Cu doping on the B-site. Six different samples were prepared with compositions $La_{0.67}Ca_{0.33}Mn_{1.05}Cu_xO_3$, x=0, 1, 2, 3, 4 and 5%. All compositions crystallized well in the same perovskite structure, but the morphology of the samples changed drastically with doping. Investigation on the magnetocaloric properties revealed that small levels of Cu up to around 3% could improve the magnetocaloric performance of the materials. Furthermore, Cu could be used to tune the working temperature interval of the refrigerant without deteriorating the effect, which is a very desired characteristic for potential use in refrigerators.

A less comprehensive part of the work investigated substitution of the A-site ions. The possibility of substituting the lanthanum content of the material

with a lanthanide mix consisting of La, Ce, Nd and Pr was investigated due to the potential of making more cost-effective materials. Four samples with compositions $(La_{1-x}(La,Ce,Pr,Nd)_x)_{0.67}Ca_{0.33}Mn_{1.05}O_3$, x=0, 0.33, 0.67 and 1 were synthesized to investigate the magnetocaloric properties of these compositions. It was found that the perovskite structure could be maintained even at the highest level of doping (x=1), and that the maximum magnetic entropy change, ΔS_M, quantifying the magnetocaloric effect was actually enhanced to an optimum at x=0.67. Furthermore, the relative cooling power (RCP) of the materials were investigated, and it was demonstrated that RCP increases continuously with doping and reaches the highest value in the composition, where the entire lanthanum content has been replaced by the lanthanide mix. These observations make promise of compositions, which could be competitive both in terms of cost-effectiveness and MCE. The work on the latter materials have been disclosed in a US and UK patent application.

Resumé

Nye og forbedrede magnetokaloriske kølematerialer er en af hjørnestenene i udviklingen af magnetisk køling ved stuetemperatur. Magnetisk køling er blevet anvendt siden 1930'erne i det kryogene temperaturområde, men efter opdagelsen af magnetisk køling ved stuetemperatur har dette område været i kraftig vækst. Dette Ph.D. arbejde har beskæftiget sig med udviklingen af en ny måleteknik til at karakterisere den magnetokaloriske effekt, samt efterfølgende at bruge denne teknik i udviklingen af nye og forbedrede kølematerialer til magnetisk køling. Til dette formål er der blevet udviklet et nyt differentielt skannende kalorimeter (DSC) med mulighed for at måle i et påtrykt magnetfelt. Målinger med den udviklede DSC har bevist at måleteknikken har en væsentlig bedre følsomhed end kommercielle DSC udstyr, samt en hurtig bestemmelse af materialers varmekapacitet som funktion af felt, der er i god overensstemmelse med andre teknikker. Derudover er to forskellige materialesystemer blevet beskrevet. Begge systemer tager udgangspunkt i de ferromagnetiske calcium substituerede lanthan-mangan oxider. Calcium substitutionen inducerer mangan ioner med blandet valens, der er årsagen til den ferromagnetiske kobling i disse materialer. Materialerne har siden 1990'erne været kendt som CMR materialer (Colossal Magnetoresistance Materials) pga. deres usædvanligt høje magnetoresistansværdi. Disse oxider krystalliserer i den såkaldte perovskit struktur med den generelle formel ABO_3. Den første materialeserie er designet til at undersøge effekten af at dope kobber ioner ind på mangans plads i strukturen på B-pladsen. Til dette formål blev der syntiseret seks forskellige prøver med sammensætning $La_{0.67}Ca_{0.33}Mn_{1.05}Cu_xO_3$, x=0, 1, 2, 3, 4 og 5%. Alle prøver krystalliserede i den ønskede perovskit struktur, men morfologien i prøverne ændrede sig væsentligt som følge af doping. Undersøgelser af prøvernes magnetokaloriske egenskaber viste at små mængder af kobberi-

oner kunne forbedre materialernes magnetokaloriske effekt. Derudover er det også blevet påvist, at små mængder af kobberioner kan bruges til at ændre kølematerialets arbejdstemperatur uden at nedsætte eller ødelægge køleeffekten. Denne egenskab er meget eftertragtet for magnetiske kølematerialer. En mindre del af arbejdet har omhandlet undersøgelsen af substitution på A-pladsen i strukturen. Muligheden for at bytte lanthan indholdet ud med en mindre raffineret grad af lanthan er blevet undersøgt. Den mindre raffinerede lanthan består af en lanthanid (Ln) blanding, der udover lanthan også indeholder cerium, praseodymium og neodymumium. Dette ønskes undersøgt pga. den omkostningsreduktion på materialeprisen, der kunne følge. Fire sammensætninger blev syntiseret for at undersøge disse materialers magnetokaloriske egenskaber $(La_{1-x}(La,Ce,Pr,Nd)_x)_{0.67}Ca_{0.33}Mn_{1.05}O_3$ for x=0, 0.33, 0.67 og 1. Alle sammensætningerne krystalliserede fint i den ønskede perovskit struktur selv i den fuldt substituerede sammensætning (x=1.00). Ydermere findes det, at den magnetiske entropiændring, ΔS_M, der er et udtryk for størrelsen af den magnetokaloriske effekt, blev forbedret som følge af substitution. Den magnetokaloriske effekt nåede et optimum ved 67% substitution af lanthan med den blandede lanthanid sammensætning. Derudover viste en udregning af den relative kølekapacitet (RCP) for disse materialer, at kølekapaciteten steg kontinuert som funktion af denne substituering og opnåede den maksimale værdi i den fuldt substituerede sammensætning. Disse iagttagelser giver grund til at tro, at disse materialer kunne blive konkurrencedygtige som magnetokaloriske kølematerialer både mht. pris og ydelse. Arbejdet med de sidstnævnte materialer er indeholdt i en patent ansøgning indsendt til det amerikanske og det engelske patentkontor.

Notation

List of Symbols

Symbol	Name	Unit
2θ	Diffraction angle	Degrees (°)
a,b,c	Lattice parameters	nm
C	Specific heat	$Jkg^{-1}K^{-1}$
C_P	Specific heat at constant pressure	$Jkg^{-1}K^{-1}$
H	Applied magnetic field (μ_0H)[1]	Tesla (T)
M	Magnetization	$Am^{-1}kg^{-1}$
r_A	Radius of the A-site cations	nm
r_B	Radius of the B-site cations	nm
r_O	Radius of the oxygen ion	nm
$\langle r_A \rangle$	Average radius of the A-site cations	nm
$\langle r_B \rangle$	Average radius of the B-site cations	nm
t*	Goldschmith tolerance factor	Dimensionless
T	Temperature	K
T_C	Curie temperature of a ferromagnet	K
x	Level ion doping (Cu or Ln (La, Ce, Pr, Nd))	Dimensionless

[1] In vacuum the applied field or the magnetic flux density $\mathbf{B}=\mu_0\mathbf{H}$. For simplicity the applied magnetic field is written as H in units of Tesla.

Abbreviations

Abbreviation	Meaning
AF	AntiFerromagnet
CMR	Colossal MagnetoResistance
CO	Charge Ordered
DE	Double Exchange
DSC	Differential Scanning Calorimetry
FM	FerroMagnet
FI	Ferromagnetic Insulator
FOMT	First Order Magnetic Transitions
FWHM	Full Width at Half Maximum
GMR	Giant MagnetoResistance
JT	Jahn-Teller
MCE	Magnetocaloric Effect
MIT	Massachusetts Institute of Technology
MR	Magneto Resistance
Pbnm	Spacegroup no. 62[2]
PLD	Pulsed Laser Deposition
SOFC	Solid Oxide Fuel Cells
SOMT	Second Order Magnetic Transitions
TS	Temperature-Entropy (diagram)
VSM	Vibrating Sample Magnetometer
XRD	X-Ray Diffraction

[2]International Tables of Crystallography. Spacegroup no. 62. Link: http://it.iucr.org/-Ab/ch7o1v0001/sgtable7o1o062.pdf

Contents

List of Figures

CHAPTER 1

Introduction
- what is it all about

Magnetic refrigeration goes back more than 100 years. As early as 1881 Warburg [1] discovered the magnetocaloric effect in iron, but it wasn't explained theoretically until 1918 by Weiss & Piccard [2] and the room-temperature regime was not investigated for many years after the discovery. The principle of adiabatic demagnetization was demonstrated by Debye and Giauque [3, 4] in 1926-27 and Giauque received the Nobel prize in 1949 for his work. Since Giauque and MacDougall in 1935 [5] used the magnetocaloric effect to cool gadolinium sulphate from 1.5 K to 0.25 K, adiabatic demagnetization has been used to obtain very low temperatures in different applications. One of the most widespread uses of the technique has been in helium liquefaction industries.
In 1976, Brown constructed the first room-temperature magnetic refrigeration system [6] using gadolinium as magnetic refrigerant. Since Brown demonstrated refrigeration by adiabatic demagnetization in the room-temperature range, the field of room-temperature magnetic refrigeration has evolved drastically. With the discovery of giant magnetocaloric materials in the 90's, the potential of magnetic refrigeration becoming an alternative to conventional vapor-compression based refrigeration technologies led to even larger efforts being put into the field. Vapor-compression have been the leading technology for the last century after outcompeting natural ice as the primary source of refrigeration [7]. Vapor-compression is today a reliable and low-cost technology, but possible improvements are limited. With modern society relying more and more on available cooling and a contemporary increased focus on the environment, there

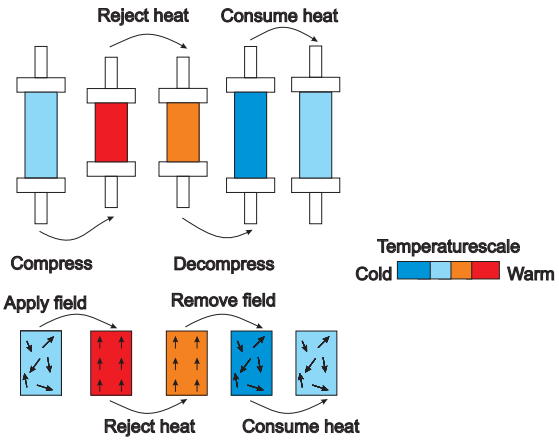

Figure 1.1: Four schematic cycles of refrigeration using vapor compression (top panel) or magnetic refrigeration (bottom panel). In this representation the analogue cycle steps in the two different refrigeration methods are easily recognized. The color coding of the refrigerant temperature is shown to the right on the temperature scale.

has been a driving force towards development of new and more energy-efficient technologies. This has caused an increased interest in this type of refrigeration over the last decade. Not only the possibility of being more energy-efficient is ecologically attractive, but also the use of chlorofluorocarbons (CFCs) and hydrochlorofluorocarbons (HCFCs) as working fluids in conventional refrigeration technology has raised serious environmental concerns. CFCs are now prohibited and HCFCs will be prohibited around 2010[8]. Even marginal efforts in reducing power consumption in household and industrial refrigeration will have a large economic and ecological impact due to the size of this area. Around 15% of the total energy consumption worldwide is used for refrigeration purposes [9].

1.1 Magnetic Refrigeration

Magnetic refrigeration is refrigeration by use of the magnetocaloric effect (MCE). Heating and cooling caused by a changing magnetic field are used analogous to the heating and cooling of a refrigerant gas in response to compression and expansion. This is a good intuitive description of the technique and figure 1.1 shows the four analogous steps for the two techniques. It is seen how an applied magnetic field aligns the magnetic spins (represented by arrows) in the refrigerant material. The fact that the increase of order in the material leads to a temperature increase might seem counterintuitive for those familiar with the concept of entropy, since more order in general means lower temperature. How-

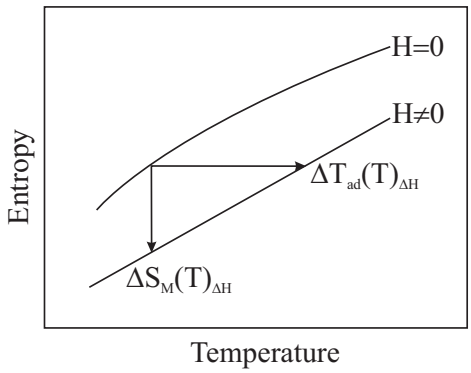

Figure 1.2: Thermodynamic TS diagram demonstrating the magnetocaloric effect by the adiabatic temperature change, $\Delta T_{ad}(T, \Delta H)$, and the isothermal magnetic entropy change, $\Delta S_M(\Delta H, T)$.

ever, this is exactly what demonstrates the principle of magnetic refrigeration, since the entropy of the magnetic material generally consists of three different contributions, a lattice, electronic and magnetic entropy (S_L, S_E, and S_M), respectively. The lattice and electronic contributions are essentially independent of magnetic fields, whereas the magnetic entropy is lowered due to ordering of the magnetic spins. That was the intuitive part, more order means lower entropy. However, the lowering of magnetic entropy results in an increase of the lattice entropy if the material is kept isolated from its surroundings (adiabatic conditions). The increase in lattice entropy means an increase in the temperature. This way of changing the temperature of a material by a magnetic field is the principle behind magnetic refrigeration.
To be able to use the principle for cooling something other than the material itself, magnetizing and demagnetizing the material is applied in a cyclic process as pictured in Figure 1.1, which allows to move heat from one end of a refrigerator system to the other. The temperature change in the refrigerant material upon application of a magnetic field is characteristic of the MCE and known as the adiabatic temperature change, $\Delta T_{ad}(T, \Delta H)$. The magnetocaloric effect can instead be characterized at constant temperature, where the application of a magnetic field results in a change of the magnetic entropy. This is known as the isothermal magnetic entropy change $\Delta S_M(\Delta H, T)$. In Figure 1.2 the two quantities are shown in a temperature-entropy (TS) diagram between two magnetic isofield curves without magnetic field (H=0) and a nonzero magnetic field (H≠0).

Magnetocaloric materials have the most extensive MCEs around magnetic phase transitions. In Figure 1.3 the behavior of a magnetocaloric material is shown as function of temperature. The maximum MCE is obtained in the

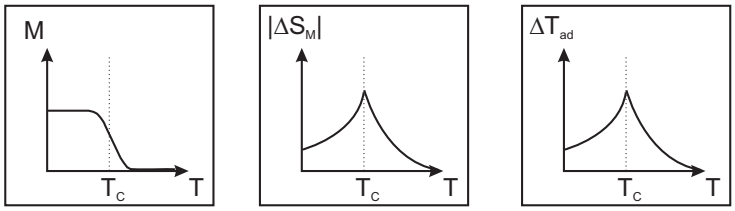

Figure 1.3: The maximum magnetocaloric effect is obtained in the vicinity of magnetic phase transitions such as the ferro- to paramagnetic phase transition. The magnetization, M, the adiabatic temperature change, ΔT_{ad}, and the isothermal magnetic entropy change, ΔS_M, are here shown as functions of temperature around the phase transition temperature T_C.

vicinity of magnetic phase transitions such as the ferro- to paramagnetic phase transition, which implies that magnetocaloric materials must have a magnetic phase transition temperature close to the working range of the refrigerator in order to be a potential candidate for magnetic refrigeration. In order to develop new refrigerants the MCE has to be evaluated in a consistent manner in order to be able to compare the materials. The main scope of this Ph.D. project has been the development of a new characterization technique to quantify the MCE and the use of this technique and others to design and characterize new magnetic refrigerants. Magnetic refrigeration cannot compete with vapor-compression technology by good refrigerants alone. In our group at Risø DTU not only the refrigerant materials are researched, but new refrigerant systems, small permanent magnet arrays with high fields and a large effort in numerical modeling of both systems and magnet configurations is part of the effort to make magnetic refrigeration viable. Since Brown [6] built his refrigerator, more than 20 prototypes have been developed all over the world [9] two systems alone in our group at Risø DTU. Furthermore, hundreds of materials have been evaluated and a rapidly increasing number of scientist and private companies are now taking part in the research.

1.2 Magnetocaloric Materials

There are several promising classes of materials with large MCEs and tunable Curie temperatures. All of them show great potential for room-temperature applications [10]. The properties that define a good performance of a magnetocaloric material may vary with the refrigeration system and desired temperature interval. The two parameters that provide a good basis for comparison are the adiabatic temperature change and the isothermal magnetic entropy change as was explained above. A general classification of magnetocaloric materials

divide them into two types according to the nature of the magnetic phase transition used to exploit the MCE. Since the MCE is highest around magnetic phase transitions the behavior of the materials around these transitions are crucial to the performance of the refrigerant. They can be divided into first order magnetic transition (FOMT) materials and second order magnetic transition (SOMT) materials. This division into two classes is convenient since certain characteristics in general follow each class. FOMT materials are currently thought to be the most promising candidates, since they show the highest measured values of the MCE. FOMT reach these high values of the MCE, since they have a very abrupt change in magnetization as function of temperature. The derivative of the magnetization is proportional to the magnetic entropy change and the very abrupt phase transitions therefore typically gives a high MCE in a narrow temperature range. On the other hand, SOMT materials in general have broader transitions with lower values of the MCE. Since in technological applications several other material properties are of importance, the choice between FOMT and SOMT materials are therefore not as straightforward as it might seem. FOMT's have in general slower kinetics than SOMT's, since they are normally connected with structural changes. This leads to different hysteresis phenomena which are unwanted in technological applications. Furthermore most of the known FOMT material systems contain either very expensive elements (e.g. Gd), toxic elements (e.g. As) or have very complicated and costly synthesis routes (e.g. La-Fe-Si-H). A variety of SOMT materials with expensive constituents or difficult synthesis routes has also been suggested. Due to several advantages in applications there is a continued interest in the class of mixed-valence manganites crystallizing in the perovskite structure despite the inferior MCE compared to many of the FOMT materials. Manganites are cheap, non-toxic, resistant to corrosion, easy to manufacture, have a decent MCE and have easily tunable transition temperatures. In the above classification they lie in between FOMT and SOMT materials depending on the compositions. Compositions from the class of mixed-valence manganites will be further investigated in this thesis. Several extensive reviews on magnetocaloric materials exists [10, 11, 12]. Figure 1.4 adopted from [10] shows a comparison of some of the most investigated magnetocaloric materials in a plot of $\Delta S_M(T)_{\Delta H=0.5T}$ versus transition temperature. It is quite evident from the figure that the FOMT materials have the highest MCE's, however most prototype magnetic refrigerators use pure gadolinium (Gd) as refrigerant, which is a SOMT material.

1.3 Outline of the Thesis

The focus of the thesis has been an experimental investigation of magnetocaloric materials. The thesis is structured in 8 chapters. The first four chapters is aimed

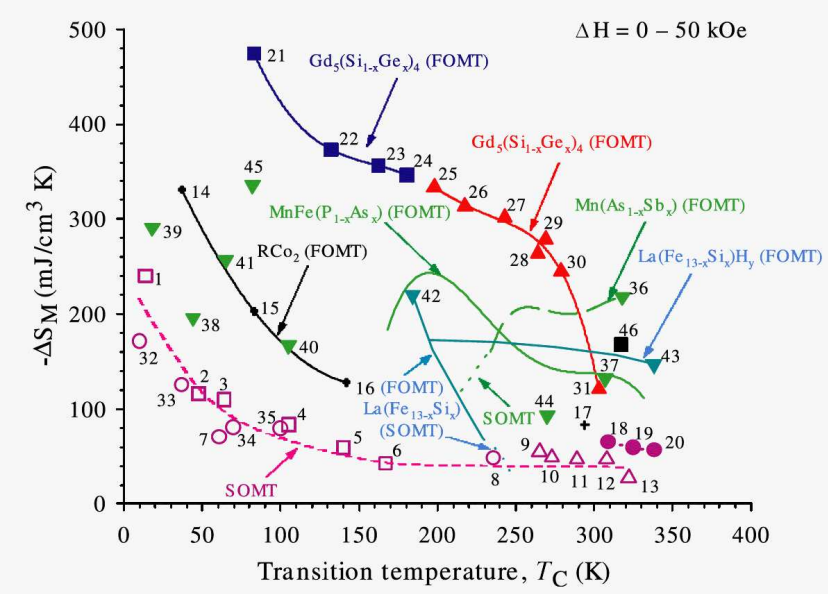

Figure 1.4: The different families of magnetocaloric materials plotted with their magnetic entropy changes, $\Delta S_M(T)_{\Delta H=0.5T}$ as function of transition temperature T_C. Pure Gd is seen with caption number 17 marked with a cross symbol. Adopted from [10]

to put the work in context by a short introduction to the field (Chapter 1), followed by the basic thermodynamical aspects of magnetic refrigeration (Chapter 2). The thermodynamics is described from the general equations of adiabatic cooling further to the linkage between entropy and magnetism, which makes the basis of adiabatic demagnetization. Then more specifically its described how parts of the entropy can be changed by a magnetic field, and finally how the heat capacity of a sample can be used to describe this entropy change. Chapter 3 is an introduction to the material systems investigated in this work. The materials belong to a class of magnetic oxides called mixed-valence manganites. Chapter 4 is describing the various experimental methods, which have been used in the synthesis and characterization of the materials. In order to characterize the heat capacity of the materials as function of magnetic field a specialized differential scanning calorimeter was constructed. The construction of this instrument has been one of the primary scopes of this work and is therefore elaborated in a single chapter (Chapter 5). Two material systems are treated in this thesis. In Chapter 6 investigations the MCEs upon copper doping in the mixed-valence manganite system La-Ca-Mn-O are described. In Chapter 7 studies on substitution of pure lanthanum with an impure lanthanide mixture

have been investigated also in the mixed-valence manganite system La-Ca-Mn-O. Finally the thesis is closed in Chapter 8 with a concluding summary of the findings and several suggestions for future work. Appendix A concerns a procedure used for the subtraction of baselines from entropy changes calculated from calorimetric measurements. Appendix B to D is reprints of published papers, Appendix E is the patent application, which is confidential until publication and Appendix F represents a paper in preparation.

CHAPTER 2

Thermodynamic Theory of the Magnetocaloric Effect

A general introduction to the thermodynamics of the MCE is given in this chapter. First some aspects of adiabatic cooling are described, then its described how the MCE can be utilized in adiabatic cooling by adiabatic demagnetization. Finally the role of the heat capacity in magnetocaloric materials are described. The heat capacity can be used as an essential parameter in the description and quantification of the MCE. Elaborated reviews on the thermodynamics of the MCE can be found in [13, 14]

2.1 Thermodynamics of Adiabatic Cooling

Adiabatic cooling such as adiabatic demagnetization, which is the principle behind magnetic refrigeration, are based on the fact that the total entropy, S, of a system is a thermodynamic state function that can be altered by external thermodynamic variables like temperature (T), pressure (p), and magnetic field (H)

$$S = S(T, p, H) \tag{2.1}$$

The change in entropy, dS, can be written as

$$dS(T, p, H) = \left(\frac{\partial S}{\partial T}\right)_{p,H} dT + \left(\frac{\partial S}{\partial p}\right)_{T,H} dp + \left(\frac{\partial S}{\partial H}\right)_{T,p} dH \tag{2.2}$$

In general, in magnetic refrigerators variations in pressure are too small to play a significant role in the entropy change and therefore can be neglected. However, there are some studies showing how to use applied pressure instead of magnetic

field in adiabatic cooling [15]. In this thesis however materials and processes will be assumed to be at constant pressure (isobaric). For isobaric processes dS becomes

$$dS(T,H) = \left(\frac{\partial S}{\partial T}\right)_H dT + \left(\frac{\partial S}{\partial H}\right)_T dH \tag{2.3}$$

By keeping the temperature constant and applying a magnetic field, we can induce an isothermal entropy change ΔS. The ability of a material to produce this entropy change can be used in a cooling process as will be explained below. The isothermal entropy change induced by an applied magnetic field change from H_0 to H_1 is defined as

$$\Delta S_{H_0 \to H_1} = S(T,H_1) - S(T,H_0) \tag{2.4}$$

$$= \int_{H_0}^{H_1} \left(\frac{\partial S(T,H)}{\partial H}\right)_T dH \tag{2.5}$$

where subscript T indicates isothermal conditions. In adiabatic cooling, the entropy is instead kept constant (dS=0), and by applying a magnetic field a temperature change is induced in the material. This temperature change was described in the introduction and is known as the adiabatic temperature change, ΔT_{ad}. Since the total entropy must be conserved (adiabatic conditions) the following must apply

$$S(T,H_1) = S(T + \Delta T_{ad}, H_0) \tag{2.6}$$

and from the definition of heat capacity, $C_{conditions}$, we can rearrange to express the entropy

$$C_{conditions} = T\frac{dS}{dT} \Rightarrow S = \int \frac{C_{conditions}}{T} dT + S_0 \tag{2.7}$$

which under the assumption of constant pressure is expressed as

$$S(T)_H = \int \frac{C_p(T)_H}{T} dT + S_0 \tag{2.8}$$

Differentiating with respect to temperature yields

$$\left(\frac{dS(T,H)}{dT}\right)_H = \left(\frac{C(T,H)}{T}\right)_H \tag{2.9}$$

and since dT can be defined from Equation 2.3 now imposing adiabatic conditions (dS=0), dT becomes

$$dT = \left(\frac{\partial T}{\partial S}\right)_{p,H} \left(\frac{\partial S}{\partial H}\right)_{T,p} dH \tag{2.10}$$

By subsequently combining Equations 2.9 and 2.10 and integrate from H_1 to H_0 the adiabatic temperature change, ΔT_{ad}, can be expressed

$$\Delta T_{ad}(T,H)_{H_1 \to H_0} = \int_{H_1}^{H_0} \left(\frac{T}{C(T,H)} \frac{\partial S(T,H)}{\partial H} \right)_T dH \tag{2.11}$$

In this equation, the magnetic field have been chosen to change from H_1 to H_0 to indicate that it is the demagnetization that yields the adiabatic cooling in a magnetocaloric material.

2.2 Magnetocaloric Effect and Adiabatic Demagnetization

To express the entropy change in terms of the magnetization, M, we need to introduce the relationship between entropy and magnetization. From the thermodynamic Maxwell equations [16]

$$\left(\frac{\partial S(T,H)}{\partial H} \right)_T = \left(\frac{\partial M(T,H)}{\partial T} \right)_H \tag{2.12}$$

Integrating equation 2.12 from zero field, H_0, to an applied magnetic field, H_1 yields

$$\Delta S = \int_{H_0}^{H_1} \left(\frac{\partial M(T,H)}{\partial T} \right)_H dH \tag{2.13}$$

the equation shows that magnetic entropy change is proportional to both the derivative of magnetization with respect to temperature at constant field and to the magnitude of the field variation. To express also the adiabatic temperature change, ΔT_{ad}, in terms of the magnetization we combine equation 2.11 and 2.12

$$\Delta T_{ad}(T,H)_{H_1 \to H_0} = \int_{H_1}^{H_0} \left(\frac{T}{C(T,H)} \frac{\partial M(T,H)}{\partial T} \right)_H dH \tag{2.14}$$

From Equations 2.13 and 2.14 information about the behavior of MCE in solids can be extracted. Since it is well known that magnetization at constant magnetic field decreases in both para- and ferromagnetic materials with increasing temperature, i.e., $(\partial M/\partial T)_H < 0$, we can see from the equations that ΔT_{ad} is positive and ΔS_M is negative for positive field changes, $\Delta H > 0$. Furthermore, in ferromagnets where the absolute value of the derivative of magnetization with respect to temperature, $(\partial M/\partial T)_H$, is maximum at the Curie temperature, T_C, the values of ΔT_{ad} and ΔS_M should also peak at the temperature $T = T_C$. From equation 2.14 it is also seen that the adiabatic temperature change increases with increasing temperature and decreasing heat capacity. Since ΔT_{ad} is what determines the potential of the refrigerator material it becomes evident, that the

heat capacity plays a significant role, not only heat capacity at constant field, but also how heat capacity varies with magnetic field. As would be expected both ΔT_{ad} and ΔS_M increases with increasing field variation $H_0 \rightarrow H_1$.

2.3 Entropy and its Dependence on the Magnetic Field

The total entropy is the sum of the lattice S_L, electronic S_E and magnetic S_M entropy [13]

$$S = S_L(T,H) + S_E(T,H) + S_M(T,H) \tag{2.15}$$

This is a general presentation and only valid in a magnetic solid with localized moments. In solids with electrons of itinerant nature the three contributions cannot be clearly separated. As a first approximation we can believe that the electronic and lattice part are not affected by a magnetic field and therefore the term S_M will present any contribution to the total entropy made by the applied magnetic field. The lattice entropy can be represented according to [13] by the Debye interpolation formula:

$$S_L(T,H) = n_a R \left[-3\ln(1-e^{T_D/T}) + 12\left(\frac{T}{T_D}\right)^3 \int_0^{T_D/T} \frac{x^3 dx}{e^x - 1} \right] \tag{2.16}$$

where R is the gas constant, T_D the Debye temperature, n_a the number of atoms per formulae unit. The electronic part of the entropy can be represented by the standard relation:

$$S_E(T,H) = a_e T \tag{2.17}$$

where a_e is the electronic heat capacity coefficient. As follows from Equations 2.16 and 2.17 the lattice and electronic entropy contributions are only functions of temperature and not magnetic field in this approximation. The total entropy can therefore in general be written as

$$S = S_L(T) + S_E(T) + S_M(T,H) \tag{2.18}$$

deriving the relation between entropy and heat capacity from the definition of heat capacity

$$C_p = \left(\frac{\partial Q}{dT}\right)_p \tag{2.19}$$

where ∂Q is the dissipated heat during a temperature change dT at constant pressure, p, and combining this definition with the second law of thermodynamics here written on differential form

$$dS = \frac{\partial Q}{T} \tag{2.20}$$

we have the relation between heat capacity and entropy [13]

$$C_p = T\left(\frac{dS}{dT}\right)_p \tag{2.21}$$

Remembering that S_L and S_E in equation 2.18 are independent of magnetic field, we can write the differential of the total entropy as

$$dS(H,T) = \frac{C_L}{T}dT + \frac{C_E}{T}dT + \frac{C_M}{T}dT + \left(\frac{\partial S_M(H,T)}{\partial H}\right)_T dH \tag{2.22}$$

where the last two terms express the total differential of the magnetic entropy

$$dS_M(H,T) = \frac{C_M}{T}dT + \left(\frac{\partial S_M(H,T)}{\partial H}\right)_T dH \tag{2.23}$$

from this equation we can see that the magnetic entropy change describing the MCE can be evaluated in two ways. It can be deduced from isothermal magnetization data remembering that the last term can be expressed as function of magnetization also shown in equation 2.13. Alternatively, the magnetic entropy change can be deduced from isofield heat capacity data using instead the first term in equation 2.23.

2.4 Heat Capacity

It has been reported [17] that deducing the magnitude of the MCE from heat capacity combined with isothermal magnetization data can reduce the error significantly. Heat capacity measurements in applied magnetic fields is however not a straightforward technique. The thermodynamic properties of materials is often obtained from Differential Scanning Calorimetry (DSC) measurements. Commercial DSC's however do not have the option to measure in magnetic fields. Nevertheless an increasing number of DSC inserts in superconducting magnets have been reported [18, 19, 20, 21] and is now also commercially available e.g. Quantum Design PPMS® system[1]. In this work, a DSC under applied magnetic field has been developed. Characteristic of this DSC opposed to the above mentioned is mainly that it is a cheap versatile system, designed to work with any laboratory magnet. It uses a principle well known to produce highly accurate and reproducible results [18, 19, 20], and without the need of liquid helium normally used in superconducting magnet setups. By knowing the heat capacity as function of an applied magnetic field, the magnetic entropy can be calculated. A numerical integration of Equation 2.8 was proposed by Pecharsky

[1] http://www.qdusa.com/products/ppms.html

et al. [17] using the following formula:

$$S(T_n)_H = 0.5\left\{C(T_1)_H + \sum_{i=1}^{n-1}\left[\left(\frac{C(T_i)}{Ti} + \frac{C(T_{i+1})}{T_{i+1}}\right)_H \times (T_{i+1} - T_i)\right]\right\} \tag{2.24}$$

where, H represents the applied magnetic field, and n is the number of heat capacity data points obtained between the temperatures, T_1 and T_n . The term $C(T_1)_H$ accounts for the missing heat-capacity data between the lowest temperature of the experiment T_1 and T=0 K assuming that $C(T=0)_H=0$. Subsequently, the entropy change corresponding to a field change $H_0 \rightarrow H_1$ can readily calculated from

$$|\Delta S(T)|_{H_0 \rightarrow H_1} = S(T)_{H_1} - S(T)_{H_0} \tag{2.25}$$

where the entropies have been calculated using Equation 2.24.

CHAPTER 3

Manganites

The magnetocaloric materials that have been synthesized and characterized in this work all belong to the family of mixed-valence manganites. This chapter describes the general aspects of this class of materials.

3.1 Historical Perspective

The doped perovskite manganites have been investigated since the fifties, e.g. the work of Jonker and Van Santen [22] carried out on the compounds La_{1-x}-A'$_x$MnO3 with A' = Ca, Sr and Ba. Jonker and Van Santen found that the end members (x=0 and x=1) of these materials were antiferromagnetic and insulators. However, for intermediate values of x, the materials ordered ferromagnetically. It was found that the ferromagnetic interaction was strongest around x=2/3 and that the onset of ferromagnetism is associated with a sharp increase in electrical conductivity [22]. Later Zener proposed the well known double exchange model [23] to explain the link between ferromagnetism and metallic behavior - a ferromagnetic exchange coupling between magnetic ions present in different valence states. The magnetoresistance (MR) effect was discovered in 1954 by Volger [24]. The discovery of giant magnetoresistance (GMR) and colossal magnetoresistance (CMR) in the 1990s [25] resulted in an enormous attention in the doped perovskites.
Of scientists contributing to the early works on the doped perovskites must be mentioned Wollan and Koehler, who in 1955 reported on ferro- and antiferromagnetic regions in $La_{1-x}Ca_xMnO_3$ [26]. After the re-discovery in the 1990s of

the mixed-valence manganites in the field of magnetoresistance, these materials have primarily been known as CMR materials. Some of the most famous results were published in 1994 by Jin et al. [25] with an impressive magnetoresistance value of 127.000% reached in thin film samples of La-Ca-Mn-O at 77 K and an applied magnetic field of 6 Tesla. However, magnetoresistance didn't appear to be the only field of application for this type of materials. The doped perovskites have also been widely used in the field of Solid Oxide Fuel Cells (SOFC) [27] as electrode material. Furthermore, Morelli et al. [28] presented later their results in 1996 on MCEs in $La_{0.67}Ca_{0.33}MnO_3$ with A=Ca, Ba and Sr. They showed that magnetic entropy changes in this system was in the same order of magnitude as that of gadolinium (Gd), which still today is considered as benchmark material in magnetic refrigeration at room temperature.

3.2 Structure and Properties

Manganites are perovskite structured oxides. The perovskite structure has its name from the cubic structured mineral perovskite $CaTiO_3$ and is also referred to as the ABO_3 structure. The structure is a closed-packed array of O^{2-} anions and A cations. The B cations are located in octahedral symmetry in the BO_6 octahedra (Figure 3.1). In this work we only deal with manganites, where the B-site is occupied by Mn-ions, i.e. $AMnO_3$.

3.2.1 Ionic Size Distribution

The stability of the perovskite structure is often defined by the tolerance factor t^*. This factor was defined by Goldschmith in 1926 [29] and is therefore commonly referred to as the Goldschmith factor

$$t^* = \frac{r_A + r_O}{\sqrt{2}(r_B + r_O)} \tag{3.1}$$

where r_A and r_B are the mean radii of the ions occupying the A-sites and the B-sites, respectively, and r_O is the ionic radius of oxygen. Stable perovskites are formed if t^* is within the range $0.89 < t^* < 1.02$ [30].

Should the A-site cation exactly match the close packed structure t^* would be equal to 1 and the perovskite would be cubic. As an example we have calculated tolerance factor of $La_{0.67}Ca_{0.33}MnO_3$, which is used in the present investigation. The mean radius on the A-site, $\langle r_A \rangle$, will be calculated as $0.67{*}r_{La^{3+}}{+}0.33{*}r_{Ca^{2+}}$ assuming that the A-sites have 9-fold coordination and using the values listed in Table 3.1. The mean radius of the B-site, $\langle r_B \rangle$, has been calculated by assuming that 67% of the B-sites are occupied by Mn^{3+} and 33% by Mn^{4+} ions as a

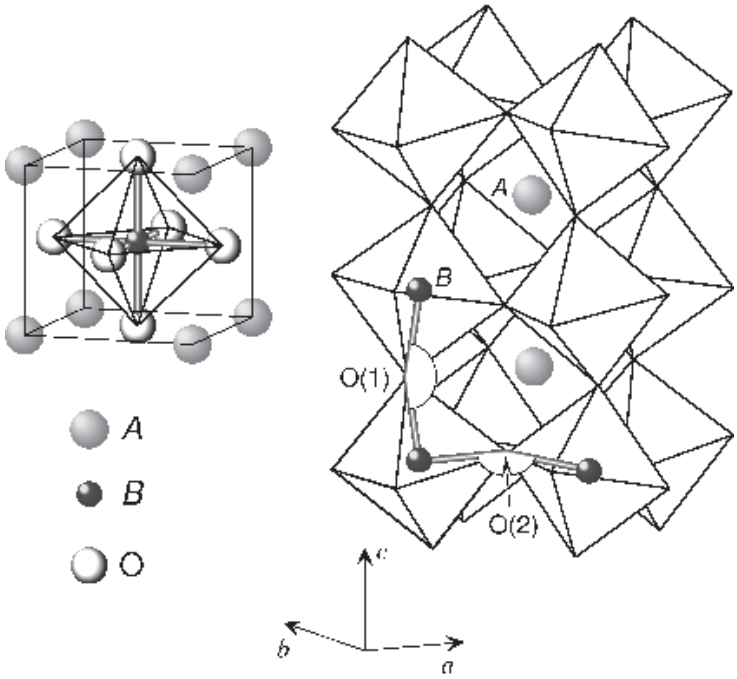

Figure 3.1: ABO_3 perovskite structure. Left: The cubic perovskite structure with the A cation in the corners and the B cations in the center of the BO_6 octahedra. Right: The perovskite structure packs with the BO_6 octahedra connected at the vertices and the A cations situated at the interstitial sites between the octahedra. Here the octahedra are tilted with respect to each other with a B-O-B bond angle $\neq 180^\circ$ in what is called a $GdFeO_3$-type orthorhombically distorted perovskite.

consequence of 33% divalent Ca ions being substituted for trivalent La ions.

$$t^* = \frac{0.67 * 0.1216nm + 0.33 * 0.1118nm + 0.140nm}{\sqrt{2}(0.67 * 0.0645nm + 0.33 * 0.053nm + 0.140)} = 0.91 \qquad (3.2)$$

which fulfills the stability criterion of forming a stable perovskite structure. Since $t^* \neq 1$, the perovskite structure is distorted from the cubic structure. In addition to distortions caused by the size mismatch between A- and B-site in the perovskite, a well known effect in transition metal compounds (in our case manganese) is the Jahn-Teller (JT) distortion. The JT distortion occurs in d^9, d^7 low spin and in d^4 (Mn^{3+}) high spin states for octahedrally coordinated transition metals, since they all have doubly degenerate ground levels [32]. The reason is that the e_g orbitals involved in this degeneracy point directly

A-site	B-site	O-site
La^{3+} 0.1216 nm	Mn^{4+} 0.0530 nm	O^{2-} 0.140 nm
Ca^{2+} 0.1118 nm	Mn^{3+} 0.0645 nm	
(9-fold coordination)	(6-fold coordination)	(8-fold coordination)

Table 3.1: Ionic radii in the $LaCaMnO_3$ perovskite taken from Shannon [31].

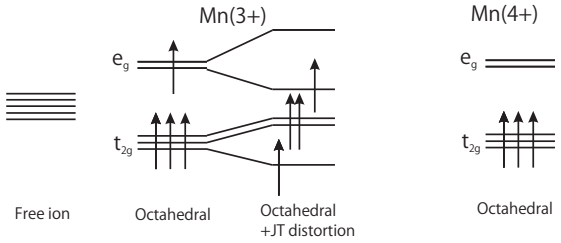

Figure 3.2: The Jahn-Teller distortion in octahedral symmetry affecting Mn^{3+} but not Mn^{4+}.

towards the ligands and therefore offering a significant lowering of the energy by distorting the structure, as will be discussed below.

3.2.2 Jahn-Teller Effect and Crystal Field Splitting

To understand the JT effect we need to understand how the energy levels of an atom depends on its surroundings. In octahedral symmetry the five d-orbitals of transition metals d_{xy},d_{xz},d_{yz},d_{z^2} and $d_{x^2-y^2}$ are split into two groups lifting the degeneracy: The low energy t_{2g} group consisting of d_{xy},d_{xz} and d_{yz}, and the high energy e_g group consisting of d_{z^2} and $d_{x^2-y^2}$ (see figure 3.2). The reason for the splitting in energy is the difference in Coulomb repulsion between orbitals (Figure 3.3). For the d^4 to d^7 ions two configurations occur, the low spin state (LS) and the high spin state (HS). Whether the ion is in LS or HS depends on the competition between two energy contributions. With respect to Hund's first rule the HS state is preferred since it maximizes **S**, but the cost, Δ, of putting an electron in the elevated e_g energy level in the octahedral symmetry has to be balanced with the cost of putting 2 electrons in the same low energy t_{2g} orbital. The HS is most likely to occur in $3d$ orbitals since $\Delta(3d) < \Delta(4d) < \Delta(5d)$[33].

The crystal field splitting of the orbital energies is a result of the crystal field potential, which "quenches" the orbital angular momentum i.e. it obstructs the free rotation of the orbital. This phenomenon is called orbital quenching and is important in $3d$ ions since the crystal field interaction is much larger than the spin-orbit coupling [34, 35].

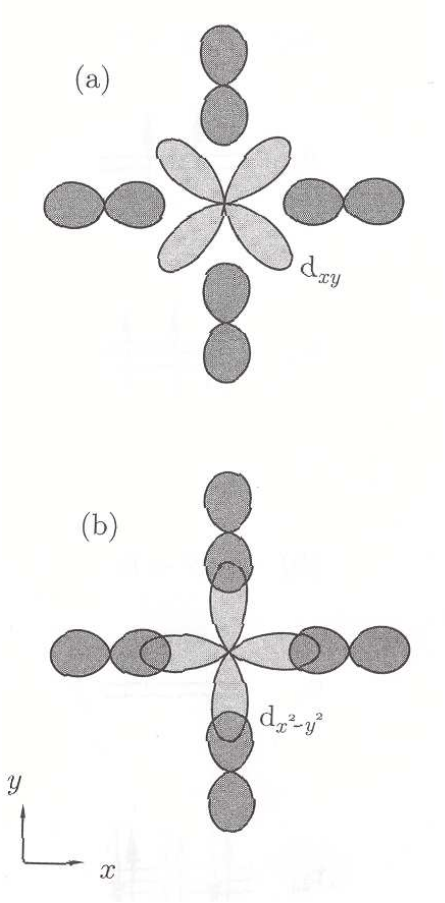

Figure 3.3: The difference Δ (see text) between t_{2g} and e_g orbitals originate from the Coulomb repulsion between overlapping p-orbitals from oxygen and the d-shell t_{2g}- and e_g-orbitals in octahedral symmetry. a)Repulsion is low in $t_{2g}(d_{zx}$ is shown) and b) high in $e_g(d_{x^2-y^2}$ is shown). Adopted from Blundell [34].

If the symmetry is high, the degeneracy will be high, since there are many possible symmetry transformations, whereas in low symmetry this degeneracy is lifted. The JT effect lowers the symmetry in order to minimize the energy.
In octahedral symmetry, O_h, the d-orbitals were split into e_g- and t_{2g}-orbitals lifting the degeneracy. By distorting O_h the degeneracy can be lifted even further. In some cases this distortion of the symmetry can be energetically favorable. This distortion of symmetry is known as Jahn-Teller (JT) distortion or the JT effect and has given name to the JT theorem stating that:

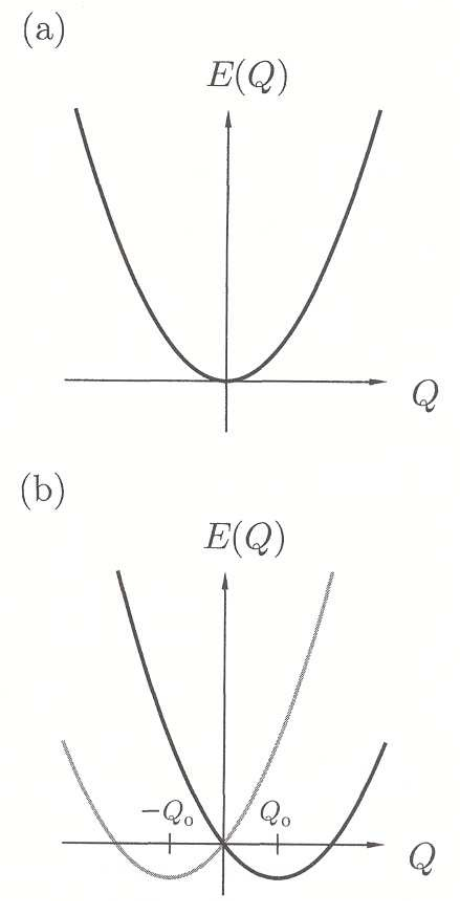

Figure 3.4: a) The energy E(Q) of an octahedral complex as function of the distortion parameter Q. b) E(Q) including the electronic energy dependence to the first order giving rise to a minimum energy finite valued distortion Q_0. Adopted from Blundell [34].

> If an ion is at a crystal site of such high symmetry that its ground-state degeneracy is not a Kramers minimum, then it will be energetically favorable for the crystal to distort in such a way to lower the symmetry enough to remove the degeneracy. [36]

The essential point is, that the energy increase due to the distortion of the lattice, is proportional to the 2nd power of the distortion, whereas the energy splitting of the orbital states is linearly proportional to the distortion. If we quantify the distortion by a parameter Q, the energy cost of the lattice distortion

can be written as

$$E(Q) = 1/2M\omega^2Q^2 \tag{3.3}$$

where M is the mass of the anion, ω is the angular frequency corresponding to the particular normal mode [34, 37]. It is obvious that distortion of the lattice will cost energy, and therefore the lattice term has a minimum in zero distortion (Figure 3.4.a). The linear term due to splitting of the orbital states can be either positive or negative with respect to raising or lowering of the electronic energy, respectively. The electronic energy is normally quite complicated but can be approximated by a Taylor expansion and assuming that the distortion is small, we can neglect any higher order terms and settle with the linear term. Doing this we obtain the following expression for the electronic contribution

$$E(Q) = \pm AQ \tag{3.4}$$

where A is a constant. The sum of the electronic contribution (i.e. Equation 3.4) and the elastic contribution (Equation 3.3) gives us the total energy of the octahedral complex

$$E(Q) = \pm AQ + 1/2M\omega^2Q^2 \tag{3.5}$$

which is shown in figure 3.4.b. From (3.5) the minimum E(Q) is obtained at $\pm Q_0$ with a value of $E(Q)_{min}$

$$Q_0 = \frac{A}{M\omega^2} \tag{3.6}$$

$$E(Q_0)_{min} = \frac{-A^2}{2M\omega^2} \tag{3.7}$$

This implies that the octahedral complex described in this simple model will gain energy by distortion [34]. In this treatment of the (JT) effect it is not considered whether or not the distortion could become unstable due to vibrations of the anions. If such vibrations have amplitudes exceeding the distortion Q_0 this simple model will not be valid, but has to be replaced with dynamical calculations [34]. If the approximation is valid the distortion is stable and known as a static JT distortion and it would result in a spontaneous distortion in order to lower the energy of the complex. In context with the ferromagnetic double-exchange mechanism that will be treated in the following section, the perovskite structure is seen to provide the possibility of electrons moving freely between two ions of mixed valency. Ferromagnetic coupling between these electrons is the basis of the double exchange mechanism. However, in terms of JT effect the fact that an electron hops into an empty orbital, while hopping from site to site, the electron "drags" the lattice distortions and the JT effect will have a dynamic character instead of a static. The electron with its accompanying lattice distortion forms a so-called lattice polaron [38]. Since the surrounding

oxygen atoms are much larger than the electron, the polaron behaves as a negatively charged particle with a larger mass and lower mobility than an isolated electron.

3.3 Magnetic Interactions

3.3.1 Double Exchange

After Jonker and van Santen [39] discovered the strong correlation between ferromagnetism and conductivity in perovskites, Zener proposed a theory that could explain this phenomenon in a mixed-valence state, namely the double exchange mechanism (DE). Zener explained that two degenerate ionic configurations could occur [23]

$$\psi_1 : \mathrm{Mn}^{3+}\mathrm{O}^{2-}\mathrm{Mn}^{4+} \qquad \psi_2 : \mathrm{Mn}^{4+}\mathrm{O}^{2-}\mathrm{Mn}^{3+} \tag{3.8}$$

In this model the two configurations are connected by the double-exchange matrix element, which arises from the transfer of an electron from Mn^{3+} to O^{2-} simultaneous with the transfer of an electron from O^{2-} to Mn^{4+}. The transfer is fundamentally different from the superexchange in that the two ions have different valency [34]. The matrix element only has finite value when the Mn ions are aligned ferromagnetically due to a strong Hund coupling. The system resonates between ψ_1 and ψ_2, and if the core spins are aligned thus having a ferromagnetic and conducting state [40]. Later Anderson and Hasegawa [41] revised Zener's work treating the Mn cores classically but the moving electron quantum mechanically. The fundamental result of their work and still basic to the double exchange theory is that the hopping probability becomes a function of the angle between the core spins. The double exchange Hamiltonian can be written in Block form

$$\mathbf{H} = \begin{bmatrix} -J_H\mathbf{S_1}\cdot\mathbf{s} & t_0\mathbf{I} \\ t_0\mathbf{I} & -J_H\mathbf{S_2}\cdot\mathbf{s} \end{bmatrix}$$

where the 2x2 diagonal blocks H_{11} and H_{22} correspond to energy states of the electron and the Mn^{4+} core ion at site 1 and 2, J_H is the Hund coupling and t_0 is the normal transfer integral and $\mathbf{I}$ is the unit matrix. If the Hund coupling is strong, $J_H >> t_0$, we have two low energy solutions, which are eigenvalues of the Hamiltonian

$$E = -\frac{J_H S}{2} \pm t_0 cos\left(\frac{\theta}{2}\right) \tag{3.9}$$

where θ is the angle between the Mn^{4+} spins. From this equation it is readily seen that since the lowest energy and hence the ground state is obtained for parallel spins between neighboring core spins the double exchange mechanism

leads to ferromagnetism. The effective transfer integral can be written as

$$t_{\text{eff}} = t_0 cos\left(\frac{\theta}{2}\right) \tag{3.10}$$

In 1955 Goodenough [42] calculated that the optimum composition of a mixed-valence manganite in terms of ferromagnetic coupling was around x=0.31 (La^{3+}_{1-x}-$A^{2+}_{x}MnO_3$). The substitution of a trivalent La^{3+} ion with a divalent alkaline earth changes two Mn ions from Mn^{3+} to Mn^{4+} and one trivalent La ion to become divalent in order to minimize the Madelung energy of the configuration [42]. Goodenough calculated that in order to obtain the maximum number of randomly distributed Mn^{4+} ions with one and only one Mn^{3+} neighbor the composition has to be x=0.31. Several studies have later reconfirmed e.g. [43, 44, 45], that optimum conditions in the mixed-valence manganites is in the vicinity of x=1/3. Many studies have been carried out earlier on compositions with x=0.33, and this was the basis for choosing this composition in the present work.

CHAPTER 4

Experimental Methods

The application of manganites as refrigerant materials in magnetic refrigerators requires preparation in bulk form. Bulk ceramic materials are prepared by colloidal ceramic processing or dry powder pressing. In colloidal processing manganite powders are suspended in a solvent. The materials are subsequently shaped by different consolidation techniques such as tape casting, extrusion, lamination etc. and then dried and sintered to obtain the final material. In the dry powder pressing method, which was utilized in this work, the powders are pressed into a shape and then subsequently sintered.
The manganite powders can be prepared either by soft chemistry methods, such as co-precipitation or combustion synthesis. The powders can also be synthesized by solid state reaction methods. For other purposes manganite thin films can be produced by techniques such as laser ablation [46] or sputtering [47]. It is well known that mixed-valence manganites are very sensitive to the synthesis [38, 48, 49, 10, 13, 50, 11].
Adequate heat treatment of both powders and bulk shapes are necessary, since the phase purity, stoichiometry and oxygen content is sensitive to the route of synthesis [51]. The crystallinity of the sample plays a significant role and the synthesis of single as opposed to poly-crystalline materials can greatly enhance the magnetocaloric properties [52]. The polycrystalline manganites are also sensitive to grain sizes. The grain size alters the conductive as well as the magnetic properties of manganites [53].
From a technical point of view the porosity of the manganites becomes important as well. Porosity represents dead volume in the material with no contribution to refrigeration. The volume of the refrigerant is a very important design aspect

in magnetic refrigerator systems, since the cost of producing a strong magnetic field is very high. From this consideration materials must be as dense as possible to ensure cost-effectiveness of the refrigerator system. On a larger scale the bulk shape of the refrigerator material determines the geometry dependent demagnetizing field in the sample. The demagnetizing field is acting opposite to the applied magnetic field reducing the magnetic flux density available to produce the entropy change. The surface topology of the final bulk shaped refrigerant is also important since it partly determines the heat transfer between the refrigerant and the cooling liquid [54].

4.1 Sample Synthesis and Heat Treatment

As explained the structure and properties of mixed-valence manganites are very sensitive to the synthesis. It has not been the scope of this work to investigate these processes in detail, but to ensure the best possible consistency between samples as few parameters as possible have been altered. By using the same synthesis to prepare all samples, information on the actual effect of the altering compositions have been investigated.

4.1.1 Glycine-Nitrate Combustion Synthesis

In this work all powders were synthesized using the glycine-nitrate combustion synthesis described by Chick and Bates [55]. This combustion synthesis is known to produce highly homogenous powders with a uniform distribution of cations [55]. The Glycine-nitrate combustion synthesis (GNS) starts from stock solutions of nitrates. The solutions are prepared from laboratory grade (99.9%) metal nitrates diluted in water rinsed in a milli Q column[1] to avoid additional adding of impurities from the water. The solution concentrations are determined by calculating the weight loss upon drying and typically lies in the vicinity of a 0.1 nitrate/water ratio. There is a tradeoff between accuracy and synthesis time, since the error induced by weighing is minimized in very dilute solutions. However, in very dilute solutions it takes longer to remove the water from the solution and longer synthesis time increases the possibility of precipitation. In all samples produced in this work no precipitation was observed. The nitrate solutions are then added in the intended ratio in a large beaker to obtain the stoichiometric composition that were intended and then glycine (NH_2CH_2COOH) is dissolved in the nitrate solution. The glycine actually has two purposes in the synthesis, it acts as fuel for the combustion by oxidation of glycine by the nitrate ions, but the glycine also helps to form complexes with the metal ions in the solution and thereby increase the solubility. Glycine is

[1] http://www.millipore.com/catalogue/module/c7658

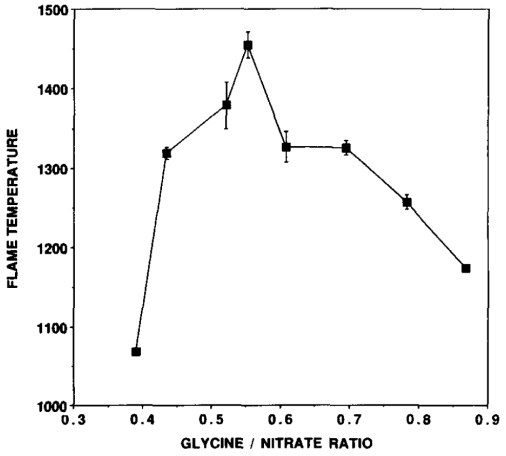

Figure 4.1: The combustion temperature as function of glycine/nitrate ratio. The relation shows the combustion of glycine-nitrate chromite precursors. Adopted from Chick and Bates [55].

added in molar ratio of glycine/nitrate in the vicinity of 0.55 to produce a very high temperature [55]. In this work the ratio was increased to 0.57 to minimize the explosion during combustion. The explosion was so powerful, when using the 0.55 ratio, that the lid of the chimney that collects the powder was blown away and very little powder remained to be collected. The relation between nitrate/glycine ratio and combustion temperature is pictured in Figure 4.1 from the original article [55] showing the relation during synthesis of chromites. As it is evident in Figure 4.1 the ratio should be increased or decreased depending on the exact relation in a given composition. In this work the actual reaction temperature has not been measured, but since the increased ratio minimized the explosion its reasonable to assume that our ratio is situated somewhere on the right side of the characteristic peak for the manganite system. The ratio is kept constant for all samples in this work.

Having a solution with the intended ratio between the constituent nitrate solutions to produce a manganite with the intended stoichiometry, the excess water then need to be removed. To do this the solution is heated in the beaker on a hot plate heater. The gel slowly transforms into a foam as the water is removed. This process takes a couple of hours and finally the foam becomes very viscous and no visible water vapor condenses on the beaker sides anymore. The final step is then to increase the temperature of the hot plate and to place the beaker under a chimney. The thermal evaporation of the water continues until the foam self-ignites. The function of the chimney is to enclose a large volume that can collect the powder during the combustion explosion, and is therefore

sealed of with a fine metal net in the top to allow release of the pressure and collection of the powder. The high combustion temperature and short combustion time results in a very pure powder with low-levels of residual carbon [55]. However, all parts of the powder might not be completely in an equilibrium phase due to the fast heating and cooling. This might also result in a small uniformity of the ion distribution in the powder. To ensure that the powder is well-crystallized in a single phase and the cations uniformly distributed in the stoichiometric composition the as-synthesized powder is heat treated after the combustion synthesis. This heat treatment is called calcination and takes place at an elevated temperature to allow for thermal decomposition in the powder, but below the melting point of the composition. To avoid agglomeration of the powder and ensure good mixing the powders are ball-milled in air for at least 24 hours. The ball-milled powders are then placed in alumina crucibles and placed in air in a high-temperature oven. All powders in this work were ramped at 50 K/hour to $700°C$, where they were kept for 5 hours before ramping back to room temperature at 50K/hour again. The calcination causes a slight aggregation of the powder, which therefore needs to be crushed subsequently in a mortar.

4.1.2 Dry Pressing

The powder is the corner stone of the synthesis, but further synthesis is necessary to be able to use the manganite as refrigerant material as was explained above. In this work the final samples have been made by dry powder pressing. The calcinated powders are pressed into cylinders of 5 mm in diameter and 6-7 mm in height with an uniaxial load of 1 ton. This load corresponds to a pressure around 10 MPa. The pressure cannot be determined very accurately, but all cylinders have been made using the same load on the uniaxial press. The cylinder is subsequently sintered to transform the powder compact into a dense material. During sintering the porosity of the material is eliminated by diffusion. In this work all the pressed cylinders have been sintered in air for five hours at $1200°C$ to obtain single phase polycrystalline samples of the different target compositions.

4.2 Structural Characterization

The structural characterization was carried out using X-ray diffraction (XRD). XRD is a powerful tool widely used to extract quantitative information about the crystallin structure of materials. Since it is a non-destructive characterization technique, which can probe length scales from Ångstrøms to several micro-meters, it is the primary structural characterization technique for solid state materials. After many years as a "waste product" at synchrotron facilities in storage rings that were designed to do high-energy particle physics, the pri-

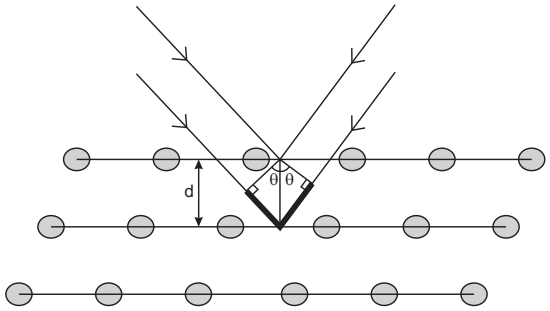

Figure 4.2: Bragg reflection from a set of lattice planes with interplanar spacing d. The incident and reflected x-rays are shown for two neighboring planes and their path difference is shown with a bold line.

mary purpose of many modern synchrotron facilities is the generation of x-rays [56]. Synchrotron radiation and especially modern 3rd generation sources have extremely high brilliance, which is attractive for structural characterization, but most laboratory facilities and universities also have an in-house standard diffractometer with a fixed or rotating anode setup. In this work a STOE-CIE diffractometer with Bragg-Brentano symmetry ($\theta - 2\theta$) has been used for the structural characterization. It is a fixed tube Cu-anode diffractometer using both Cu K_{α_1} and Cu K_{α_2} radiation (λ=0.154056 nm, and λ=0.154439 nm, respectively). In such a scan, the sample and detector angles are changed in a constant ratio of 1:2 and constructive interference is obtained from beams diffracted from adjacent atomic planes when the Bragg condition is met. The Bragg condition dictates constructive interference when the path difference is an integral number of wavelengths

$$n\lambda = 2d \sin\theta \tag{4.1}$$

with λ being the wavelength, d the interplanar spacing and θ the angle of incidence. The Bragg condition is shown in Figure 4.2, where the path difference is shown with a bold line. All diffraction experiments were carried out at room-temperature, which for the samples in this work is in the paramagnetic state. It has earlier been confirmed (e.g. [57]) that the lattice parameters have non-linear temperature dependency near the magnetic phase transition apart from the expected thermal expansion. Therefore, in the efforts to describe the structure of the investigated manganites a sample stage was built to be able to do XRD below room-temperature in order to look at dependency of the lattice parameters near the magnetic phase transition. The sample chamber could not be kept free of ice at measurements with temperatures below the freezing point and these experiments were therefore rejected. A new Bruker diffractometer

with the ability to measure below room-temperature is however installed now in the department, and these experiments might be the subject of future work in our group. Especially in conjunction with FOMT materials, which are linked to a structural change this could be interesting to investigate in detail.
Since all materials in this work is measured in the paramagnetic state we can assume that the lattice parameters can be compared within the different compositions, but in material series with Curie transitions above and below the measuring temperature, this consideration should be taken into account.
The XRD technique was used to verify that powders were crystallized in the intended perovskite structure after calcination. After dry pressing and sintering the powders in cylindrical form the samples were again characterized by XRD. For this final structural characterization long integration times (15 s/step) and small angle steps of 0.02 degrees were used to obtain good counting statistics, since these diffractograms were used to do the Rietveld refinement explained in the following section. To ensure that the setup was well calibrated, the diffractometer angles were calibrated from the intense (111) reflection at 28.443 in ultra-pure Si powder. The diffractograms were fitted by the Rietveld method [58, 59] using the Fullprof program suite [60].

4.2.1 Rietveld Analysis

By indexing the peaks in an XRD diffractogram some information regarding the structure can be extracted, but to get deeper insight into bond lengths and angles and other more specific details of the structure a Rietveld analysis of the diffractograms is needed
Rietveld refinement is an iterative procedure to refine powder diffraction patterns by the least squares method. The method uses a number of parameters describing both sample and instrument. By calculating an approximate diffraction pattern that corresponds to a set of given parameters, all or some of the parameters are then refined and a new pattern is calculated. This is repeated until the difference between the measured pattern and the calculated pattern reaches a minimum error. The fitted parameters are considered to be equal to the physical parameters of the measured pattern. The parameters are approximated by Taylor expansions in the refinement and therefore good initial guesses of the parameter values are needed for the refinement method to work. Poorly initiated parameters can lead to false local minima in the Rietveld refinement technique. An elaborated review of Rietveld Method of refinement can be found in [61]. All Rietveld refinements in this work have been performed with the Fullprof program suite [60] and all resulted in fitted patterns with $\chi^2 < 6$ (goodness-of-fit).

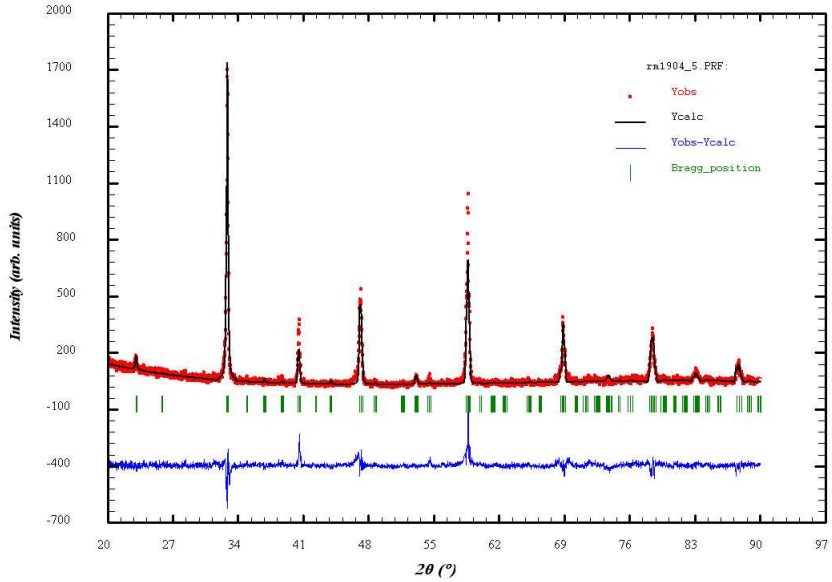

Figure 4.3: Rietveld refinement using Fullprof [60]. In the plot you see the actual diffracted intensity (red line), the calculated intensity (black line), the vertical lines show the Bragg positions (green lines) and the difference between measured and calculated intensities is shown at the bottom (blue line).

4.3 Magnetic Properties Characterization

The magnetic and magnetocaloric properties of the samples were investigated using a Vibrating Sample Magnetometer (VSM). This type of magnetometer was developed by Simon Foner at MIT back in the 1950's [62]. A LakeShore 7407 VSM system was used for the VSM measurements in this work. In the original VSM developed by Foner, two pickup coils situated parallel to the vibration direction of the sample and normal to the magnetic field were measuring the induced voltage from the magnetization of the vibrating sample. Modern VSM systems like the LakeShore system use a four-coil gradiometer array, which have increased the sensitivity of the method significantly. A pair of circular coils mounted on each pole face, one over the other constitutes the array (See Figure 4.4). The sample is oscillated vertically (Indicated by the arrows in Figure 4.4), causing the flux through each coil to vary with time, thereby inducing a small AC voltage. Because the upper and lower coils are wound in opposite directions, the voltages add rather than cancel out. The signal is proportional to the time derivative of flux through the coils. Since the sample displacement velocity is

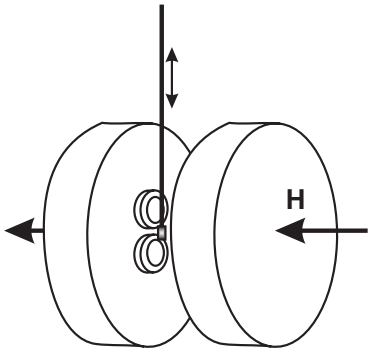

Figure 4.4: The VSM setup with a vertically vibrating sample holder and four-coil gradiometer array of pick-up coils. Two of them are visible on one of the polefaces. The magnetic field, **H**, is applied perpendicular to the motion of the sample.

known its possible to calculate the gradient field produced by the sample at the coils. The LakeShore system has a variable gap between the coils to allow for adjusting the coils to suit sample and magnetic field requirements.
The magnetization **M** is related to the applied magnetic field, **H**[2], and the magnetic flux density, **B**, by

$$\mathbf{B} = \mu_0(\mathbf{H} + \mathbf{M}) \tag{4.2}$$

H takes a known value, so that any change in the flux density **B** inside the sample will be due to a change in the magnetization **M**. The **B** field then generates a voltage over the pick-up coils as the sample vibrates. The e.m.f. in one turn is given by Faraday's law

$$\varepsilon = -\frac{d\Phi_B}{dt} = \frac{\partial}{\partial t}\left(\int \mathbf{B}\cdot\mathbf{dS}\right) \tag{4.3}$$

where Φ is the flux of a vector area element and dS is an element of vector area. The magnetization of the sample is calculated automatically by the software, but to perform the calculation a nickel sample with a known magnetic moment is measured as a calibration standard and the Hall probe are re-calibrated before the measurement using a zero Gauss chamber (A small chamber shielded from magnetic fields). The relevant characteristics of a magnetic material are extracted by measuring hysteresis loops (H_{max} to $-H_{max}$ to H_{max}) at constant temperatures. Since the investigated materials in the present work are soft mag-

[2]In this description of the VSM, the applied magnetic field is termed H and the magnetic flux density is termed **B**. The conventional distinction is here necessary to explain the VSM technique.

netic materials (low remanence[3] and low coercivity[4]), it is often satisfactory to do only half the hysteresis loops (0 to H_{max} to 0), as this loop contains most of the information and is measured in half the time.
The as-synthesized samples can be described by a so-called "virgin" curve. This curve relates to the first time a sample is magnetized and might contain information on the as-synthesized state of the sample. All samples characterized by VSM in this work have been magnetized prior to the measurement during saddling (The symmetric alignment of the sample in the magnetic field).

4.4 Magnetocaloric Properties Characterization

Different methods to determine the MCE have been suggested in the literature [17, 19, 63]:

1. *Direct measurement.* Measurements of the adiabatic temperature change, ΔT_{ad}, by moving the sample in and out of a magnetic field region and recording the changes of the temperature.

2. *Indirect measurement.* Magnetization method: By determining the magnetization curves at various temperatures, the magnetic contribution to the entropy change, ΔS_M, can be extracted.

3. *Indirect measurement.* Calorimetric method: By measuring specific heat capacity as a function of temperature at various magnetic fields.

By measuring a series of isothermal magnetization curves in the VSM with a temperature range from well below to well above the Curie temperature the magnetocaloric properties of the material can be evaluated. We can calculate the isothermal magnetic entropy change that characterizes the magnitude of the MCE, since we know from section 2.2 equation 2.13 that the entropy change can be calculated from the magnetization. McMichael et al. [64] proposed a simple equation for the calculation of ΔS_M using magnetization data:

$$|\Delta S_M| = \sum_i \frac{M_i - M_{i+1}}{T_{i+1} - T_i} \Delta H_i. \tag{4.4}$$

This method is the most commonly used (e.g. [65, 66, 17]), while methods 1 and 3 in the above list require specialized equipment. Direct measurements of ΔT_{ad} have also been performed (e.g. [67]) using simple setups to move samples in and out of magnetic fields while measuring the sample temperature, but

[3]The remanence is the remaining magnetization after the applied magnetic field has been removed.

[4]The coercivity is the magnetic field needed to remove the magnetization of the sample completely.

since its rather difficult to do these measurements adiabatically, more and more groups tend towards calorimetric measurements combined with the standard magnetization measurements.
The construction of a differential scanning calorimeter (DSC) with the ability to measure in applied magnetic fields was therefore one of the primary goals of this work. Different aspects of the construction, calibration and results will be treated in the following chapter.

CHAPTER 5

Differential Scanning Calorimeter with applied magnetic field

As part of this work, a high-sensitivity Differential Scanning Calorimeter (DSC) unit operating under a magnetic field has been built for indirect determination of the MCE. The principle of the measuring unit in the calorimeter is based on Peltier elements as heat-flow sensors. The high sensitivity of the apparatus combined with a suitable calibration procedure allows very fast and accurate heat capacity measurements under magnetic field to be made. The description and results in this chapter have been published in Review of Scientific Instruments [68].

5.1 Introduction

The heat capacity of a material as a function of temperature is important for the determination of the thermodynamic properties of a material as was established in chapter 2. The use of calorimetry to investigate the magnetocaloric effect (MCE) is roughly one out of three possible methods. The need for fast and reliable characterization techniques of the MCE is increasing. As pointed out by Pecharsky and Gschneidner, calorimetry provides a method to minimize the systematic errors in the determination of the isothermal magnetic entropy change from heat capacity data as a complement to magnetization data [17].

Experimentally, the heat capacity is most commonly determined by calorimetry, but although a variety of commercially available instruments are used for this purpose, the ability to conduct thermal measurements as a function of

applied magnetic field is still quite rare [69, 20, 21, 19]. Apart from the obvious advantage of minimizing systematic errors by using heat capacity measurements, the calorimetric approach also provides a fast way to obtain information on MCEs as well as structural changes and charge ordering [70]. It was described in section 2.1 how the entropy can be calculated from temperature and magnetic field dependent heat capacity in equation 2.8 and further from this coupling information on the adiabatic magnetic entropy change can be derived.

5.2 Experimental Details

5.2.1 Construction of the Calorimeter

When designing the calorimeter, a large effort was devoted to optimization according to these criteria:

1. Accurate heat capacity measurements under magnetic field.
2. Determination of the MCE must be optimized around room temperature.
3. The measurement should be performed in near adiabatic conditions.

The calorimeter is schematically depicted in Figure 5.1. The calorimetric block is a solid copper cylinder of high thermal conductivity. This configuration allows for the use of any standard laboratory electromagnet, a superconducting coil magnet or alternatively a permanent magnet. The temperature is measured to within ± 0.1 K by means of a platinum resistance thermometer placed in the DSC cavity. The Peltier element acts like 16 thermocouples placed thermally in parallel and electrically in series, which puts the calorimeter into the family of Calvet calorimeters [71]. This idea to use Peltier elements as heat flow sensors was proposed by Plackowski et al. [19] and has the advantage of obtaining highly reproducible data with high sensitivity in a very inexpensive manner. As opposed to Plackowski and other types of insets to superconducting magnets [69, 20, 21, 19] this setup was designed to be more flexible in the adaption into the applied magnetic field. By keeping the measuring unit as small as 20 mm in diameter and the cold finger reaching 110 mm, this setup can be adapted into various sorts of magnets including electromagnets, which have a much lower running cost than the superconducting magnets. Furthermore the temperature control was optimized to have maximum stability in the room-temperature range contrary to temperature controls heating from liquid nitrogen or helium temperatures. The cavity is surrounded by a cover, which ensures thermal homogeneity and near-adiabatic conditions via thermal isolation from the environment. The design of the temperature control system was based on the ability to choose the temperature range by a secondary cooling liquid (see Figure 5.1) in order to obtain maximum temperature stability during the

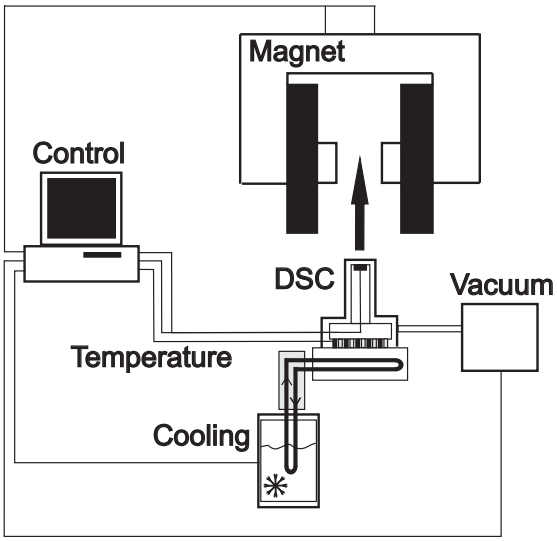

Figure 5.1: Schematic of the DSC setup. In this setup the temperature of the sample (heating and cooling) is controlled by a Peltier element with an additional separate cooling unit. The DSC can be operated with and without magnetic field. The running parameters of the DSC are controlled from a computer. In order to ensure a complete isolation of the sample from the surroundings the sample is also kept in vacuum using a turbo pump system which is coupled to the DSC unit.

measurements. The temperature, process control and the data acquisition are controlled from a LabView interface. A detailed scheme of the cavity is shown in Figure 5.2 and the basic design parameters are given in Table 1. In order to minimize heat losses to the surroundings the calorimeter unit is placed in a vacuum chamber equipped with a radiation reflection shielding made of gold. The DSC signal in the cavity is acquired by two differentially connected heat flow sensors, which represent the sample (S) and the reference (R). In the present setup the samples were mounted directly on the upper surface of the sample holder without the use of a sample pan. In order to ensure a good thermal contact, thermal grease (Apiezon® H-grease) is used. The thermal grease was investigated for a possible phase transition well below the operating temperature range of the DSC, and no visible indication of a phase transition was found in this range. This observation combined with the fact that a very small amount of grease (∼0.1 mg) was used allowed us to treat the grease as part of the background. The heat capacity of the grease is subtracted from the sample signal by including the grease used to mount the sample, when measuring the empty sample holder in the addenda measurement. The cavity temperature is

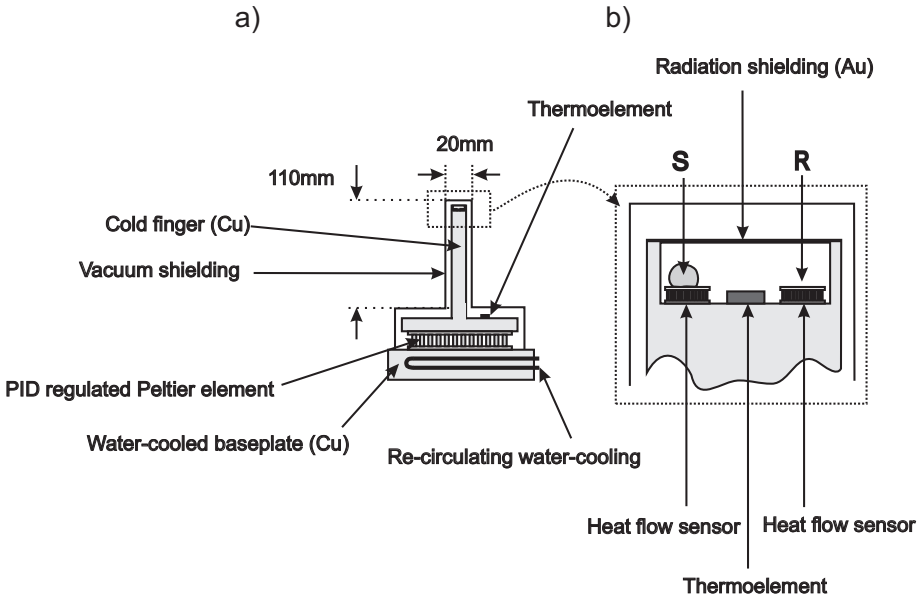

Figure 5.2: Schematic of the measuring unit. The complete DSC unit (a) and a close-up of the sample holder (b). (a) The temperature is controlled by a water-cooled baseplate mounted with a Peltier element. The Peltier element is PID controlling (Proportional-Integral-Derivative control) the temperature of the cold finger by a LabView® interface. The thermoelement for the PID control is placed distant to the measuring unit to level out temperature fluctuations caused by the PID control, and the sample temperature is then logged close by the sample (S) and reference (R) by another thermoelement. The two small Peltier elements marked as sample (S) and reference (R) are independently used as heat flow sensors for measuring of the sample and the reference to provide a differential signal.

simultaneously recorded by a resistance temperature detector which is situated in the proximity of the sample/reference (Thermoelement in Figure 5.2, b). A signal from a second sensor is used as feedback signal for the temperature PID (Proportional-Integral-Derivative) controller (See Figure 5.2, a). Since the operation temperature range of this equipment was designed to be around room temperature, it was sufficient to control the temperature in the range of 200-340 K. The temperature range of this device can be expanded in the future to lower or/and higher temperatures.

Element	Dimension (mm)	Specification
Sensor Peltier elements	3x4	Supercool PE-018-03-09
Temperature control Peltier element	62x62	Supercool PE-127-20-15
Cold finger	110x20$^{\varnothing}$	Copper
Thermoresistor element	2x3	Pt100 element 100W
Power supply		Instek PSH 2018 20V/18A
Multimeter		Keithley 2700 40 channels
Hall sensor	2x3	Arepoc AHP-H3Z
Grease for mounting of the sample		Apiezon H-grease

5.2.2 Data Acquisition

When heat passes through a Peltier element it generates a voltage drop U_p, which is proportional to the heat flow Q_p passing through the specific element to the heat sink:

$$U_p = \frac{S}{k} Q_p \tag{5.1}$$

where S is the Seebeck coefficient and k is the thermal conductance of the Peltier element [19]. At constant external conditions (temperature, pressure, magnetic field) S/k is constant and Up can therefore be used directly as a measure of the heat flow. The heat capacity C_p

$$C_p(T) = \frac{Q_p}{\dot{T}_s} = \frac{k}{S} \frac{U_p}{\dot{T}_s} \tag{5.2}$$

is then derived by the classical 3-step-procedure [71] from three successive temperature scans of the sample: (1) scan of the sample, (2) scan of the reference sample (for the calibration of the heat capacity we have used copper (99.999% Cu) as a reference material [72, 71]) and (3) scan of an empty sample holder for determining the background signal. As described above the background signal includes the amount of Apiezon H-grease used to mount the sample subsequently. During these scans the temperature is ramped at a constant rate. Keeping the experimental conditions identical, i.e. sample weight and heating/cooling rates, in all three scans the heat capacity can then be derived point by point for a range of temperatures [71]:

$$C_{p,sample}(T) = \frac{U_{sample}(T) - U_0(T)}{U_{ref}(T) - U_0(T)} \frac{m_{ref}}{m_{sample}} C_{p,ref} \tag{5.3}$$

5.3 Calibration

The temperature measured in the setup has been calibrated by using the onset melting point of gallium (303.05 K)[73] with high purity (99.999%). The onset of the melting temperature used for the calibration is determined by the crossing point of the base level and slope of the peak during heating as shown in Figure 5.3. The base level and the slope of the peak is determined by linear regression

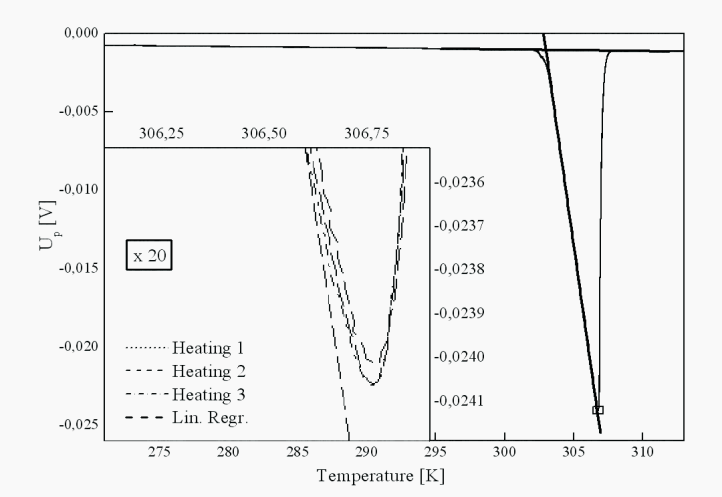

Figure 5.3: Temperature calibration using the onset melting point, T_m (303,05 K), of gallium as reference material. The onset is defined as the crossing between a linear regression of the background data points below T_M and a linear regression of the data points on the left side of the peak above T_M. The inserted figure shows the peak of the melting point magnified 20 times. In the magnified inset it also becomes visible that the data consists of three successive measurements on the same sample.

of the data below and above the melting peak and the linear range of the melting peak between 303.5 K and 306.5 K, respectively. The temperature calibration is only valid for a specific heating rate, and in our experiments we kept the heating rate constant at 1 K/min and the sample and reference of comparable sizes. Besides the temperature calibration Figure 5.3 demonstrates the excellent reproducibility of the measurements. In this case an endothermic process within the sample is recorded and illustrates the melting behavior of the material. Changes in ramping rate, heat loss and thermal conductance would show up in the position of the melting peak. The inset in Figure 5.3 is a magnification of the peak tip to enable the viewer to resolve the difference between the three data sets. Furthermore the melting enthalpy of gallium has been calculated and compared to values from the National Institute of Standards and Technology (NIST). The enthalpy of melting given by the NIST database [74] is 80.097 J/g in a 99.9999% pure Ga standard sample, whereas we calculated the enthalpy from our heat capacity data to be 80.8±0.2 J/g in a 99.999% pure Ga sample, which implies a deviation of less than 1% including deviations due to differences in purity.

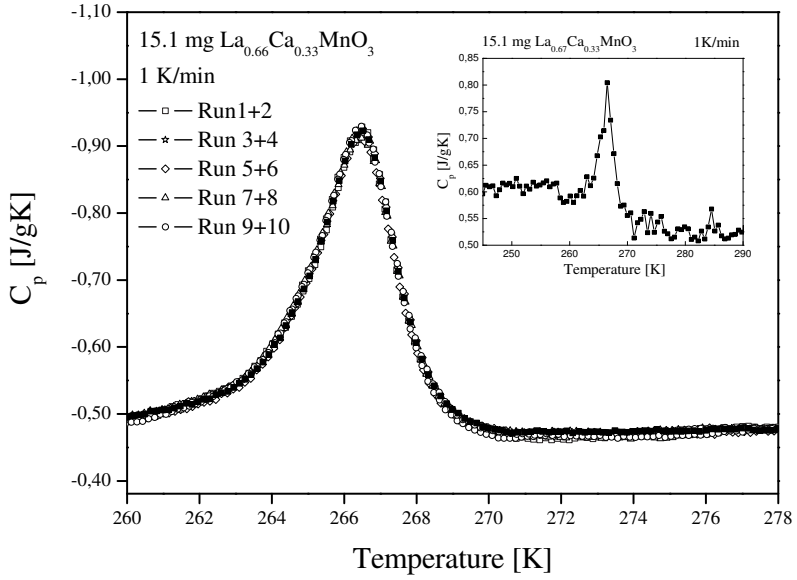

Figure 5.4: Heat capacity as function of temperature in ten successive runs on the same 15.1 mg $La_{0.67}Ca_{0.33}MnO_3$ sample in zero magnetic field obtained by the new calorimeter. The inset shows heat capacity data of the same sample obtained in a Seiko DSC-120 commercial DSC setup.

5.4 Linear Temperature Ramp Experiments

Since this setup was built for the purpose of characterizing the heat capacity of magnetocaloric materials as function of temperature and applied magnetic field, the sensitivity of the DSC needs to be tested on a much weaker signal e.g. from a magnetic phase transition. The magnetic phase transition from the ferromagnetic (FM) to paramagnetic (PM) state in the $La_{0.67}Ca_{0.33}MnO_3$ system represents a signal, which is more than 50 times weaker than the melting of gallium. $La_{0.67}Ca_{0.33}MnO_3$ (LCMO) was chosen since it is considered to be one of the possible candidate refrigerants in the field of room-temperature magnetic refrigeration and has a transition just around 267 K [67] depending on the exact way of synthesis and heat treatment.

Figure 5.4 shows the results from ten successive runs on a 15.1 mg LCMO sample and heating/cooling rate of 1 K/min. The signal due to the FM to PM transformation is measured to be only around 0.3mV, whereas the signal from

the melting of gallium was of the order 20mV, i.e. the FM-to-PM signal is nearly two orders of magnitude smaller. The reproducibility of the signal and an excellent signal-to-noise ratio is however upheld, which demonstrates very well the capabilities of this measuring technique and the set-up. The characteristic "lambda shape" of the phase transition is also clearly recognized.
The signal-to-noise ratio of the new DSC developed in our laboratory can be estimated by defining a noise band covering all measured data values in a linear part of the dataset. This noise band includes the electrical noise of the measurement as well as the main contribution to the noise, namely fluctuations in the signal derived from thermal fluctuation during the heating/cooling experiment. The width of the noise band can then be evaluated with the signal strength in a given phase transition investigated at a given heating rate. The width of the noise band has been estimated to be maximum $2.5\mu V$ over a 7 K range during heating at 1 K/min. With a signal strength similar to the magnetic phase transition peak shown in Figure 5.4 peaking around 0.3 mV, this will lead to a signal-to-noise ratio above 100/1. The much stronger signal from the melting of Ga shown in Figure 5.3 is exceeding 20mV at the peak, leading to a signal-to-noise ratio of more than 800/1 in that experiment. A zero-field heat capacity measurement of the same sample (Figure 5.4 inset) measured in a commercial DSC setup (Seiko 120-DSC) led to a signal-to-noise ratio of less than 10/1 for the same sample and experiment conditions. Sample sizes between 10 and 100 mg are typically used in conventional DSC measurements depending on the exact material and experiment. As demonstrated when comparing the results in Figure 5.4 and the inset in Figure 5.4, the relatively low weight when considering conventional DSC measurements of the 15.1 mg LCMO sample results in a very high signal-to-noise ratio in the setup described in this work, whereas to obtain equally good results in the commercial DSC it would be necessary to increase the sample size significantly or to change the heating rate. On the results presented in Figure 5.4 it furthermore becomes evident that even smaller samples would still give a satisfactory signal-to-noise ratio when measuring on FM to PM transitions. The reproducibility and an excellent signal-to-noise ratio is hereby validated, confirming the results from the Ga runs (Figure 5.3). Further, the enthalpy corresponding to the magnetic phase transition for the LCMO sample is more than 50 times smaller than that of the melting enthalpy of Ga, and the reproducibility of the LCMO transition is therefore an important figure of merit for the performance of the new calorimeter. The calorimeter has also been tested under applied magnetic fields. Figure 5.4 shows the influence of an applied magnetic field on the magnetic phase transition for the LCMO sample. As expected, the applied magnetic field changes the Curie temperature (T_C) to higher temperatures and tends to broaden the shape of the phase transition. These results correspond well with the results obtained by direct measurements previously reported [30]. The absolute comparison of our results

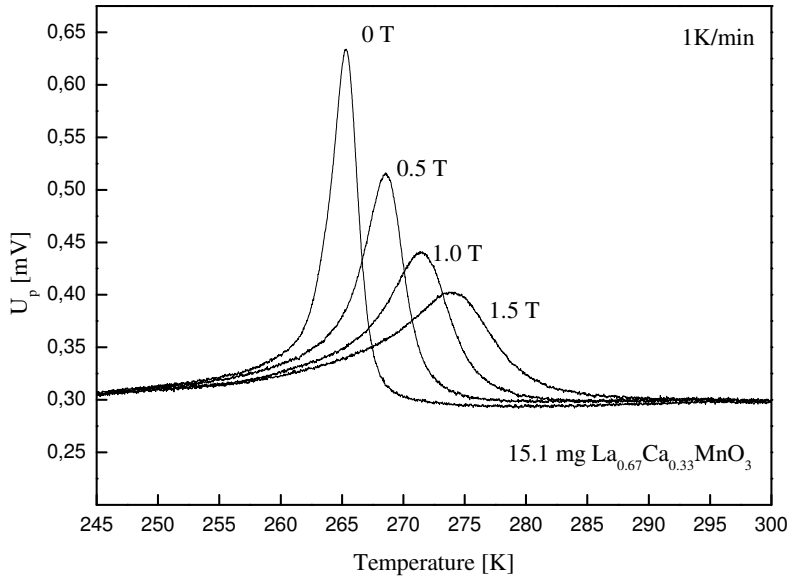

Figure 5.5: Heat capacity data of the 15.1 mg $La_{0.67}Ca_{0.33}MnO_3$ sample measured in four different magnetic fields with the new calorimeter.

and the results reported in the literature for the same material composition are not possible since the properties of these materials are very sensitive to the preparation procedure e.g. heat treatment. For a direct comparison with alternative measuring techniques the same ceramic material was measured in a Quantum Design® Physical Properties Measuring System (PPMS). The results are shown in Figure 5.6 and demonstrate an excellent agreement between the two techniques. The PPMS uses a relaxation technique and requires up to 40 minutes per measuring point, whereas scans with the Risø DSC is normally carried out with a scan rate of 1 K/min and 2 Hz data logging frequency. This difference is also easily recognized in Figure 5.6 where the dataset from the Risø DSC shows much higher density of the data. A picture of the DSC setup is shown in Figure 5.7

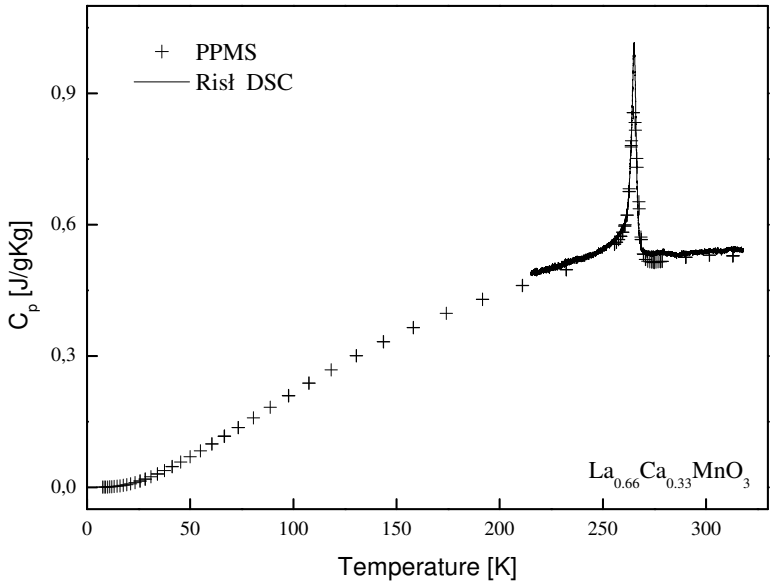

Figure 5.6: $La_{0.67}Ca_{0.33}MnO_3$ sample measured in a Quantum Design PPMS system and compared to the measurement from the DSC setup described in the present work.

5.5 Conclusion

A novel DSC was constructed for the purpose of characterizing magnetocaloric materials in the near room temperature range (200-340 K). A significant improvement of the signal-to-noise ratio has been observed when compared to a conventional zero magnetic field DSC. Test results on pure Ga and $La_{0.67}Ca_{0.33}MnO_3$ have been presented to demonstrate the performance of the setup. Test runs as a function of applied magnetic field demonstrate the ability of this device to operate correctly under applied magnetic fields up to 1.8 Tesla. The results from the DSC are in good agreement with results obtained in a commercial PPMS system from Quantum Design®.

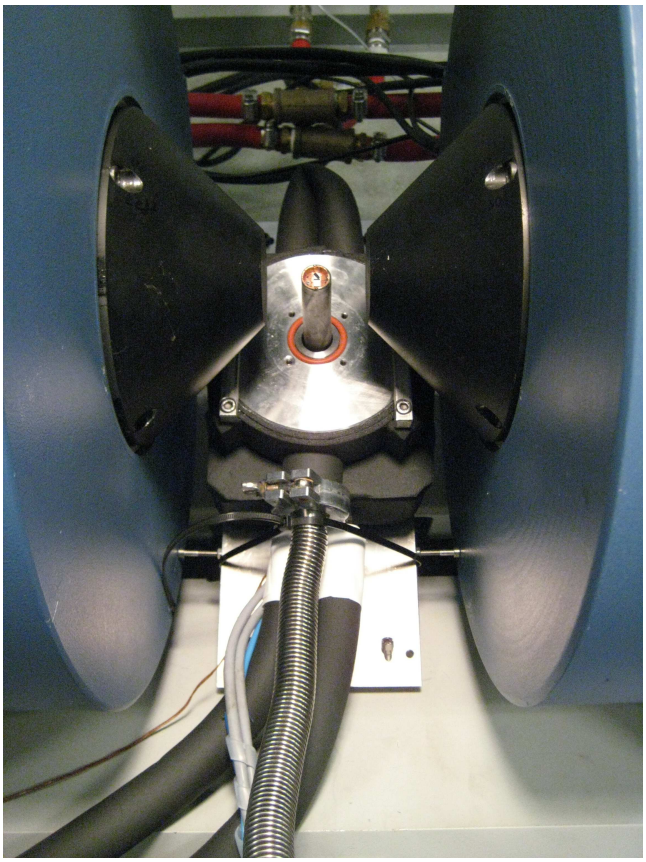

Figure 5.7: Picture of the DSC unit placed in the pole gap of the laboratory electromagnet.

CHAPTER 6

The Magnetocaloric Effect in Cu-doped Manganites

The magnetocaloric materials studied in this work takes basis in the well known $La_{1-x}Ca_xMnO_3$ system [25]. The magnetocaloric properties of manganites have been extensively reviewed in a recent paper by Phan and Yu 2007 [75]. The investigated systems include not only the $La_{1-x}Ca_xMnO_3$ compositions, but a wide variety of variations with substitution of both A-site and B-site ions. Earlier studies on Cu substitution in the La-Sr-Mn-O manganite system have demonstrated an increase in the magnetic entropy from 3.05 J/kgK in a 5% Cu doped sample to 3.24 J/kgK in a 10% Cu doped sample obtained for a field change of only 1 T [76]. Furthermore, Cu-doping has also been investigated in the La-Ca-Mn-O system in studies of magnetoresistance showing anomalous behavior at low levels of Cu-doping [77, 78, 79]. There is no prior study on the influence of Cu doping on magnetocaloric properties of La-Ca-Mn-O system to my knowledge.

6.1 Phase Diagram of the La-Ca-Mn-O System

The La-Ca-Mn-O system has a variety of different structural, magnetic and electronic phases depending on the composition. The compositions synthesized in this work, x=0.33, lie in the middle of the ferromagnetic (FM) region (See FM on Figure 6.1). This composition lies in the phase diagram near the maximum possible transition temperature. This indicates that the material has a very strong ferromagnetic coupling. Furthermore, the composition is far away from possible competing magnetic phases such as charge ordered (CO) and ferro-

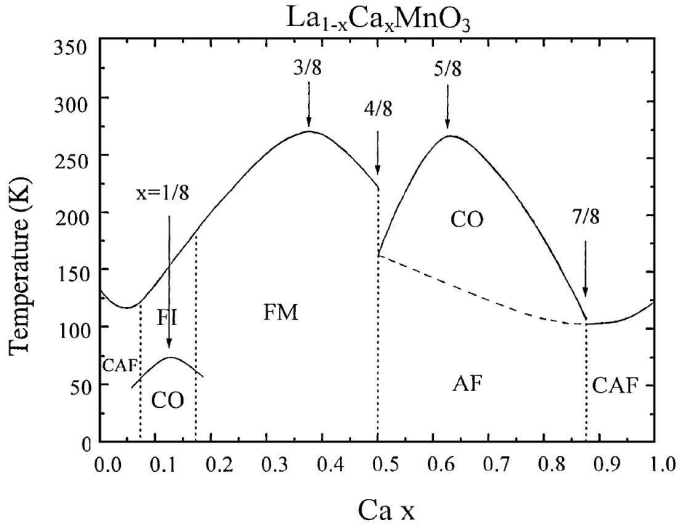

Figure 6.1: The complex phase diagram of the La-Ca-Mn-O system. The compositions synthesized in this work lies in the middle of the ferromagnetic (FM) region at x=0.33. The phase diagram is adopted from Dagotto et al. [80].

magnetic insulator (FI) regions at lower Ca levels or CO and antiferromagnetic (AF) regions at Ca levels above 4/8. The phase diagram therefore gives reason to assume that the ferromagnetic phase will continue to be ferromagnetic upon doping, at least at low doping levels. By knowing the phase diagram, we are also provided with a tool to interpret results if some regions of the materials is found to have high or low levels of calcium.

6.2 Sample Preparation

The sample preparation described in this section have been schematized in Figure 6.2. To investigate the effect of Cu doping in the $La_{0.67}Ca_{0.33}MnO_3$ system, three samples were synthesized with 0, 5 and 10% Cu doping i.e. $La_{0.67}Ca_{0.33}$-$Mn_{1.05}Cu_{0.00}O_3$, $La_{0.67}Ca_{0.33}Mn_{1.05}Cu_{0.05}O_3$ and $La_{0.67}Ca_{0.33}Mn_{1.05}Cu_{0.10}O_3$, respectively. The samples were characterized by DSC measurements using a Netzsch 200F3 Maia DSC setup (See Figure 6.3) to investigate the effect on Curie transition at different doping levels. This was done in order to design a relevant series of materials compositions. In the DSC measurements the samples were heated from -60 to 60°C at a constant ramp rate of 1K/min using Argon as purging gas to avoid ice in the sample chamber, and the sample weights were approximately 30mg. From these results it was found that doping the system

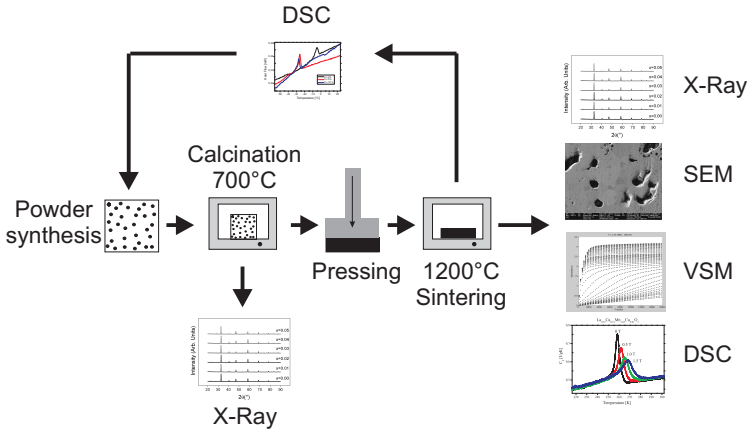

Figure 6.2: A schematized description of the sample preparation. The diagram is explained in the text.

up to 5% Cu drastically changes the Curie temperature of the system, i.e. it reduces the Curie temperature by more than 20°C. From 5 to 10% the transition only decreases around 2°C, so in order to understand the reason for the large changes in the Curie temperature over a relative small amount of Cu doping, it was decided to concentrate on the range of 0 to 5% Cu doping. Six samples with the following compositions were synthesized for this purpose:

1. $La_{0.67}Ca_{0.33}Mn_{1.05}O_3$
2. $La_{0.67}Ca_{0.33}Mn_{1.05}Cu_{0.01}O_3$
3. $La_{0.67}Ca_{0.33}Mn_{1.05}Cu_{0.02}O_3$
4. $La_{0.67}Ca_{0.33}Mn_{1.05}Cu_{0.03}O_3$
5. $La_{0.67}Ca_{0.33}Mn_{1.05}Cu_{0.04}O_3$
6. $La_{0.67}Ca_{0.33}Mn_{1.05}Cu_{0.05}O_3$

In order to ensure high sintering ability, the Mn content was kept 5% above the stoichiometric composition [81]. All powders were synthesized using the glycine-nitrate combustion synthesis as described in Section 4.1.1. Subsequently the powders were calcined at 700°C and then checked for phase purity by XRD. The XRD patterns were obtained according to the description in Section 4.2. Figure 6.4 shows the XRD patterns of the as-calcined samples. It was verified that all powders have crystallized in the perovskite structure. Subsequently, the powders were dry pressed and sintered at 1200°C according to the procedure described in Section 4.1.2.

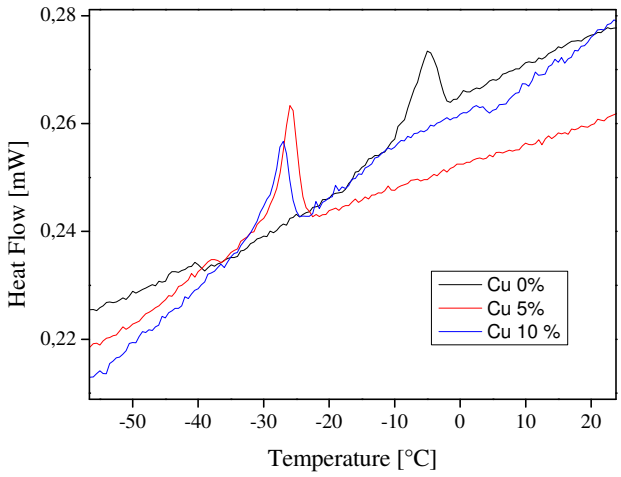

Figure 6.3: Preliminary DSC measurements to screen the Curie transitions in compositions of various Cu doping level. $La_{0.67}Ca_{0.33}Mn_{1.05}Cu_{0.00}O_3$ (black line), $La_{0.67}Ca_{0.33}Mn_{1.05}Cu_{0.05}O_3$ (red line) and $La_{0.67}Ca_{0.33}Mn_{1.05}Cu_{0.10}O_3$ (blue line).

6.3 Structural Characterization

After synthesizing the bulk samples by dry pressing and sintering, the final structure of the material were characterized by XRD. The diffraction patterns were obtained using long integration times for each step (15 s) and small angle steps (0.02°). This was done to ensure high quality pattern for Rietveld refinement. The basic composition of the samples synthesized in this work, i.e. Cu doping ranging from 0 to 5%, is similar to the $La_{0.67}Ca_{0.33}MnO_3$, which in earlier studies [82] have been confirmed to crystallize in the orthorhombically distorted perovskite structure with space group Pbnm.

The XRD patterns of the six sintered samples are shown in Figure 6.5. From the patterns it is seen that all samples are essentially in single phase form, since all the visible peaks can be indexed into one single phase. In Figure 6.5 only the strongest peaks are indexed, the peaks consist of reflections from 2-4 indexable planes all belonging to the orthorhombically distorted Pbnm perovskite structure. Figure 6.6 shows a closeup of two diffractograms from the samples with 0 and 5% in blue and purple, respectively. In the bottom panel the indexed

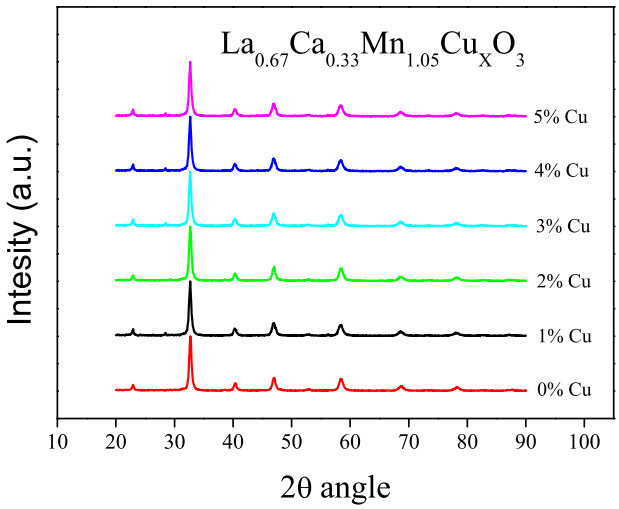

Figure 6.4: XRD patterns of the as-calcined samples. The calcined powders are checked for phase purity before continuing the synthesis. The XRD patterns show that all powders are well-crystallized in the perovskite structure. No further analysis is made at this step of the synthesis.

peaks from the crystallographic ICDD[1] card [89-6933] is shown. This diffraction data card belongs to studies of the composition $La_{0.67}Ca_{0.33}MnO_3$ [83]. This confirms that the visible peaks including even the smallest ones can be indexed into the same phase, and therefore any impurity phases cannot be detected by XRD from these data. In Figure 4.3 in Section 4.2.1 the Rietveld refinement from the sample with 5% Cu was demonstrated. All parameters extracted from the Rietveld refinement of the six samples are listed in Table 6.1. The unit cell parameters of the 6 different compositions is found to be very close, but there is a slight tendency, that with increasing Cu content the unit cell volume is decreasing. This is reasonable due to the substitution of the high spin Mn^{3+} ion (0.0645 nm) with the smaller Cu^{3+} ion (0.054 nm), which has also been observed in previous studies in similar compositions [84]. It is pointed out in [84] that the Cu ions may exist in different valence states, where the larger Cu^{2+} (0.073 nm) might be present simultaneously with the Cu^{3+} ions. The decreased unit cell can only indicate that the average ionic size on the B-site has decreased, which could be the case even in the presence of a fraction of Cu^{2+} ions.

[1] International Center for Diffraction Data

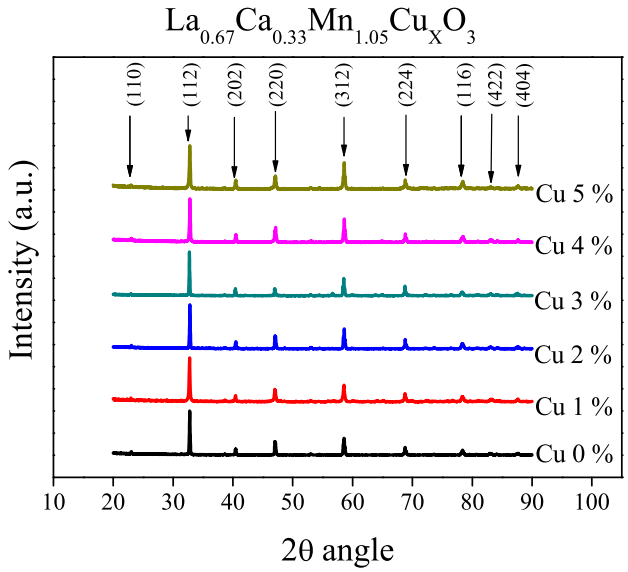

Figure 6.5: XRD patterns of the sintered samples. The XRD patterns show that all powders are well-crystallized in the perovskite structure. The consecutive Rietveld refinement were made from these XRD patterns.

The angles of the Mn-O-Mn bonds have also been extracted from the Rietveld refinement. As the Cu doping is increased, the bond angle decreases (See Figure 6.7). It has been showed in earlier studies [30] that a correlation between bond angle and Curie transition exist, where a decrease in the Mn-O-Mn bond angle leads to a decrease in transition temperature. The orbital overlap and therein the magnetic interaction between manganese ions is maximized in the undistorted cubic structure, where the Mn-O-Mn bond is 180°. A decrease in this bond angle will tend to decrease the orbital overlap thereby weakening the magnetic coupling and lowering the transition temperature. In [30] the bond angle is changed by changing the A-site ion, whereas in these studies the bond angle is altered by Cu doping of the B-site. Remembering the Goldsmith tolerance factor t^* from Equation 3.1 we can calculate the tolerance factors for the six doping levels. The values are plotted (See Figure 6.8) as function of doping level with the Mn^{3+} ions either replaced by the smaller Cu^{3+} ions (squares) or the larger Cu^{2+} ions (triangles). As a consequence the tolerance factor is either seen to increase (Cu^{3+}) with increasing doping level or decrease (Cu^{2+}). The minimization of the unit cell indicated that the Cu ions were in a divalent state,

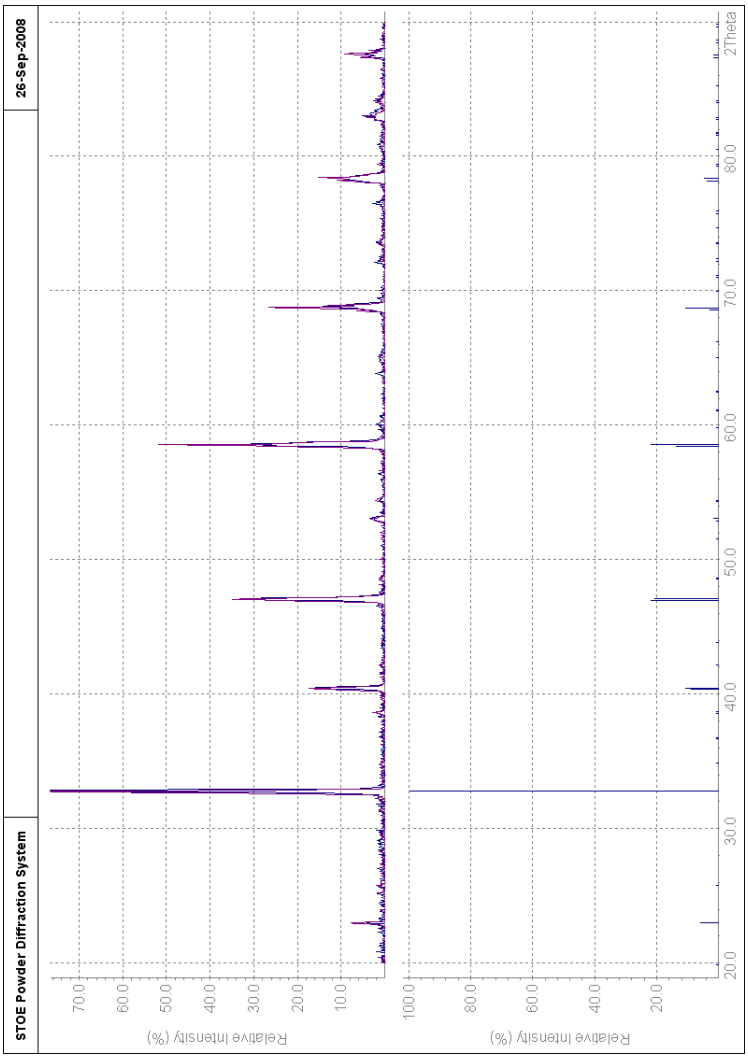

Figure 6.6: XRD patterns from the samples with 0 and 5% Cu doping. The magnification of the diffractogram confirms that only one phase is detectable. Below the XRD patterns the indexed peaks from the crystallographic ICDD card [89-6933] is shown. The indexation is made from a perovskite sample of $La_{0.67}Ca_{0.33}MnO_3$ sample (Spacegroup Pbnm) [83].

whereas the decrease of transition temperature with increasing Cu doping indicates a trivalent state of the Cu ions. However, it has been proposed in studies of the La-Sr-Mn-O system [85], that a mixed-valence state of the Cu ions can account for that type of contradictory indications. The mixed valence state of the Cu ions in the La-Sr-Mn-O system was also later verified by means of X-ray

$La_{0.67}Ca_{0.33}Mn_{1.05}Cu_xO_3$						
x	0	0.01	0.02	0.03	0.04	0.05
Phase						
Spacegroup	Pbnm	Pbnm	Pbnm	Pbnm	Pbnm	Pbnm
Unit Cell						
a [nm]	0.5465	0.5466	0.5466	0.5466	0.5467	0.5467
b [nm]	0.5448	0.5449	0.5448	0.5448	0.5447	0.5446
c [nm]	0.7701	0.7699	0.7699	0.7698	0.7695	0.7692
V [nm^3]	0.2293	0.2293	0.2293	0.2293	0.2292	0.2291
Bond angles [Degrees]						
Mn-O-Mn	178	175	174	175	171	169
Bond lengths [nm]						
Mn-O	0.1925	0.1926	0.1943	0.1926	0.1930	0.1931
Goodness-of-fit (Dimensionless)						
χ^2	4.26	4.55	3.94	5.55	3.88	2.80

Table 6.1: Refined structural parameters of the $La_{0.67}Ca_{0.33}Mn_{1.05}Cu_xO_3$ samples with six different Cu doping levels x. All structures are refined using the orthorhombic Pbnm spacegroup. The refined parameters are the unit cell dimensions (a, b, c), unit cell volume (V), the bond angles for the Mn-O-Mn bonds, the bond lengths Mn-O and finally the χ^2 value representing goodness-of-fit.

Photoelectron Spectroscopy [84].

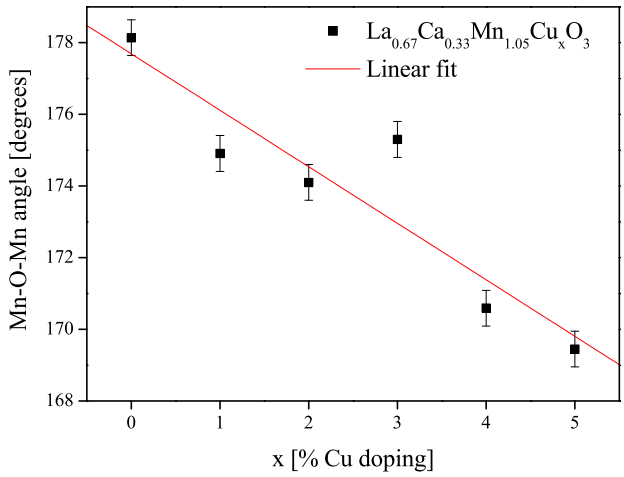

Figure 6.7: Bond angles, Mn-O-Mn, vs. x in $La_{0.67}Ca_{0.33}Mn_{1.05}Cu_xO_3$.

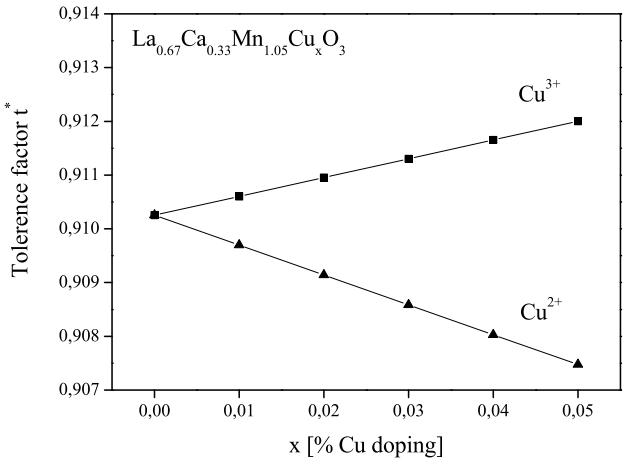

Figure 6.8: Calculated tolerance factors as function of Cu doping level. The square symbols indicate that the Mn^{3+} ions have been replaced by the smaller Cu^{3+} ion, whereas the triangular symbols indicate that the Cu ions will attain Cu^{2+} valence, which is a larger ion than the Mn^{3+}.

6.4 Morphology

The Cu-doped samples have been investigated by scanning electron microscopy (SEM) using a Zeiss 1540 XB microscope with X-Ray microanalysis. When obtaining micrographs of the six samples a low accelerating voltage of 1.5keV has been used to avoid charging of the samples. The micrographs are shown in three different magnifications 5.000, 10.000 and 20.000 using secondary electrons (See Figures 6.9, 6.10 and 6.11). By using energy dispersive spectroscopy (EDS) the compositional changes in the samples have also been investigated. The EDS technique provides a quick and precise elemental analysis of element levels above 1%. In EDS the energy of escaping x-rays exited by the electron beam is measured. The maximum resolution of EDS is therefore confined by the size of the interaction volume (the sample volume from where the x-rays have been generated). The interaction volume is determined by the accelerating voltage and the material, so to increase the resolution it is necessary to decrease the accelerating voltage. However, in order to perform the EDS analysis its also necessary to be able to excite the element, that needs to be quantified. The accelerating voltage was therefore increased significantly to be able to excite the Cu in the sample, which of course is of special interest in these Cu doped samples. To be able to use the photon energy emitted from the Cu Kα_1 line, which is 8047.78 eV, we need as a rule of thumb around double that energy (i.e. 16.196 keV) to conduct EDS on this line. Therefore an accelerating voltage of 16.5 keV was used. This decreases the maximum resolution to the micrometer range (Interaction volume in the vicinity of $1.5\mu m^2$). Due to the increased accelerating voltage the samples also had to be coated with a carbon layer to avoid charging.

By studying the micrographs it becomes clear (e.g. Figure 6.9) that the porosity of the samples is changing with Cu doping, i.e. as the Cu content increases the size of the pores increase while the number of pores decrease. By image analysis[3] the pore sizes has been investigated (See Figure 6.12). In Figures 6.12(a) to 6.12(f) the pore size distributions corresponding to Cu doping levels from 0 to 5% are shown. Figure 6.12(g) shows the mean diameters of the pores extracted from the pore size distributions assuming circular pores. The low number of investigated pores above 3% Cu doping (See Figure 6.9) explicates the large error bars in Figure 6.12(g) and the poor pore size distributions in Figures 6.12(e) and 6.12(f). It was already evident from the SEM micrographs in Figure 6.9 that a change in porosity was seen around 3% Cu doping. This is confirmed by this analysis and the pore diameter is seen to be close to $1\mu m$

[2]To investigate the interaction volumes, the software package CasinoV242 has been utilized. Casino is a software to do Monte Carlo simulations of electron trajectories in solids. It can be downloaded free from http://www.gel.usherbrooke.ca/casino/index.html.

[3]The image analysis was made with Scion Image®, which can be downloaded from www.scioncorp.com

with 0 to 2% Cu doping. When increasing the Cu content the pore diameter increases to around $4\mu m$. The error on the diameter in the compositions with 4 and 5% Cu is very large, but the $4\mu m$ seems to be a good estimate, if some of the pores in Figures 6.9(e) and 6.9(f) are measured by hand.
The effect of the changing porosity can be explained by the increasing over-stoichiometry of the samples with increasing Cu doping. The over-stoichiometry increases from 5 to 10% on the B-site with Cu doping and increasing over-stoichiometry is known [81] to enhance the sintering abilities of the manganite. In this study, the interest is to know whether the Cu ions are located in the perovskite structure or aggregated in separate phases or as inclusion of pure Cu in the materials. The XRD patterns didn't reveal any new phases as consequence of the Cu doping. But since there was a change in the unit cell parameters and bond angles, we wanted to clarify whether the Cu is dissolved in the structure or concentrated in certain parts of the sample. This was done by means of EDS linescans, i.e. sequences of consecutive EDS measurements obtained in a line through certain points of interest in a micrograph (e.g. grains, grain boundaries, pores etc.). In Figures 6.14 and 6.15 the sites of the linescans have been shown for all six compositions. Sites which show compositional contrast in the micrograph were picked out for every sample. There was no visible compositional contrast in the sample with zero Cu doping (See Figure 6.14(a)). Instead an area with some visible inhomogeneous morphology was picked out to investigate the compositional homogeneity near and away from pores in the structure. As can be seen in Figure 6.14(d) the composition through the entire linescan is very constant in all elements. The ratios between La, Ca and Mn agree well with the nominal compositions of the synthesis. In Figures 6.14(c) and 6.14(d) the micrograph area and matching EDS linescan, respectively, is shown for 1% Cu doping. Grains with some visible contrast were observed. Away from these grains the composition is homogeneous as in the previous sample without Cu. In the vicinity of the grain (around $4\mu m$ into the linescan) the atomic percent of Mn increases drastically by more than 20%, around 11 μm a smaller increase is seen on a smaller grain. Analogous to Mn, the Cu content increases slightly in the grain. The values have been normalized to yield 100% between these 4 elements, so other elements like carbon, oxygen or impurities in the material are not taken into account. As the Cu content of the samples is increased to 2% (See Figures 6.14(e) and 6.14(f)) an increased Mn content is again observed in the investigated grain accompanied by a slight increase in the Cu content as well. In the sample with 3% Cu doping (See Figures 6.15(a) and 6.15(b)) the Cu content in the vicinity of the observed grain increases drastically to 14%. This indicates that the Cu in the composition either starts to form a new phase in the observed grain together with Mn or that the Cu ions agglomerate in the grain boundaries. Since there was no evidence of new phases from the XRD patterns the Cu doesn't seem to crystallize in large quantities neither in

pure Cu nor together with other elements. Instead the Cu might be smeared out in the grain boundaries agglomerating in thicknesses of only a few atomic distances or in very small nanometer sized particles that would be invisible in small quantities in the XRD patterns. In Figures 6.15(c), 6.15(d)), 6.15(e) and 6.15(f)) the Cu content is further increased to 4 and 5%, respectively. The Cu content increases correspondingly in the investigated grains. To elaborate on this point a superposition of three linescans from the samples with 3, 4, and 5% Cu is shown in Figure 6.13. These measurements indicates that above a certain doping level the Cu ions are no longer dissolved in the perovskite structure. It was earlier pointed out that Cu doping levels as high as 20% didn't result in any observable phase change [86]. All the samples in [86] were, however, nominally stoichiometric and much larger amounts of Cu might therefore be possible to dissolve. In our samples the Cu ions seems to agglomerate in the grain boundaries of certain Mn rich grains instead. The reason why the grain boundaries are suggested rather than the bulk grain is the results from the linescans. Linescans across selected particles show a larger Cu ratio in the grain boundary region compared to the middle of the grains (See Figures 6.15(d) and 6.15(f)) for the large grains, this indicates that the Cu contrary to the Mn content is highest in the boundaries rather than the bulk grain. From the micrographs of the samples presented in Figure 6.11 it seems as if the over-stoichiometric Cu and Mn contents acts as a sintering aid in the structure. The samples become more and more dense with Cu doping.

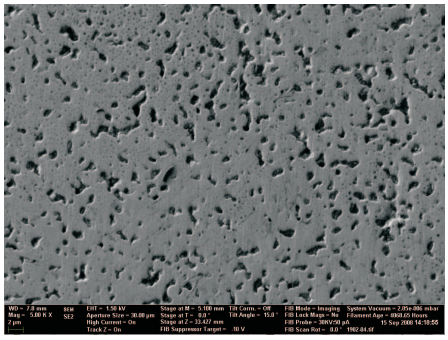

(a) x=0.00

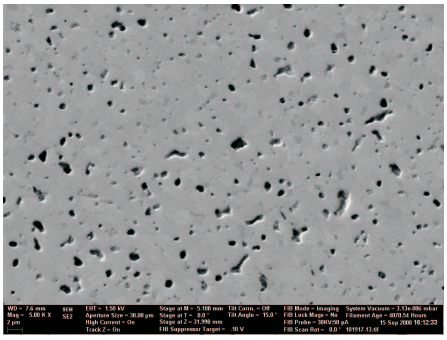

(b) x=0.01

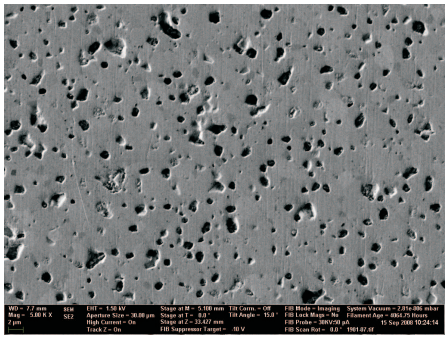

(c) x=0.02

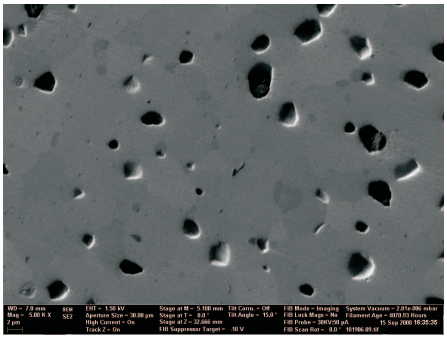

(d) x=0.03

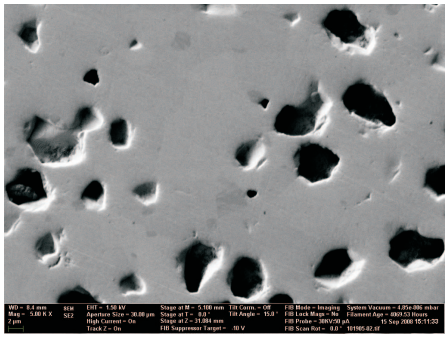

(e) x=0.04

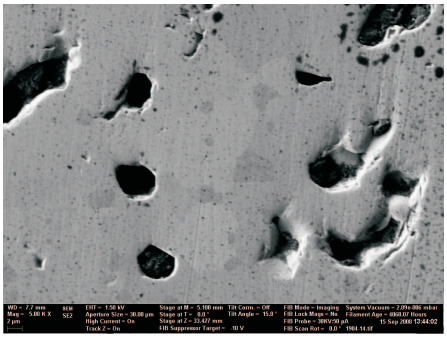

(f) x=0.05

Figure 6.9: SEM micrographs of $La_{0.67}Ca_{0.33}Mn_{1.05}Cu_xO_3$. The magnification is 5.000 times.

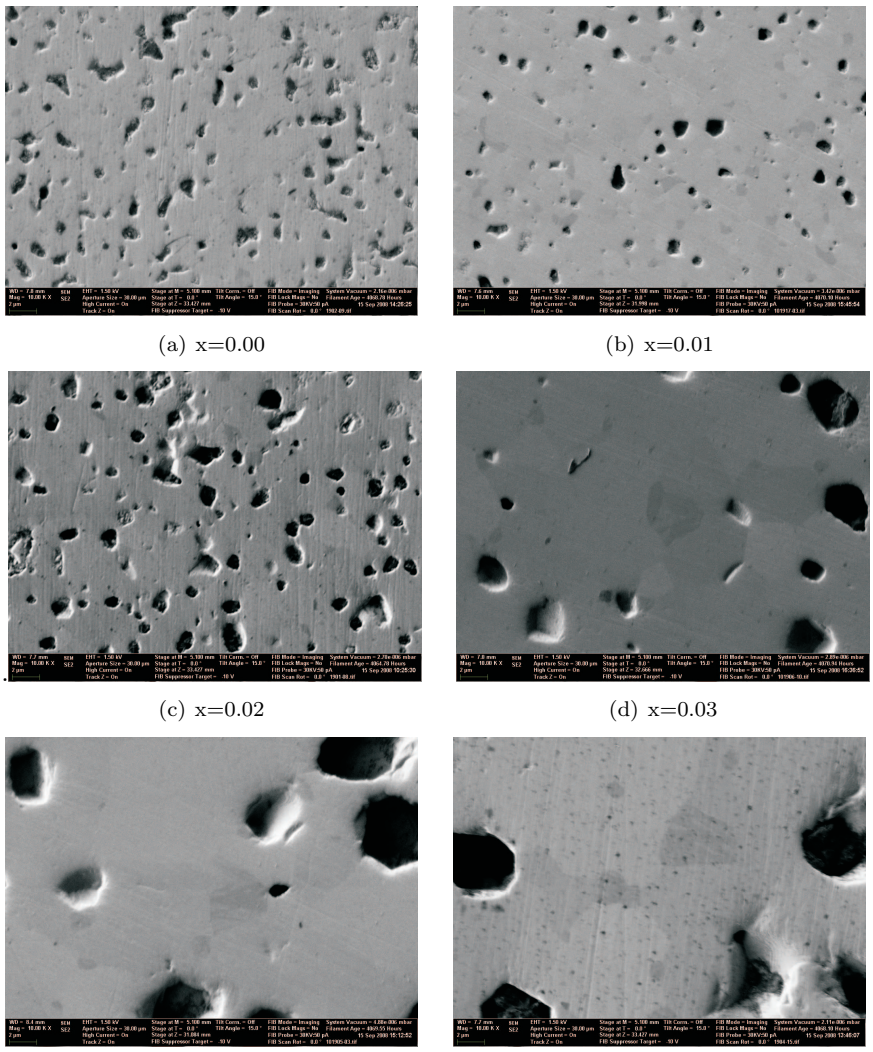

(a) x=0.00 (b) x=0.01

(c) x=0.02 (d) x=0.03

(e) x=0.04 (f) x=0.05

Figure 6.10: SEM micrographs of $La_{0.67}Ca_{0.33}Mn_{1.05}Cu_xO_3$. The magnification is 10.000 times.

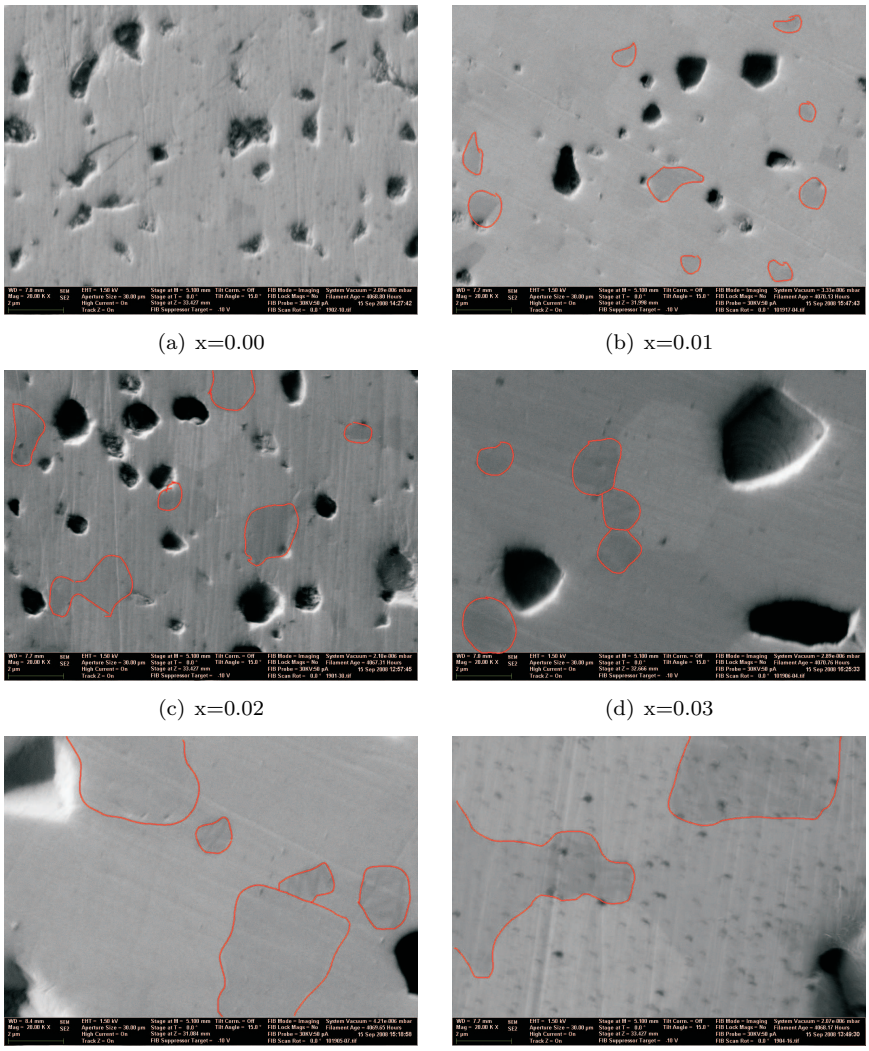

(a) x=0.00 (b) x=0.01

(c) x=0.02 (d) x=0.03

(e) x=0.04 (f) x=0.05

Figure 6.11: SEM micrographs of $La_{0.67}Ca_{0.33}Mn_{1.05}Cu_xO_3$. The magnification is 20.000 times. The red markings indicate some selected grains with visible contrast.

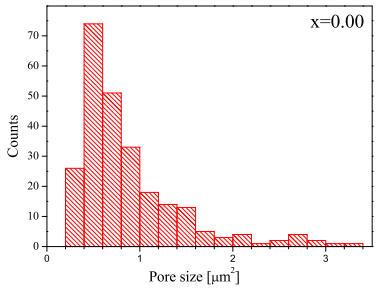

(a) x=0.00

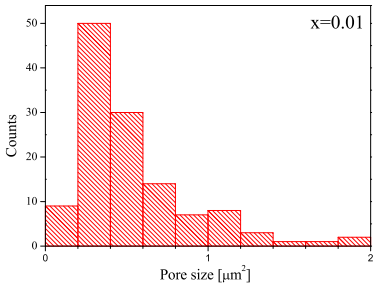

(b) x=0.01

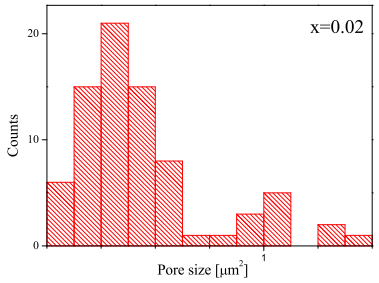

(c) x=0.02

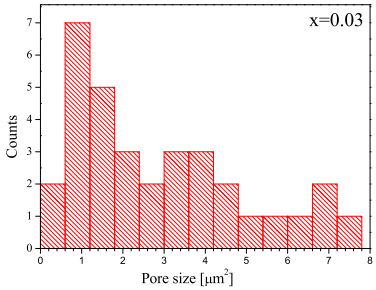

(d) x=0.03

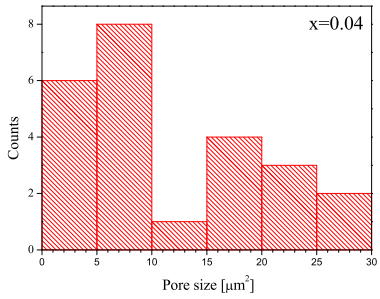

(e) x=0.04

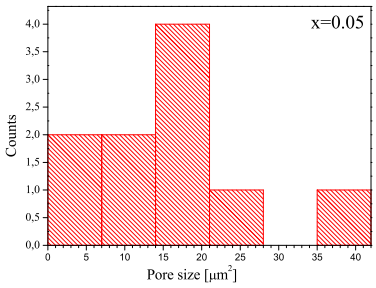

(f) x=0.05

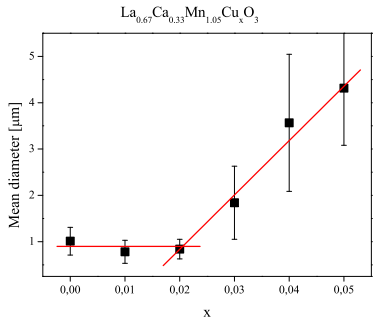

(g) Mean diameters.

Figure 6.12: (a)-(f) Pore size distributions of $La_{0.67}Ca_{0.33}Mn_{1.05}Cu_xO_3$. (g) The mean diameters extracted from the distributions in (a)-(f). The red lines in (g) are guides to the eye.

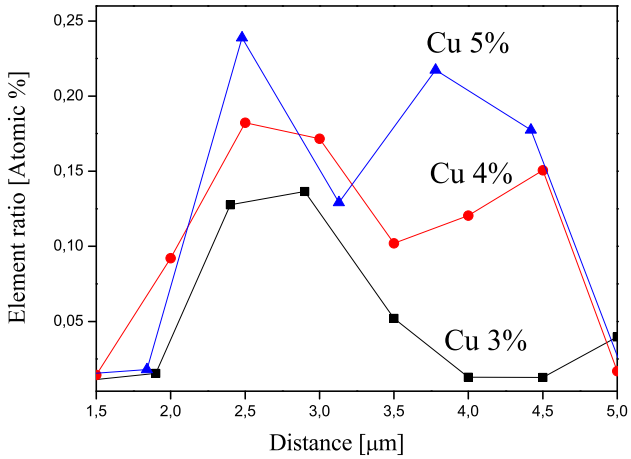

Figure 6.13: Superposition of three linescans from samples with 3, 4 and 5% Cu.

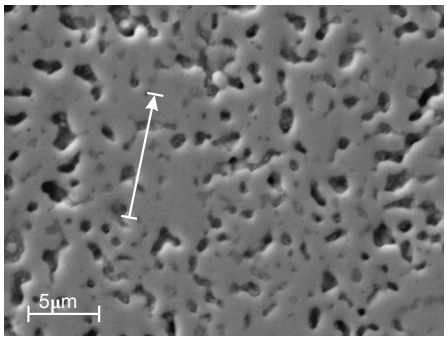

(a) x=0.00

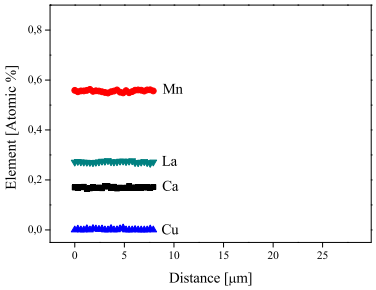

(b) x=0.00

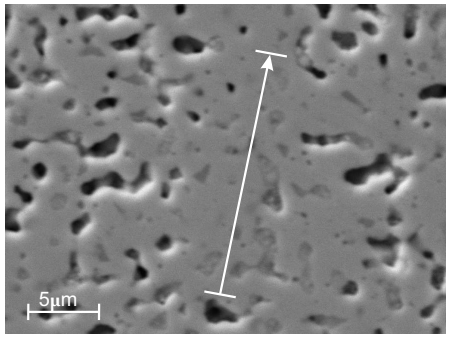

(c) x=0.01

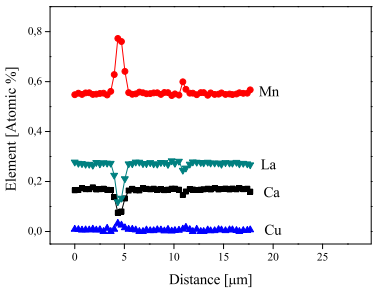

(d) x=0.01

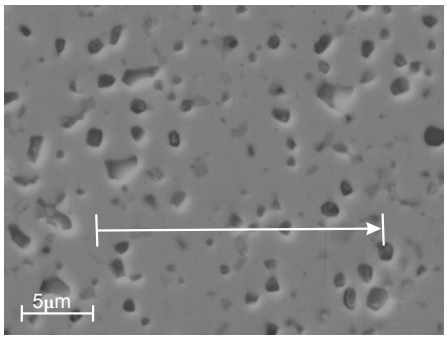

(e) x=0.02

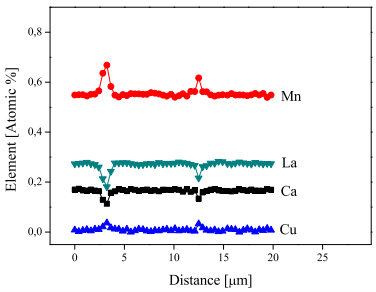

(f) x=0.02

Figure 6.14: EDS linescans in $La_{0.67}Ca_{0.33}Mn_{1.05}Cu_xO_3$, x=0,1,2. On the left the SEM micrograph shows, where the linescan was performed. On the right the EDS results are shown for La, Ca, Mn and Cu ratios.

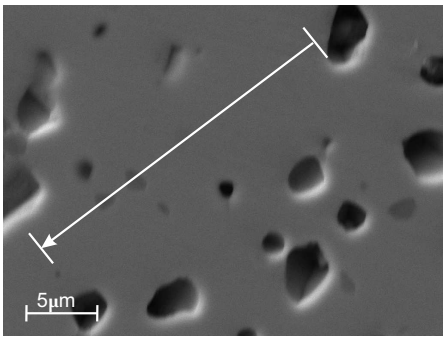

(a) x=0.03

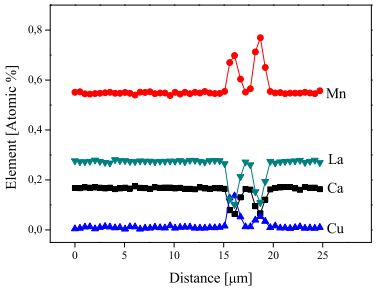

(b) x=0.03

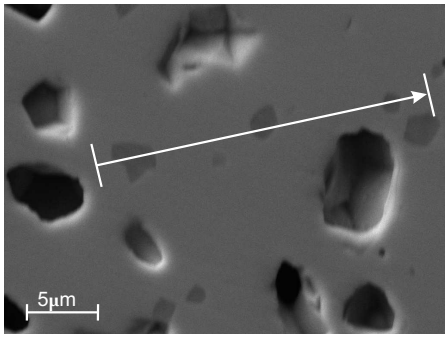

(c) x=0.04

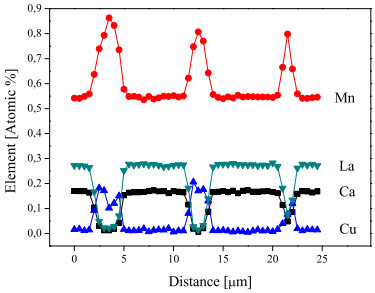

(d) x=0.04

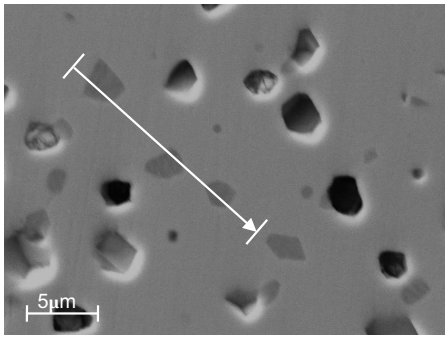

(e) x=0.05

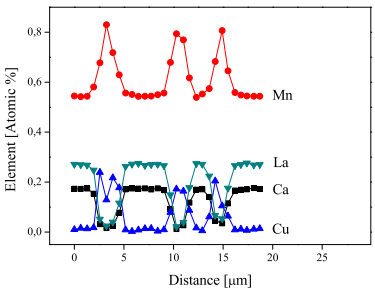

(f) x=0.05

Figure 6.15: EDS linescans in $La_{0.67}Ca_{0.33}Mn_{1.05}Cu_xO_3$, x=3,4,5. On the left the SEM micrograph shows, where the linescan was performed. On the right the EDS results are shown for La, Ca, Mn and Cu ratios.

6.5 Magnetic Characterization

The magnetization, M, of the samples was measured by the VSM technique (See Section 4.3). A series of experiments were set up to create a full temperature profile of the samples. At constant temperature, M is measured as a function of the applied magnetic field, H, from 0 to 1.6T. When the temperature profile was set up, small temperature steps (1-2 K) were used around the transition temperature where ($\frac{\partial M}{\partial T}$) is high, whereas away from the transition longer temperature steps (5 K) is adequate. In order to stabilize the temperature during isothermal measurements, the temperature was kept for 5 minutes within a 0.5 K confidence band, before the isothermal experiments were initiated. The temperature profile was set up to cover temperatures well above the Curie temperature as well as below to ensure that the phase transition region is covered i.e. that the samples are completely within the temperature range of the ferro- and paramagnetic states at the lowest and highest temperature, respectively. An example of the raw data from a full temperature profile is presented in Figure 6.16, where the magnetization data for $La_{0.67}Ca_{0.33}Mn_{1.05}O_3$ is presented. In Figure 6.16 the change of temperature intervals in the temperature profile is also indicated, i.e. where 5 K steps are used away from the transition while 2 K steps is used around the transition temperature. From the measured data, the magnetization versus temperature can be extracted (See Figure 6.17(a) and 6.17(b)). Both the transition temperature and magnetization are seen to decrease with increasing Cu content (See Figure 6.17(a)). The Curie transition, which experimentally can be defined as the inflection point ($\frac{\partial M}{\partial T}_{max}$) of the magnetization vs. temperature curve, can readily be extracted from these curves as well. The extracted transition temperatures are plotted in Figure 6.18. As is also indicated in Figure 6.17(b), the slope of the curves at the Curie transition ($\frac{\partial M}{\partial T}_{max}$) increases with increasing Cu doping towards 3% and then decreases above 3% Cu doping. This will be elaborated in the following section in relation to entropy change, which is proportional to $\frac{\partial M}{\partial T}$. From Figure 6.18 it is evident that the effect of Cu doping on the transition temperatures has a very large effect at low levels of doping. For the samples with 1,2 and 3% Cu the transition temperature decreases significantly from 267 K down to approximately 245 K. From 3 to 5 % the transition temperature remains almost constant. This could be understood by considering that the Cu could participate in two different effects. The saturation magnetization and the transition temperature decrease significantly from 0 to 3% Cu doping and then decrease only slightly above 3% Cu doping. In general a decrease in both the transition temperature and magnetization is expected, since the Cu ions are believed to replace the magnetic Mn ions based on previous studies described above. A dilution of the magnetic ions will therefore be expected to weaken the magnetic interactions. From the EDS measurements presented, the solubility of the Cu ions is suggested to be in the vicinity of 3%

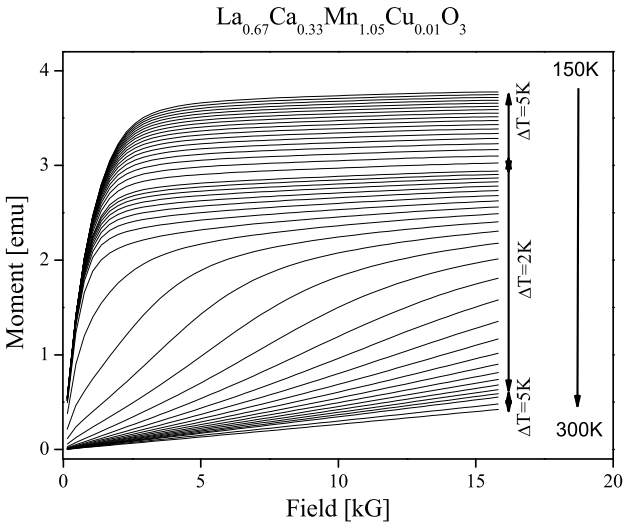

Figure 6.16: A set of isothermal magnetization curves from magnetization measurements on $La_{0.67}Ca_{0.33}Mn_{1.05}O_3$. In the right side of the figure, the temperature difference between isotherms is indicated with ΔT.

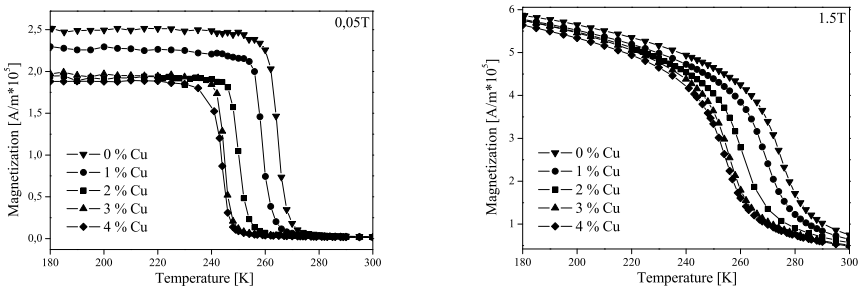

(a) (b)

Figure 6.17: Magnetization vs. temperature curves in an applied magnetic field of 0.05 T (a) and 1.5 T (b).

(This is only valid in these over-stoichiometric compositions). Above 3% the Cu ions started to agglomerate in the grain boundaries of some Mn-rich grains as observed above by EDS. These observations indicates that the Cu ions when dissolved in the structure, decreases the transition temperature and magnetiza-

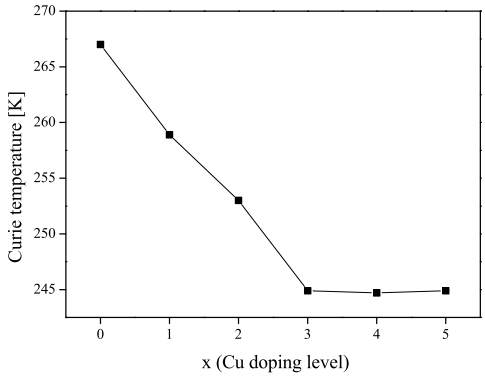

Figure 6.18: The transition temperature as function of x in $La_{0.67}Ca_{0.33}Mn_{1.05}Cu_xO_3$. The difference between the effect of Cu doping above and below 3% Cu doping was suggested from EDS measurements to stem from the maximum solubility of Cu in the over-stoichiometric perovskite structure.

tion. This is likely to have happened due to the diminished DE mechanism in environments where the magnetic Mn ions have been replaced by Cu ions. In the following section the Cu doping will be shown to have a positive effect at low doping levels, where the Cu actually enhances the MCE of the materials. The reason for the improved MCE is due to the increased slope $\frac{\partial M}{\partial T}$ through the phase transition temperature, which appears to be enhanced by small additions of Cu.

6.6 Magnetocaloric Properties

The MCE of the Cu doped samples have been characterized and compared using two different methods. The isothermal magnetic entropy change, ΔS_M have been calculated from the magnetization isotherms described in the previous section as well as from heat capacity measurements obtained on the DSC equipment developed in this work (See Chapter 5).

6.6.1 MCE from Magnetization Measurements

The simple formulae presented in Equation 4.4 is used to extract information on the MCE from a series of isothermal magnetization measurements (Figure 6.16). Figure 6.19 shows the calculated values of $\Delta S_M(T)$ for a field change of ΔH=1.5 T. This corresponds to a magnetic field possible to obtain in a magnetic refrigerator system with a permanent magnet. When the Cu content is gradually increased, $\Delta S_M(T)$ is kept nearly constant up to 3% Cu doping with a slight increase from 2 to 3% Cu. From 3 to 5% Cu, the MCE decreases significantly. Correlated with the results obtained in the EDS and the magnetization

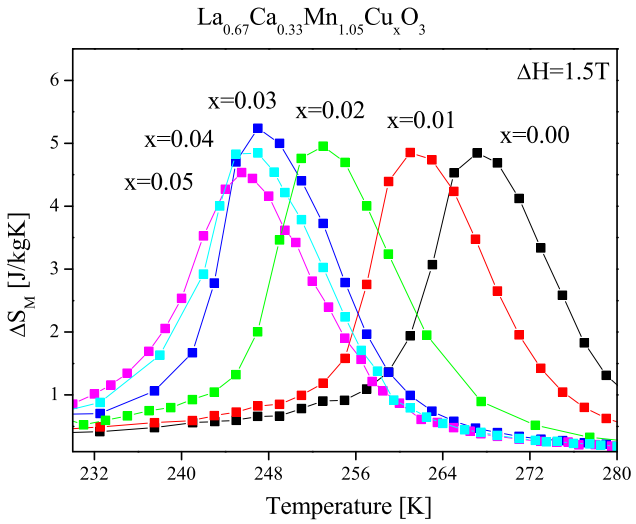

Figure 6.19: $\Delta S_M(T)$ for a field change of 1.5 T in $La_{0.67}Ca_{0.33}Mn_{1.05}Cu_xO_3$

measurements, it seems that two effects are in play during increasing Cu doping in the samples as suggested in the previous section. From 0 to 3% Cu, ΔS_M tends to increase or remain constant simultaneous to a decrease of the transi-

tion temperature. From 3 to 5% Cu ΔS_M starts to decrease and the transition temperature remains nearly constant with a slight change. In correlation with the EDS investigations on selected grains it seems that the increase in ΔS_M can be linked to the low doping levels, where the Cu ions are dissolved in the structure. From 3 to 5% Cu doping, it was found in the EDS measurements that the Cu ions appears to agglomerate in the grain boundaries. Simultaneously it is seen from magnetization measurements that the low temperature saturation magnetization decreased around $0.5*10^5$A/m from 0 to 2% Cu doping and only $0.15*10^5$A/m from 2 to 5% Cu doping in a 0.05 T field.

6.6.2 MCE obtained by Calorimetric Measurements

It is possible to characterize the magnetocaloric properties of a material from determination of the heat capacity as function of magnetic field [68]. In order to extract the heat capacity of the material a series of experiments are needed. The so-called 3-step-method (Equation 5.3) is used, which requires a set of 3 experiments for every magnetic field: (1) The calorimetric signal from the sample, $U_{sample}(T)$, (2) a reference material, $U_{ref}(T)$ and (3) the empty sample holder, $U_0(T)$. Figure 6.20 shows the raw calorimetric signals from such sets of experiments at 4 different magnetic fields, 0, 0.5, 1.0 and 1.5 T, for the $La_{0.67}Ca_{0.33}Mn_{1.05}Cu_{0.01}O_3$. Knowing also the mass of the sample and reference as well as the heat capacity of the reference, $C_{p,ref}(T)$, we can calculate the heat capacity of the sample, $C_{p,sample}(T)$, from Equation 5.3. Figure 6.21 shows the calculated heat capacity of $La_{0.67}Ca_{0.33}Mn_{1.05}Cu_{0.01}O_3$. Using the formula for calculating entropy from heat capacity measurements (Equation 2.24), the magnetic entropies of $La_{0.67}Ca_{0.33}Mn_{1.05}Cu_{0.01}O_3$ have been calculated (See Figure 6.22).
Finally the entropy changes can be calculated using Equation 2.25. Figure 6.23 shows $\Delta S_M(T)$ corresponding to a field change of 0.5, 1.0 and 1.5 T. The quality of the heat capacity data was insufficient to calculate the entropy changes. Even very small deviations in the heat capacity stemming from imperfections in the calibration will be blown up by the integration of heat capacity data done in the calculation of entropy. Since we would like to be able to compare the results from the calorimetric measurements of the MCE, it was decided to subtract a baseline artificially. To ensure this to have any physical relevance, the subtraction of all baselines was done according to the same procedure, which is described in Appendix A. The procedure takes basis in a set of assumptions, and the comparison of absolute values of the entropy changes obtained from magnetization measurements must be done with some reservation. However, since the baseline subtraction has been done in a consistent way (See Appendix A), we believe it is still possible to compare the entropy changes obtained for the different samples by calorimetric measurements.

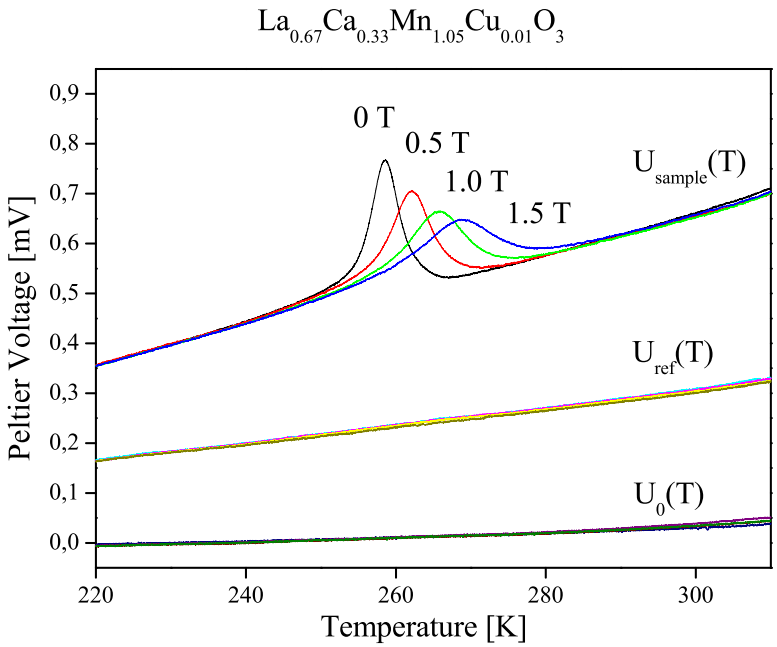

Figure 6.20: The raw calorimetric signals from the sample ($La_{0.67}Ca_{0.33}Mn_{1.05}Cu_{0.01}O_3$), $U_{sample}(T)$, a reference, $U_{ref}(T)$ and the empty sample holder, $U_0(T)$.

All the Cu doped samples have been treated in the same way as for the $La_{0.67}Ca_{0.33}Mn_{1.05}Cu_{0.01}O_3$ composition. Figure 6.24 shows ΔS_M for all six Cu doped samples measured for a field change of 0.5, 1.0 and 1.5 T. The calculations of ΔS_M for 3 different field changes reassures us that the procedure for extracting appears to be consistent. We observe for all samples the field dependency of both transition temperature and $\Delta S_{M,max}$, as was expected. The entropy changes have been compared in Figure 6.25 for all doping levels for the same field change. The results show the same tendency as observed from the entropy changes calculated from the magnetization isotherms. As the Cu doping is increased towards 3% Cu, ΔS_M increases towards a maximum. Above 3% Cu the ΔS_M decreases again. These findings confirm our observations from the magnetization results. The enhancement of the MCE at low Cu doping levels in the over-stoichiometric La-Ca-Mn-O system has been substantiated by calorimetric measurements. In Figure 6.26 the entropy changes of the six Cu doped samples have been compared. The black line with symbols represents the en-

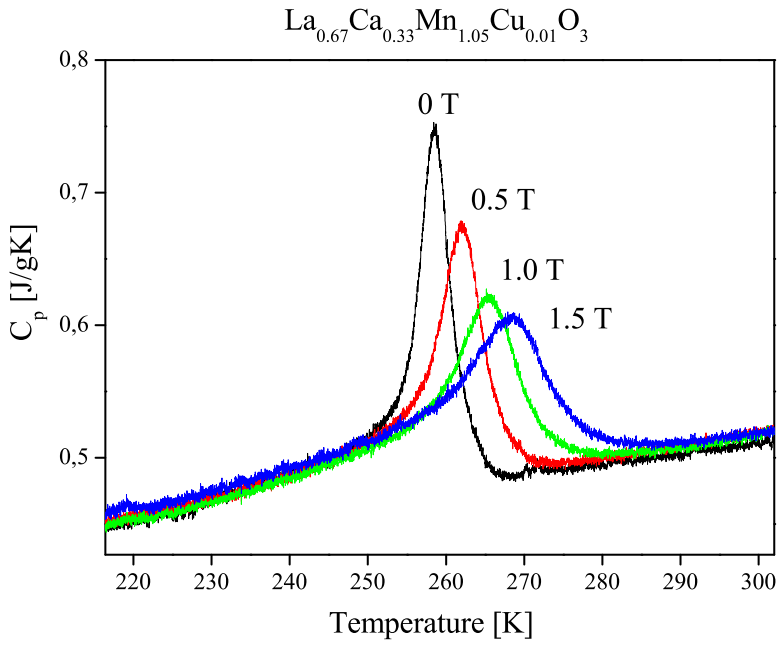

Figure 6.21: Heat capacity of $La_{0.67}Ca_{0.33}Mn_{1.05}Cu_{0.01}O_3$ as function magnetic field calculated from DSC measurements.

tropy changes calculated from magnetization data and the red line represents the entropy changes calculated from calorimetric measurements. The measurements are in fairly good agreement between the methods. The calorimetric measurements seem to underestimate the entropy changes in general. This might stem from the artificial baseline subtraction, where the entropy change is set to zero below and above the transition temperature. This assumption is only true far from the transition and would give rise to an underestimate. The differences in peak positions might stem from imperfect temperature calibration in either of the two techniques.

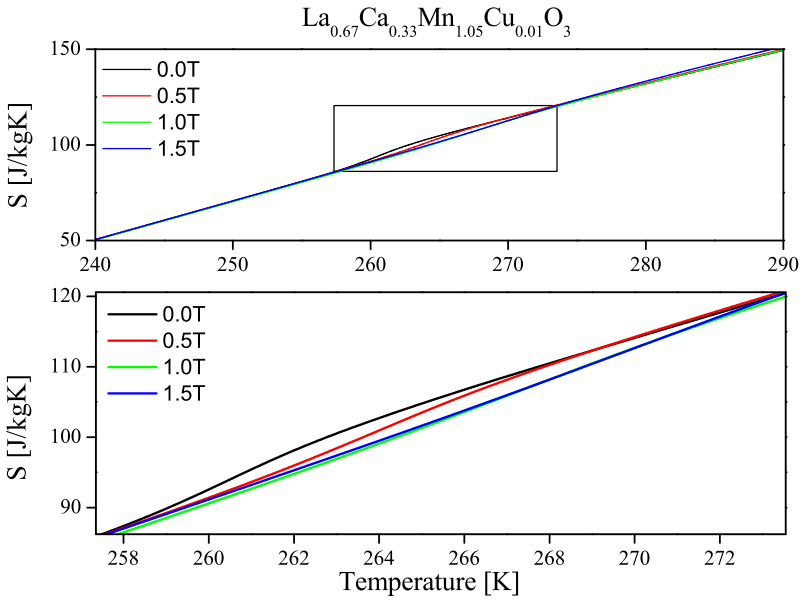

Figure 6.22: Entropy of $La_{0.67}Ca_{0.33}Mn_{1.05}Cu_{0.01}O_3$ calculated for magnetic fields of 0, 0.5, 1.0 and 1.5 T. The top panel shows the entropy calculated from 240-290 K and the bottom panel is a zoom on the phase transition region around 260-270 K.

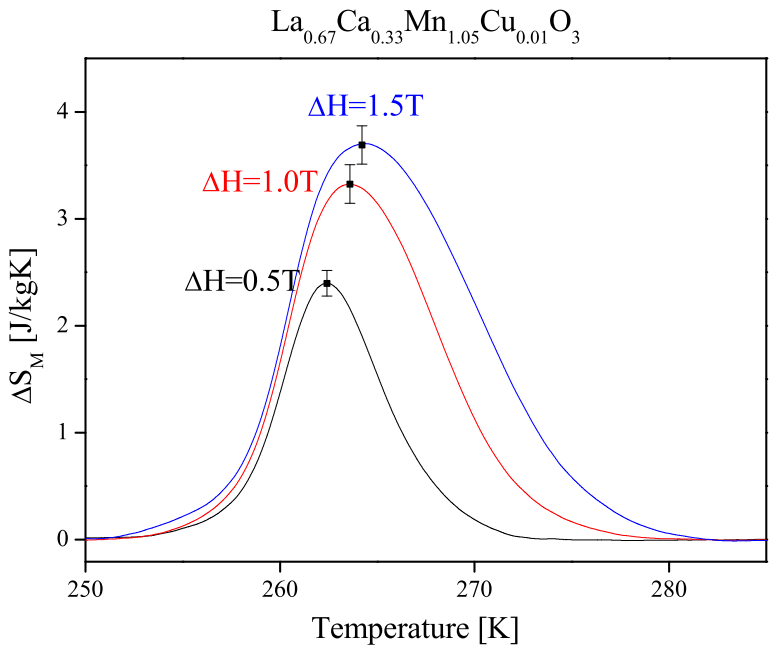

Figure 6.23: The MCE calculated as $\Delta S_M(T)$ from heat capacity measurements of $La_{0.67}Ca_{0.33}Mn_{1.05}Cu_{0.01}O_3$. $\Delta S_M(T)$ has been calculated for magnetic field changes of 0.5, 1.0 and 1.5 T.

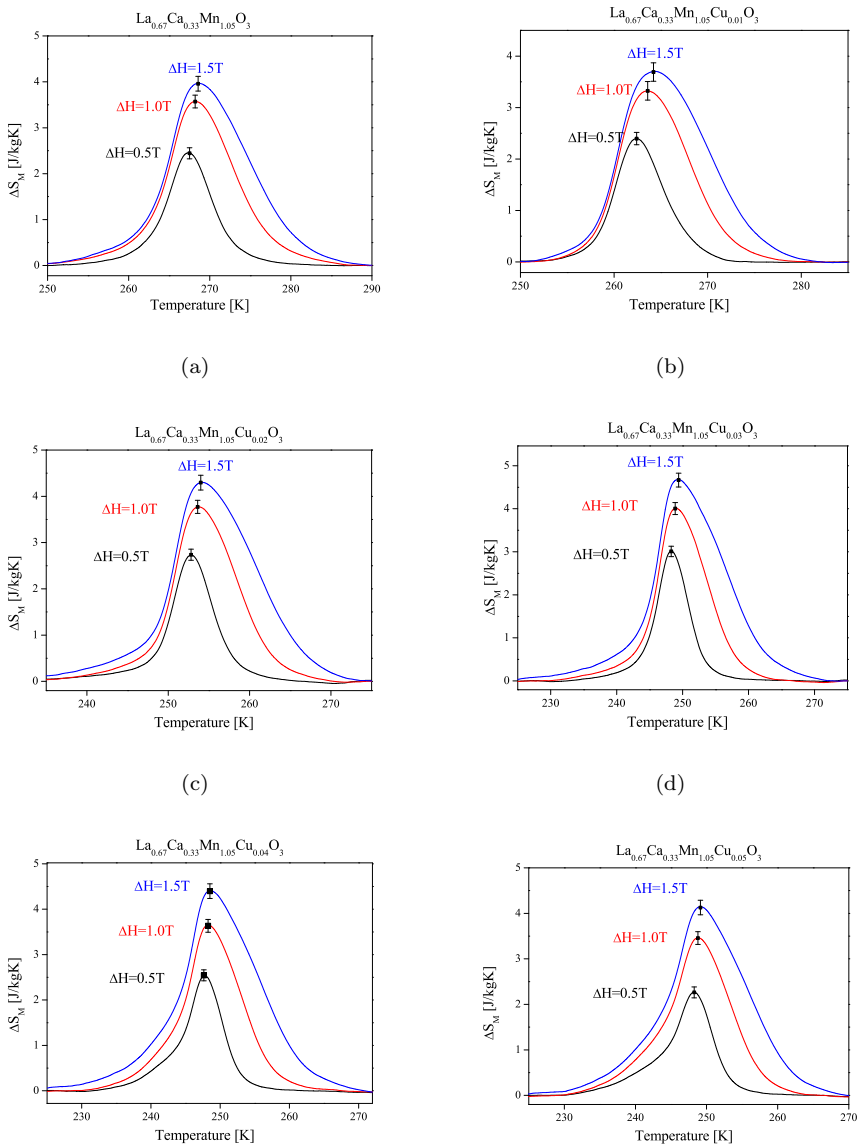

Figure 6.24: All entropy changes of $La_{0.67}Ca_{0.33}Mn_{1.05}Cu_xO_3$ determined by the procedure in Appendix A.

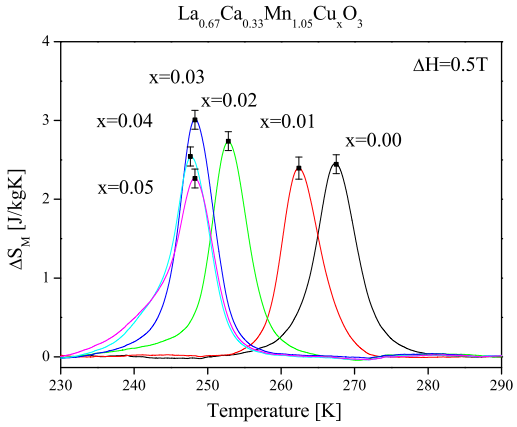

(a)

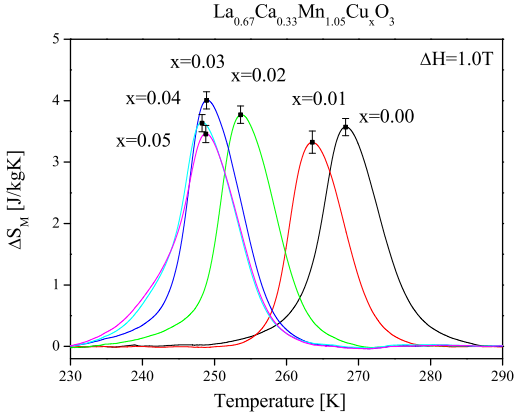

(b)

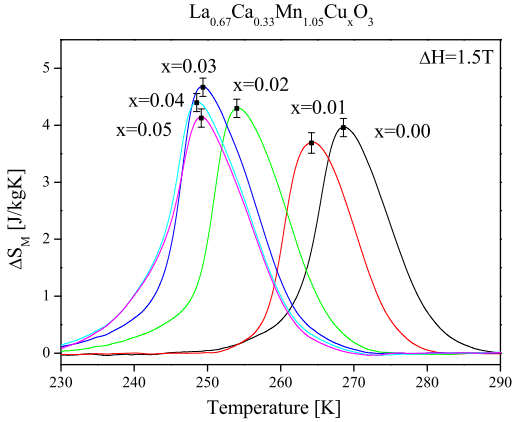

(c)

Figure 6.25: Entropy changes of $La_{0.67}Ca_{0.33}Mn_{1.05}Cu_xO_3$ determined by the procedure in Appendix A. (a) ΔH=0.5 T. (b) ΔH=1.0 T. (c) ΔH=1.5 T.

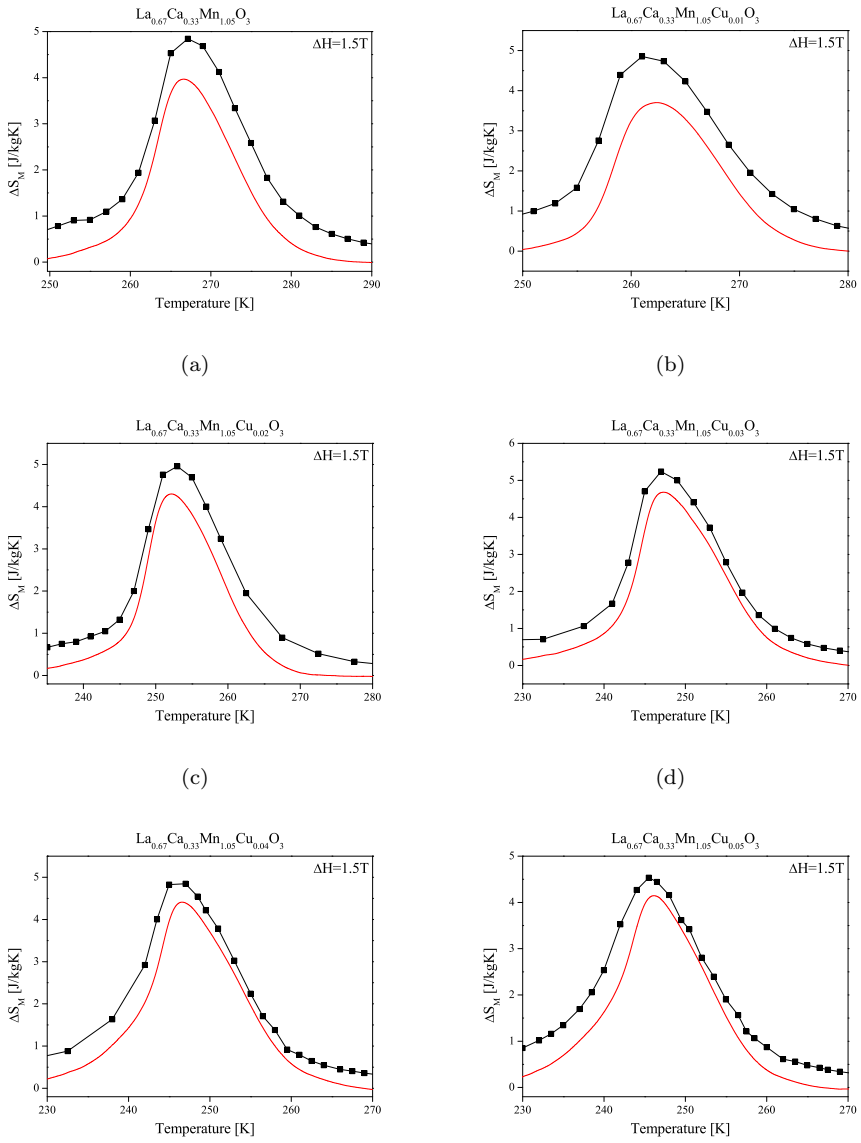

Figure 6.26: Comparison of entropy changes calculated from magnetization data (black line with symbols) and from DSC data (red line) of $La_{0.67}Ca_{0.33}Mn_{1.05}Cu_xO_3$ compositions.

6.7 Conclusion

From the structural refinement of the XRD patterns no visible phase change was found and all compositions are single phased in the orthorhombically distorted perovskite structure (Spacegroup Pbnm). It was found from the refinement that the unit cell volume decreased slightly with Cu doping together with a decrease of the Mn-O-Mn bond angle. As a consequence of the decreasing bond angle, the Curie temperature is lowered as was also observed by other studies [30]. The reason is the diminished orbital overlap in the Mn-O bond. The bond length also determines the overlap, but it was found from the refinements that this length is kept almost constant with Cu doping. From the SEM micrographs it was found that the porosity changes significantly with Cu doping. The sintering was greatly enhanced with Cu substitution, but since the over-stoichiometry of the samples was increased from 5 to 10% on the B-site when the Cu is increased from 0 to 5%, the improved sintering abilities could be a product of increased over-stoichiometry rather than specific to the Cu substitution. By EDS measurements some of the grains, which show contrast were investigated, and it was confirmed that above a level around 3% Cu doping, the Cu is agglomerating in or near the investigated grains, which from the EDS measurements were found to be Mn rich. It was proposed from the EDS linescans across these grains that the Cu was more likely to agglomerate in the grain boundaries.
From magnetization measurements some interesting effects were discovered. As the Cu content was increased from 0 to 3% the transition temperature was lowered by approximately 20 K, the saturation magnetization was also found to decrease significantly. Due to an improved quality (increased dM/dT_{max}) of the phase transition, the MCE in terms of the magnetic entropy change increases. The increase of the entropy change was confirmed by DSC measurements. Above 3% Cu the transition temperature is only lowered slightly around 2 K from 3 to 5% Cu doping, furthermore, the saturation magnetization was found only to decrease slightly.
Summing up the MCE can be increased by small additions of Cu, up to 3% in the over-stoichiometric mixed-valence manganites of composition $La_{0.67}Ca_{0.33}$-$Mn_{1.05}Cu_xO_3$. From structural investigations it was suggested that small amounts of Cu can be dissolved in the perovskite structure improving the quality of the transition, however, when larger amounts of Cu is added the Cu deteriorates the MCE.

CHAPTER 7

Magnetocaloric Refrigerator Materials

> The following chapter describes the work disclosed in US Patent Application US61/078886 and United Kingdom Patent Application No. 0815447.8 named "Magnetocaloric Refrigerators". Therefore, any portion of this chapter must not be disclosed to any third party without prior written permission from authorities at Risø DTU.

The invention relates to the production of a magnetocaloric refrigerator using lanthanum containing refrigerants. The lanthanum in the refrigerator material has been partly or completely substituted with lower purity raw materials rather than the typically used higher purity raw materials. The lower purity raw materials can be commercially available unfinished lanthanide concentrates from rare earth oxide natural resources. These concentrates are yet not separated into their individual components. Substitution of the low cost lanthanide concentrate for the pure lanthanum provides apart from the lowering of fabrication cost also increased MCE and tunability of the refrigerant working range. In order to obtain highly efficient magnetic refrigeration, it is crucial to use a magnetic material which exhibits a high MCE around the temperature of operation. This is possibly done in conjunction with other magnetocaloric materials exhibiting such an effect at selected adjacent temperatures. Therefore the tunability of the material is very important in the construction of an efficient refrigerator.
The MCE has been studied in several lanthanum containing materials. This work investigates the use of mixed-valence manganites with perovskite structure, which were described in Section 3. The effect of substituting other lanthanide elements for part of the lanthanum has been investigated earlier [87, 43, 88] in

lanthanum containing magnetic refrigerants. The materials for which data is presented in these studies contain, however, only lanthanum plus just one other lanthanide. The invention relates to the use of raw materials where at least 4 different lanthanides is present in the composition. We have now appreciated that satisfactory magnetocaloric refrigerant materials containing lanthanum can be produced using 'lanthanum concentrate', a commercially available mixed oxide containing lanthanum, cerium, praseodymium and neodymium as lanthanide components. This avoids the need to refine the original lanthanide bearing raw materials into separate pure lanthanides or reduces the necessary extent of the use of highly refined material where relative proportions of these lanthanides differing from those in lanthanide concentrate is desired. An alternative mixed lanthanide source that may be used in at least some instances is the lanthanum-rich mischmetal.

The lanthanide concentrates are obtainable from for instance Molycorp, Inc. Mountain Pass California[1] as the product entitled 'Code 5210 Lanthanum Concentrate' [89]. The other large source of rare earths in the world is the Baotou Ore in Baotou, Inner Mongolia, where La is like in the Mountain Pass ore refined from bastnaesite. It is an intermediate product produced during the purification of lanthanides from lanthanide ores and the exact composition of lanthanide concentrate may vary somewhat between suppliers. It generally contains La_2O_3, CeO_2, Pr_6O_{11} and Nd_2O_3 in weight proportions on an oxide basis normalized with respect to the lanthanum content 100% La_2O_3, 5-30% CeO_2, 5-20% Pr_6O_{11} and 20-40% Nd_2O_3 or more commonly 100% La_2O_3, 10-21% CeO_2, 12-14% Pr_6O_{11} and 28-34% Nd_2O_3. The use of lanthanum concentrate necessarily brings with it not only lanthanum, but also each of the three other named lanthanides and maybe even more residuals in small quantities. However, the elements do not have to be in the above proportions in the magnetocaloric refrigerant, as additional purified lanthanide oxides can be added in the manufacture of the product so as to increase the proportion of any of the four lanthanides or to provide one or more further lanthanide elements.

Preferably, the lanthanum content of the refrigerant derives from a mixture of lanthanum concentrate and a more pure source of lanthanum, but an alternative mixed lanthanide source for use in the invention is a mischmetal. These materials are also commercially available e.g. Tianjiao International Co. 'Code 9003 La Rich Mischmetal' [90]. La-rich mischmetal typically contain 61 wt% La, 2 wt% Ce, 35 wt% Pr, and 2 wt% Nd.

[1]The Mountain Pass ore provides around 90% of U.S. and 66.6% of the world output of the mineral bastnaesite, from which most lanthanides are extracted.

7.1 Synthesis

In order to investigate the possibility of using low purity lanthanide (Ln) mixtures instead, of the laboratory grade lanthanum, a set of samples were synthesized. Since we had no access to lanthanum concentrate from either of the above mentioned suppliers, the lanthanum concentrate was simulated by mixing laboratory grade lanthanides in a representative composition (Ln: $La_{65.5}Ce_{4.5}Pr_{7.5}Nd_{22.5}$). The lanthanide mix were substituted for lanthanum in four different compositions $(La_{1-x}Ln_x)_{0.67}Ca_{0.33}Mn_{1.05}O_3$ with x= 0, 0.33, 0.67 and 1. For the same reasons as explained previously in Chapter 6 the Mn content were kept 5% over-stoichiometric to ensure good sintering abilities. Explicitly the four compositions that constitute this study are:

1. $(La_{1.00}Ln_{0.00})_{0.67}Ca_{0.33}Mn_{1.05}O_3$
2. $(La_{0.67}Ln_{0.33})_{0.67}Ca_{0.33}Mn_{1.05}O_3$
3. $(La_{0.33}Ln_{0.67})_{0.67}Ca_{0.33}Mn_{1.05}O_3$
4. $(La_{0.00}Ln_{1.00})_{0.67}Ca_{0.33}Mn_{1.05}O_3$

All powders were synthesized using the glycine-nitrate combustion synthesis described in Section 4.1.1. The powders were calcined at 700°C and subsequently dry pressed and sintered at 1200°C according to the described procedure.

7.2 Structure

After synthesizing the samples they were characterized by XRD. The XRD patterns from the 4 samples are shown in Figure 7.1. All samples are well-crystallized and may be indexed into the orthorhombically distorted perovskite structure with spacegroup Pbnm according to the same reflections as in Figures 6.5 and 6.6. By Rietveld refinement the XRD patterns were investigated in detail (See Table 7.1). As the doping increases the unit cell volume decreases as would be expected since all the substituted ions are smaller than the La^{3+} ion. The valency of Nd and Pr are known from previous studies [91] to be Nd^{3+} and Pr^{3+}, where Ce is known to exist in a mixed valency state Ce^{3+}/Ce^{4+} [92]. The ionic sizes of these valency states have been listed for coordination number 9 in Table 7.2. The average ionic size on the A-site $\langle r_A \rangle$ decreases with increasing doping level. Furthermore, the bond angle Mn-O-Mn is decreasing. This leads us to believe that the transition temperature will decrease, as it was discussed in Chapter 6. It has already been established in previous studies [93, 88] that substitution of Nd for La leads to a lowering of the Curie temperature. Equally studies on Ce substitution also showed a lowering of the Curie temperature [94] (See Figure 7.2). It is therefore expected that the substitution of our lanthanide

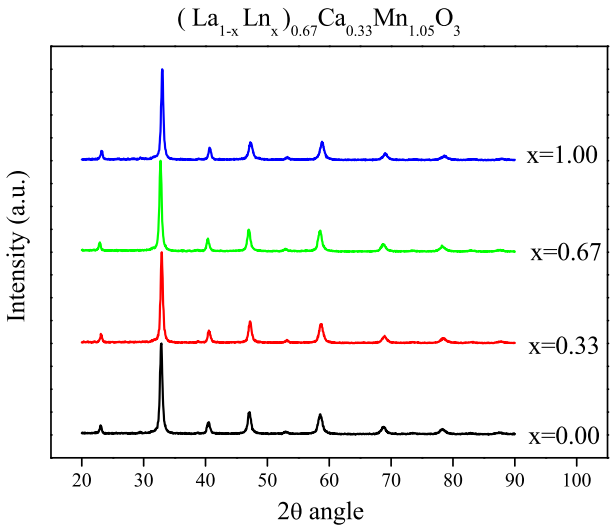

Figure 7.1: XRD patterns of the sintered samples. The XRD patterns show that all powders are well-crystallized and single phased in the perovskite structure.

mix leads to a lowering of the Curie transition, which will be investigated in the following section.

7.3 Magnetism

The four compositions were characterized magnetically by the VSM technique (See Section 4.3). A temperature profile was made for each sample. At constant temperature M is measured as a function of the applied magnetic field, H. From the isothermal magnetization measurements, magnetization versus temperature can be extracted (See Figure 7.3). The magnetization data confirms the ferromagnetic nature of the samples even at the highest doping level. The transition temperature is lowered with increased doping level. As it was pointed out in the beginning of this chapter the tunability of the transition with doping level is a very advantageous property of magnetic refrigerants. The magnetization versus temperature curves in Figure 7.3 clearly demonstrate that the transition temperature varies continuously with doping level. The fact that the change in transition temperature is continuous makes tuning of the transition very easy. To demonstrate the continuity, the transition temperature has been plotted against doping level in Figure 7.4.

$(La_{1-x}Ln_x)_{0.67}Ca_{0.33}Mn_{1.05}O_3$				
x	0	0.33	0.67	1.00
Phase				
Spacegroup	Pbnm	Pbnm	Pbnm	Pbnm
Unit Cell				
a [nm]	0.5456	0.5432	0.5439	0.5453
b [nm]	0.5475	0.5468	0.5472	0.5452
c [nm]	0.7722	0.7724	0.7695	0.7672
V [nm^3]	0.2307	0.2294	0.2290	0.2281
Bond angles				
Mn-O1-Mn	175	167	158	149
Goodness-of-fit				
χ^2	2.24	2.14	2.07	2.15

Table 7.1: Refined structural parameters of the $(La_{1-x}Ln_x)_{0.67}Ca_{0.33}Mn_{1.05}O_3$ samples with four different Ln doping levels x. All structures are refined using the orthorhombic Pbnm spacegroup. The refined parameters are the unit cell dimensions (a, b, c), unit cell volume (V), the bond angles for the Mn-O-Mn bonds and finally the χ^2 value representing goodness-of-fit.

La^{3+}	Nd^{3+}	Pr^{3+}	Ce^{3+}	Ce^{4+}
0.1216	0.1163	0.1179	0.1196	0.1070

Table 7.2: Ionic radii of A-site ions given in nm. From Shannon [31].

The data points in Figure 7.4 have been fitted with a second order polynomial to demonstrate the continuity. Such correspondence between doping level and transition temperature could also be used in the design of a refrigerator to calculate the ratio of lanthanides that needs to be used to obtain a certain temperature working range of the refrigerant. It should be noted, that the higher doping level (x→1.00), the cheaper the material gets, since it is the cheaper raw material that is substituted into the composition. However, as it will become clear in the following section, the cost-effectiveness is not the only advantage.

7.4 Magnetocaloric Properties

The MCE in terms of ΔS_M in the Ln doped materials have been characterized by isothermal magnetization measurements. Since two out of the three doped samples have a transition temperature outside the working range of the DSC described in Chapter 5, the MCE was not investigated with calorimetric

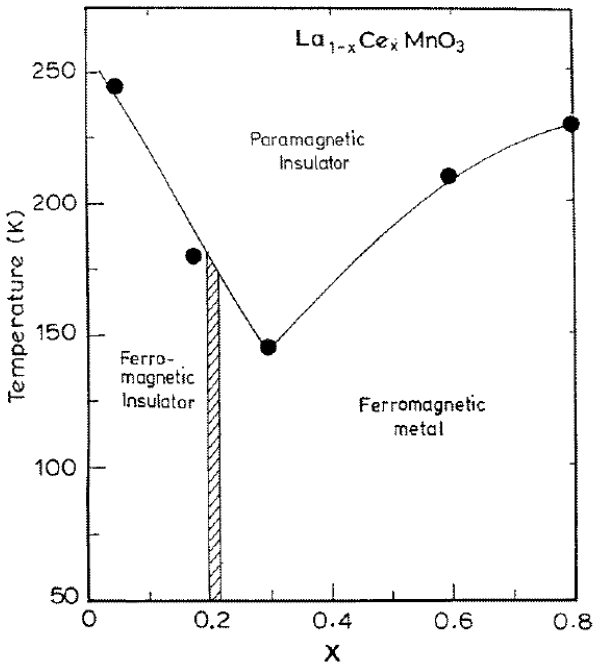

Figure 7.2: Ce substitution in the $LaMnO_3$ system investigated by Philip and Kutty [94].

measurements for these compositions. The MCE calculated from magnetization data are shown in Figure 7.5. We learned from the magnetization versus temperature plots, how the doping level was affecting the transition temperature (See Figure 7.4), but from the calculation of the MCE it is evident that the substitution is not only decreasing the cost of the material, but it is actually increasing the MCE. Figure 7.6 shows the maximum entropy changes as function of doping level. The maximum increases to an optimum at the x=0.67 composition where the magnetic entropy change reaches 6.33 J/kgK for a field change of 1.5 T. This is an increase from the undoped sample (x=0.00) of more than 20%, which had a maximum of 5.26 J/kgK for the same field change. Even more important in terms of application in refrigerators might be the fact that the integrated area under the ΔS_M curves increases with doping. A value often used to describe the potential of magnetocaloric materials is the relative cooling power (RCP), which is defined by:

$$RCP = \Delta S_{M,max} \times \delta_{\mathrm{FWHM}} \tag{7.1}$$

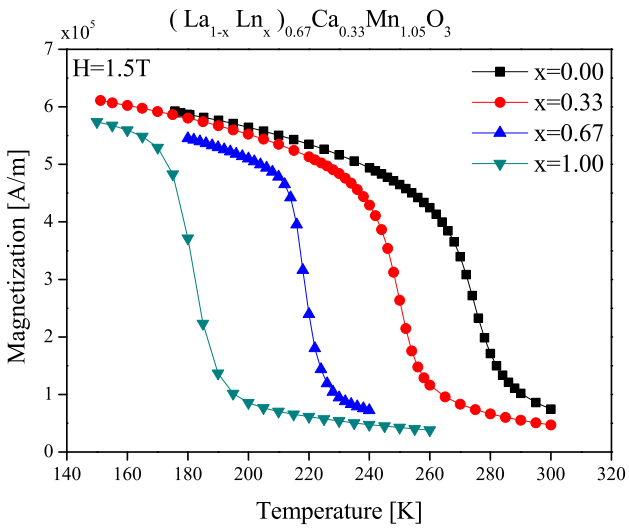

Figure 7.3: Magnetization curves as function of temperature in the $(La_{1-x}Ln_x)_{0.67}Ca_{0.33}Mn_{1.05}O_3$ compositions.

where $\Delta S_{M,max}$ is the maximum value and δ_{FWHM} is the full width at half maximum (FWHM) of the peak in entropy change. Each material in a refrigerator has to perform well in a range of temperatures, since there is a temperature gradient in the system from the hot to the cold end. This can be circumvented in some designs with a cascade of materials having different transition temperatures. Therefore the more narrow the ΔS_M peak of a material is, the smaller working range it has and the more different compositions are needed to span the working range of the refrigerator. For these reasons a good refrigerant can also be a material with a decent $\Delta S_{M,max}$ and a high RCP. The RCP's are plotted in Figure 7.7 and it becomes clear that the RCP increases continuously as function of doping level, which indicates that the doped materials could perform well in a magnetic refrigerator.

7.5 Conclusion

A patent application were filled claiming the use of lanthanum containing magnetic refrigerants, where the lanthanum has been replaced by raw materials of lower purity, where La, Ce, Pr and Nd are present in a lanthanide mix. The substitution of lanthanum leads to a decrease in the transition tempera-

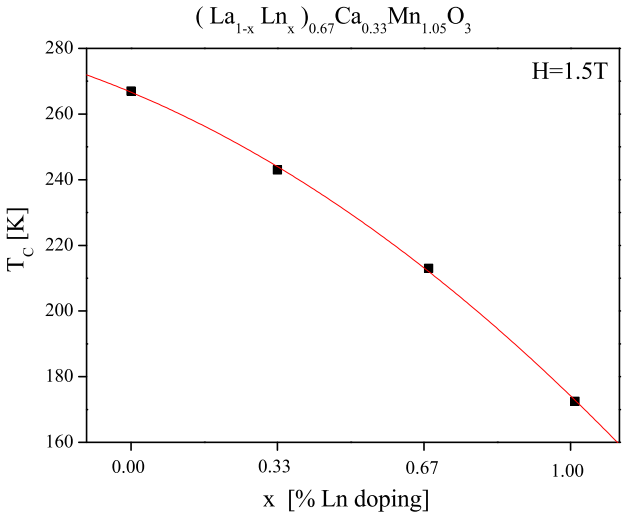

Figure 7.4: The transition temperature as function of Ln doping level x in $(La_{1-x}Ln_x)_{0.67}Ca_{0.33}Mn_{1.05}O_3$. A second order polynomial are fitted to the data points as a guide to the eye (red line).

ture from 267 K to around 175 K in the undoped (x=0.00) and fully doped (x=1.00) sample. Apart from the ability to tune the magnetocaloric material in this temperature interval, it was also demonstrated that the maximum MCE was increased by more than 20% at x=0.67 doping level and that the RCP is continuously increasing with doping level.

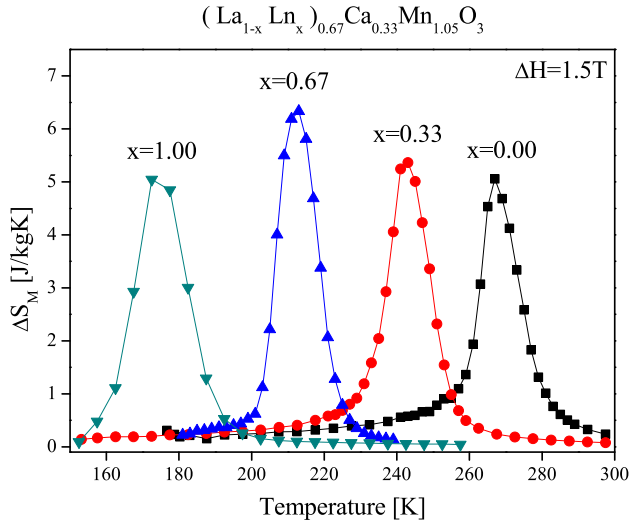

Figure 7.5: ΔS_M(T) curves of $(La_{1-x}Ln_x)_{0.67}Ca_{0.33}Mn_{1.05}O_3$. The entropy changes are obtained with a magnetic field change of 1.5 T.

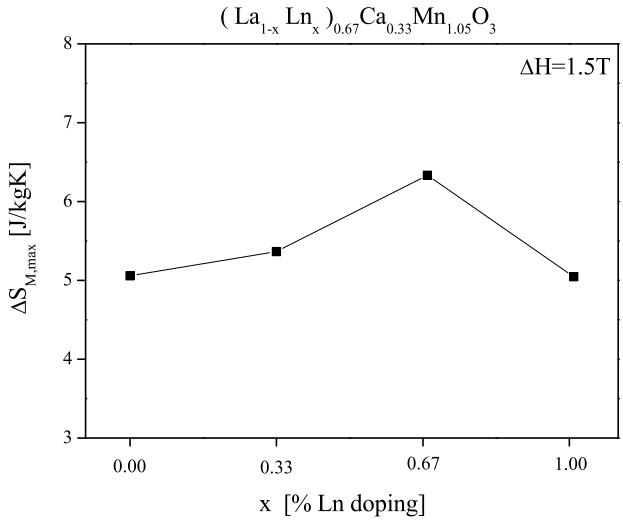

Figure 7.6: $\Delta S_{M,max}$ are extracted from Figure 7.5 and plotted as function of doping level x in $(La_{1-x}Ln_x)_{0.67}Ca_{0.33}Mn_{1.05}O_3$. The entropy changes correspond to a field change of 1.5 T

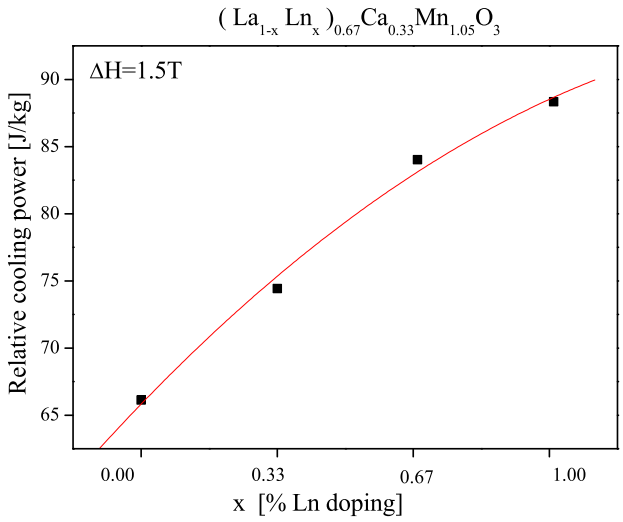

Figure 7.7: The relative cooling power (RCP) as function of Ln doping level x in $(La_{1-x}Ln_x)_{0.67}Ca_{0.33}Mn_{1.05}O_3$. A second order polynomial are fitted to the data points as a guide to the eye (red line)

CHAPTER 8

Conclusions and Outlook

This Ph.D. work has been devoted to the preparation and characterization of magnetocaloric materials. A differential scanning calorimeter (DSC) has been developed for this purpose and two materials systems from the family of mixed-valence manganites have been investigated. In this section the relevant results and conclusions from this research will be summarized. Finally some suggestions for further work will be described in the Outlook section.

8.1 Conclusions

- A novel DSC was constructed for the purpose of characterizing magnetocaloric materials in the near room temperature range (200-340 K). The key enhancements compared to conventional zero magnetic field DSC is a significant improvement of the signal-to-noise ratio and the option of applied magnetic field. Test results on pure Ga showed excellent agreement with the literature. The DSC represents a cheap versatile instrument compared to commercially available instruments, which can easily be fit into other magnets or altered to other temperature ranges. The DSC has been optimized for working in the room temperature range. Since the DSC is able to operate in the magnetic field of a conventional laboratory magnet, the use of expensive He-cooled superconducting magnets can furthermore be avoided.

- Cu doping in $La_{0.67}Ca_{0.33}Mn_{1.05}Cu_xO_3$ was investigated for doping levels up to 5% Cu. Several interesting findings were derived from these

studies. As the most important results with regards to magnetocaloric properties was the enhancement of the magnetic entropy change with an optimum at 3% Cu doping. These results were confirmed by magnetization measurements as well as calorimetric measurements. There was no direct indication from the structural refinement, which could explain the effect. However, by studying the morphology of the samples a number of effects were seen to coincide with the changes in magnetocaloric properties. From EDS measurements, it was suggested that the solubility of the Cu ions in the over-stoichiometric composition was around 3%. EDS linescans showed that with doping levels of 3% and above, Cu started to agglomerate in the grain boundaries of some Mn-rich grains distributed in the sample. The size of these grains increased with increasing Cu addition, and the Cu content increased significantly compared to Mn near the grain boundaries. The porosity was estimated by image analysis and showed an almost constant pore size at doping levels up to 2% followed by an increase in pore diameter from 1 to 4 μm at 5% Cu doping. Since the magnetization measurements showed a decrease in both transition temperature and saturation magnetization indicating a weakening of the magnetic interactions, the increased MCE resides in the improvement of the quality of the magnetic transition. Above 3% (with this stoichiometry of the sample) the agglomerating Cu ions starts to deteriorate the MCE.
This means that Cu ions can be used in very small amounts to tune the transition temperature, which is good for applications, and furthermore actually increase the MCE when doing so. The ability to tune a magnetocaloric material without deteriorating the MCE is a very desired characteristic for the potential as magnetic refrigerator material.

- The second material system investigated in this Ph.D. work took as the first system also basis in the $La_{0.67}Ca_{0.33}Mn_{1.05}O_3$ system. The effect of substituting pure La as raw material with an impure lanthanide mix (lanthanum concentrate) consisting of La, Ce, Pr and Nd. The incentive to pursue this rather complex system is the potential of making very cheap magnetocaloric refrigerator materials. In the basic composition La is the most expensive part and the cost of producing these manganites can be greatly reduced by using lanthanide constituents of lower purity. If this substitution could be done without significant deterioration of the MCE these materials could greatly enhance their potential for magnetic refrigeration in case of an upscaled production of magnetic refrigerators in the future.
  Investigation of the compositions was done by mixing pure lanthanide elements in a ratio that resembled those of lanthanum concentrates. The compositions varied from zero substitution to complete substitution of

the La with the lanthanide mix Ln i.e. $(La_{1-x}Ln_x)_{0.67}Ca_{0.33}Mn_{1.05}O_3$ x=0, 0.33, 0.67 and 1. In all compositions the material crystallized in the perovskite structure and was single phased. Further investigations showed that the substitution of Ln tuned the transition temperature continuously down from 267 K to 175 K in the undoped (x=0) to the fully doped (x=1) sample, respectively. This indicated that the materials can be tuned within 100 K to have exactly the desired transition temperature without any difficulties to ensure the maximum MCE at the working temperature of the refrigerator.
The MCE of the samples was investigated and it was demonstrated that the substitution of Ln actually enhanced the MCE. In terms of $\Delta S_{M,max}$ the compositions showed a maximum effect for the x=0.67 composition. $\Delta S_{M,max}$ is the most commonly used parameter to quantify the MCE, but the relative cooling power (RCP) is a parameter that takes into account that the material needs to work in a certain temperature interval to be attractive in applications. Calculations of RCP with Ln substitution showed that RCP increased with doping level up to x=1. The Ln substitution could then, not only facilitate a cost reduction and a way to tune the transition temperature, but also increase the relative cooling power of the material. These findings seemed promising and were disclosed in a US and UK patent application, which is currently pending.

8.2 Outlook

The magnetic refrigeration seems in general to have great potential for future refrigeration technologies, but many different aspects of the technology must be improved before an actual commercialization.
However, with regards to this particular work some quite specific efforts could be pointed out to follow up on this work. This work endeavored the development of a new characterization technique, but lots of more work could be done with the actual purpose i.e. the development and understanding of new magnetocaloric materials. Furthermore, there are still some issues regarding the calibration. The DSC works very well with a very high sensitivity of the calorimetric signal. However, to be able to extract the entropy changes some work is still required on the calibration of the DSC. One problem is, that even very small changes in the base level or the background signal blows up in the integration, when calculating the entropies. At the moment this necessitates an artificial baseline subtraction, which can hopefully be avoided by minimizing experimental errors and re-calibrating the setup. Samples can still be compared to each other, but it is very hard to determine the actual error on the absolute values found from these calculations.

An interesting aspect of both the investigated materials systems could be the design of materials, where either Cu doping or Ln doping was applied to magnetocaloric materials with initial transition temperatures above room temperature to see if the same advantages could be obtained simultaneously to a decrease in transition temperature across the room temperature.

APPENDIX A

Baseline subtraction of MCE data

Due to the data quality it was necessary to perform an artificial background subtraction to be able to compare the data on entropy changes calculated from DSC measurements. We had been unable so far to calibrate the DSC system completely. This induced a large background in the calculated entropy data, since small deviations in the heat capacity data, lead to large deviations when integrated over the investigated temperature interval necessary to get information on the entropy changes. In Figure A.1(a) the heat capacity is shown for the $La_{0.67}Ca_{0.33}Mn_{1.05}O_3$ composition determined by the 3-step-method (See Equation 5.3). The heat capacity data are in very good agreement with heat capacities determined by alternative techniques (See Chapter 5). However, as it is demonstrated in Figure A.1(a) in the bottom panel, which is a zoom of the data in the top panel, the heat capacity does not vary continuously with magnetic field. The highest C_P values belong to the zero field measurement (black line), the lowest to 0.5 T (red line) and the two data sets in the middle belong to the measurements with applied fields of 1.0 T and 1.5 T (green and blue lines, respectively). Since we cannot resolve a systematic difference in heat capacity as function of magnetic field we cannot estimate the difference of the contribution to the entropy from 0 K to the starting temperature of the experiment. When a difference in heat capacity cannot be determined, the best approximation is to assume that the contribution $C(T_1)_H$ in Equation 2.24 is set to be constant for different magnetic fields. This term then vanishes in the calculation of the entropy change (See Equation 2.25). This means that the entropy change will be fixed to zero in the limit of low temperature. When the calculation of the entropy change is performed according to Equation 2.25 without the constant

term $C(T_1)_H$, it becomes clear that $C(T_1)_H$ is not the only problem in the calculation. Figure A.1(b) shows the entropy changes of $La_{0.67}Ca_{0.33}Mn_{1.05}O_3$ calculated for 3 different field changes. As it is quite obvious from the figure, a substantial background in the entropy data makes comparison of the entropy changes impossible. However, since we know from our heat capacity data that the heat capacity may be approximated as constant in the low temperature and high temperature limits (See top panel Figure A.1(a)), it can roughly be assumed that the entropy change can be set to zero both in the high and low temperature limits ($\Delta S=0$). Making all these assumptions we have to be aware that the absolute values of the entropy changes could vary significantly from the actual values. However, the peak positions will not vary substantially by this procedure, and we will propose that by the explained procedure, we can also compare the values from sample to sample.

The assumption is that the entropy change is zero in the high and low temperature limit. Figure A.1(c) shows the entropy change corresponding to a field change of 0.5 T in $La_{0.67}Ca_{0.33}Mn_{1.05}O_3$. To meet the assumption that the entropy change is zero in the high and low temperature limit a base line is constructed from an interpolated line between ten equidistant handpicked points. The simulated baseline is constructed to be as continuous as possible, but since the pick of the baseline is somewhat discretionary, we want to estimate the magnitude of the error, this could impose on the final values of entropy changes. For this purpose three different baselines are constructed, that all meet the high and low temperature limit of $\Delta S=0$. Three baselines are shown in Figure A.1(c) as an example. In the middle the "best guess" is indicated by the green line. The best guess represents a baseline constructed to be as continuous as possible, since we don't have reason to expect any discontinuities neither from the measurements nor from the calculation. However since this a completely artificial baseline, we have constructed two "worst guess" baselines (indicated by the red lines), that either over- or underestimate the entropy change. This has been done to be able to evaluate the maximum error this procedure would impose on the calculation. In Figure A.1(d) the "best guess" of the base lines have been subtracted and the error bars indicate the maximum error that were limited by the two "worst guess" baselines. Figure A.1(e) shows the 3 entropy change curves from Figure A.1(b) with subtracted base lines and error bars, and its now possible to compare the different curves. This procedure has been used to derive information on the all the entropy changes calculated from DSC measurements presented in this work. It is of course with reservation that these results can be used as a quantitative analysis, but the entropy changes calculated from DSC measurements substantiates the trends found by other characterization techniques and these results were therefore decided to be included despite the many assumptions.

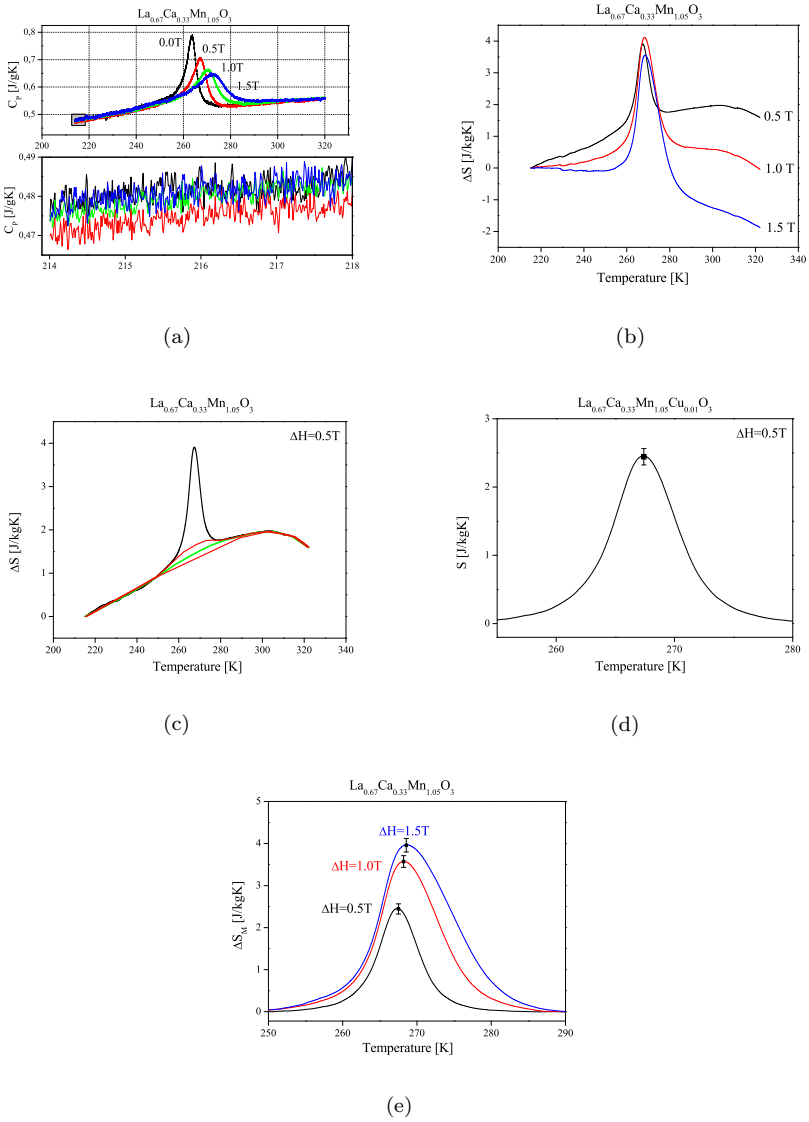

Figure A.1: Five graphs that describes the procedure used to extract information on entropy changes from DSC measurements. (a) C_P curves. (b) Three calculated entropy curves that demonstrate the problem with comparison between experiments. (c) Constructed baselines. Green line shows the "best guess" baseline and red lines show the "worst guess" baselines. (d) The entropy change curve from ((c)) with subtracted baseline and error bars. (e) The three curves from ((b)) made comparable by baseline subtraction by the described procedure.

APPENDIX B

Paper published in Review of Scientific Instruments.

Paper I

Indirect measurement of the magnetocaloric effect using a novel differential scanning calorimeter with magnetic field.
Jeppesen, S., Linderoth, S., Pryds, N., Theil Kuhn, L., and Jensen, J.B.
Review of Scientific Instruments **79** 2008, 083901.

Indirect measurement of the magnetocaloric effect using a novel differential scanning calorimeter with magnetic field

S. Jeppesen,[a] S. Linderoth, N. Pryds, L. Theil Kuhn, and J. Buch Jensen
Fuel Cells and Solid State Chemistry Department, Risø DTU, Technical University of Denmark, DK-4000 Roskilde, Denmark

(Received 10 April 2008; accepted 20 June 2008; published online 5 August 2008)

A simple and high-sensitivity differential scanning calorimeter (DSC) unit operating under magnetic field has been built for indirect determination of the magnetocaloric effect. The principle of the measuring unit in the calorimeter is based on Peltier elements as heat flow sensors. The high sensitivity of the apparatus combined with a suitable calibration procedure allows very fast and accurate heat capacity measurements under magnetic field to be made. The device was validated from heat capacity measurements for the typical DSC reference material gallium (Ga) and a $La_{0.67}Ca_{0.33}MnO_3$ manganite system and the results were highly consistent with previous reported data for these materials. The DSC has a working range from 200 to 340 K and has been tested in magnetic fields reaching 1.8 T. The signal-to-noise ratio is in the range of 10^2–10^3 for the described experiments. Finally the results have been compared to results from a Quantum Design® physical properties measuring system. The configuration of the system also has the advantage of being able to operate with other types of magnets, e.g., permanent magnets or superconducting coils, as well as the ability to be expanded to a wider temperature range. © *2008 American Institute of Physics.* [DOI: 10.1063/1.2957611]

I. INTRODUCTION

The heat capacity of a material as a function of temperature is important for the determination of the thermodynamic properties of a material. The use of calorimetry to investigate the magnetocaloric effect (MCE) is an important tool in the development and testing of new materials, e.g., magnetic refrigeration. Magnetic refrigeration is an emerging technology that has the potential for high energy efficiency.[1,2] Recent research and development of magnetic refrigerants have demonstrated large magnetocaloric effects in the vicinity of room temperature in several materials[3,4] and the need for fast and reliable characterization techniques of the MCE is increasing. As pointed out by Pecharsky and Gschneidner,[5] calorimetry provides a method to minimize the systematic errors in the determination of the isothermal magnetic entropy change from heat capacity data as a complement to magnetization data.

Experimentally, the heat capacity is measured by calorimetry. Although a variety of commercially available instruments are used for this purpose, the ability to conduct thermal measurements as a function of applied magnetic field is still quite rare.[6–9] Apart from the obvious advantage of minimizing systematic errors by using heat capacity measurements, the calorimetric approach also provides a fast way to obtain information on magnetocaloric effects as well as structural changes and charge ordering.[10]

Different methods to determine the MCE have been suggested in literature.[5,7,11]

(1) *Direct measurement*. Measurements of the adiabatic temperature change, ΔT_{ad}, by moving the sample in and out of a magnetic field region and recording the changes in the temperature.
(2) *Indirect measurement*. Magnetization method: by determining the magnetization curves at various temperatures, the magnetic contribution to the entropy change, ΔS_M, can be extracted.
(3) *Indirect measurement*. Calorimetric method: by measuring specific heat capacity as a function of temperature at various magnetic field strengths.

The second method is the most commonly used, while methods 1 and 3 require specialized equipment.

Clearly, the determination of the thermodynamic properties of materials, which exhibit a MCE, requires a reliable and accurate determination of the heat capacity of a sample under magnetized conditions. By knowing the heat capacity, C, as a function of temperature, T, and as a function of applied magnetic field, H, it is possible to calculate the isothermal magnetic entropy change ΔS_M:

$$\Delta S_M(T) = S(T)_{H_F} - S(T)_{H_I}, \tag{1}$$

$$S(T)_{H_{I,F}} = \int_0^T \frac{C(T)_{H_{I,F}}}{T} dT + S_{0,H_{I,F}}, \tag{2}$$

where the subscripts I and F denote initial and final states. S_0 is the zero temperature entropy normally assumed to be zero.[1]

In this paper, we present a simple and very accurate differential scanning calorimeter (DSC) for the determination of the specific heat of samples under magnetic field.

[a]Author to whom correspondence should be addressed. Tel.: +45 4677 5774. FAX: +45 4677 5858. Electronic mail: stinus.jeppesen@risoe.dk.

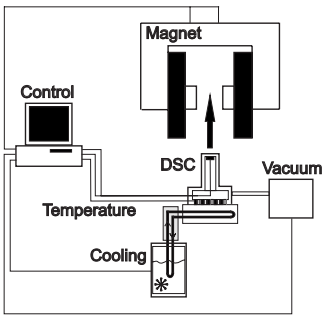

FIG. 1. Schematic illustration of the DSC setup. In this setup the temperature of the sample (heating and cooling) is controlled by a Peltier element with an additional separate cooling unit. The DSC can be operated with and without magnetic field. The running parameters of the DSC are controlled from a computer. In order to ensure a complete isolation of the sample from the surroundings, the sample is also kept in vacuum using a turbopump system which is coupled to the DSC unit.

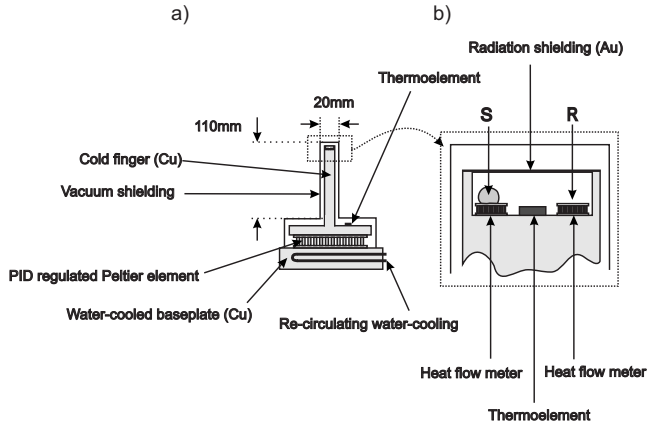

FIG. 2. Schematic of the measuring unit. (a) The complete DSC unit and (b) a close-up of the sample holder. (a) The temperature is controlled by a water-cooled baseplate mounted with a Peltier element. The Peltier element is PID controlling the temperature of the cold finger by a LABVIEW® interface. The thermoelement for the PID control is placed distant to the measuring unit to level out temperature fluctuations caused by the PID control, and the sample temperature is then logged close by the sample (s) and reference (r) by another thermoelement. The two small Peltier elements marked as sample (s) and reference (r) are independently used as heat flow sensors for measuring of the sample and the reference to provide a differential signal.

II. EXPERIMENTAL DETAILS

A. Construction of the calorimeter

When designing the calorimeter, a large effort was devoted to optimization according to these criteria:

(1) accurate heat capacity measurements under magnetic field,
(2) determination of the MCE must be optimized around room temperature, and
(3) the measurement should be performed in near-adiabatic conditions.

A description of the calorimeter is schematically depicted in Fig. 1. The calorimetric block is a solid copper cylinder of high thermal conductivity. This configuration allows for the use of any standard laboratory electromagnet, a superconducting coil magnet, or, alternatively, a permanent magnet. The temperature is measured to within ± 0.1 K by means of a platinum resistance thermometer placed in the DSC cavity. The Peltier element acts like 16 thermocouples placed thermally in parallel and electrically in series, which puts the calorimeter into the family of Calvet calorimeters.[12] This idea to use Peltier elements as heat flow sensors was proposed by Plackowski *et al.*[7] and has the advantage of obtaining highly reproducible data with high sensitivity in a very inexpensive manner. As opposed to Plackowski *et al.* and other types of insets to superconducting magnets[6–9] this setup was designed to be more flexible in the adaption into the applied magnetic field. By keeping the measuring unit as small as 20 mm in diameter and the cold finger reaching 110 mm, this setup can be adapted into various sorts of magnets including electromagnets, which have a much lower running cost than the superconducting magnets. Furthermore the temperature control was optimized to have maximum stability in the room-temperature range contrary to temperature controls heating from liquid nitrogen or helium temperatures. The cavity is surrounded by a cover, which ensures thermal homogeneity and near-adiabatic conditions via thermal isolation from the environment. The design of the temperature control system was based on the ability to choose the temperature range by a secondary cooling liquid (see Fig. 1) in order to obtain maximum temperature stability during the measurements. The temperature, process control, and the data acquisition are controlled from a LABVIEW interface.

A detailed scheme of the cavity is shown in Fig. 2 and the basic design parameters are given in Table I. In order to minimize heat losses to the surroundings the calorimeter unit is placed in a vacuum chamber equipped with a gold radiation reflection shielding. The DSC signal in the cavity is acquired by two differentially connected heat flow sensors, which represent the sample (S) and the reference (R). In the

TABLE I. Design parameters for the experimental setup.

Element	Dimension (mm)	Specification
Sensor Peltier elements	3×4	Supercool PE-018–03–09
Temperature control Peltier element	62×62	Supercool PE-127–20–15
Cold finger	$110\times20^{\phi}$	Copper
Thermoresistor element	2×3	Pt100 element 100 Ω
Power supply		Instek PSH 2018 20V/18A
Multimeter		Keithley 2700 40 channels
Hall sensor	2×3	Arepoc AHP-H3Z
Grease for mounting of the sample		Apiezon H-grease

present setup the samples were mounted directly on the upper surface of the sample holder without the use of a pan, therefore, in order to ensure a good thermal contact thermal grease (Apiezon® H-grease) is used. The thermal grease was investigated for a possible phase transition well below the operating temperature range of the DSC, and no visible indication of a phase transition was found in this range. This observation combined with the fact that a very small amount of grease (~0.1 mg) was used allowed us to treat the grease as part of the background. The heat capacity of the grease is subtracted from the sample signal by including the grease used to mount the sample, when measuring the empty sample holder in the addenda measurement. The cavity temperature is simultaneously recorded by a resistance temperature detector which is situated in the proximity of the sample/reference (Thermoelement) [Fig. 2(b)]. A signal from a second sensor is used as feedback signal for the temperature proportional-integral-derivative (PID) controller [Fig. 2(a)].

Since the operation temperature range of this equipment was designed to be around room temperature, it was sufficient to control the temperature in the range of 200–340 K. The temperature range of this device can be expanded in the future to lower or/and higher temperatures.

B. Data acquisition

When heat passes through a Peltier element it generates a voltage drop U_p, which is proportional to the heat flow Q_p passing through the specific element to the heat sink:

$$U_p = \frac{S}{k} Q_p, \tag{3}$$

where S is the Seebeck coefficient and k is the thermal conductance of the Peltier element.[7] At constant external conditions (temperature, pressure, and magnetic field) S/k is constant and U_p can therefore be used directly as a measure of the heat flow. The heat capacity C_p

$$C_p(T) = \frac{Q_p}{\dot{T}_s} = \frac{k}{S}\frac{U_p}{\dot{T}_s}, \tag{4}$$

is then derived by the classical three-step procedure[12] from three successive temperature scans of the sample: (1) scan of the sample, (2) scan of the reference sample (for the calibration of the heat capacity we have used copper (99.999% Cu) as a reference material[12,13]), and (3) scan of an empty sample holder for determining the background signal. As described above the background signal includes the amount of Apiezon H-grease used to mount the sample subsequently. During these scans the temperature is ramped at a constant rate. Keeping the experimental conditions identical, i.e., sample weight and heating/cooling rates, in all three scans the heat capacity can then be derived point by point for a range of temperatures[2]

$$C_{p,\text{sample}}(T) = \frac{U_{\text{sample}}(T) - U_0(T)}{U_{\text{ref}}(T) - U_0(T)} \frac{m_{\text{ref}}}{m_{\text{sample}}} C_{p,\text{ref}}(T). \tag{5}$$

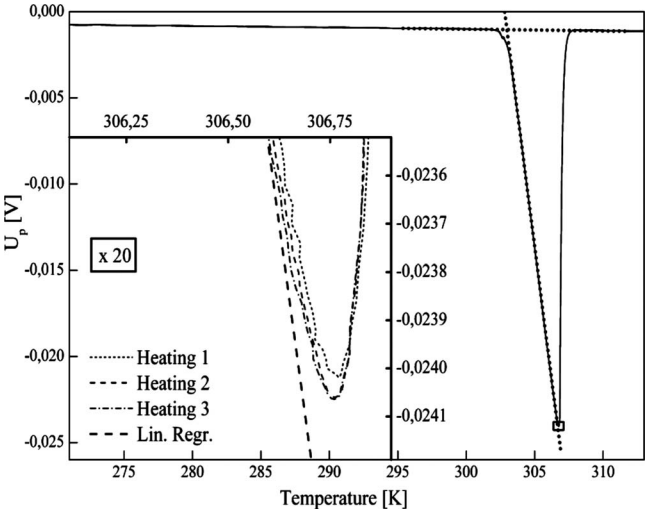

FIG. 3. Temperature calibration using the onset melting point (303.05 K) of gallium as reference material. Inserted figure shows the peak of the melting point magnified 20 times.

C. Calibration

The temperature measured in the setup has been calibrated by using the onset melting point of gallium (303.05 K) (Ref. 14) with high purity (99.999%). The onset of the melting temperature used for the calibration is determined by the crossing point of the base level and slope of the peak during heating as shown in Fig. 3. The base level and the slope of the peak are determined by linear regression of the data below and above the melting peak and the linear range of the melting peak between 303.5 and 306.5 K, respectively. The temperature calibration is only valid for a specific heating rate, and in our experiments, we kept the heating rate constant at 1 K/min and the sample and reference of comparable sizes.

Besides the temperature calibration Fig. 3 demonstrates the excellent reproducibility of the measurements. In this case an endothermic process within the sample is recorded and illustrates the melting behavior of the material. Changes in ramping rate, heat loss, and thermal conductance would show up in the position of the melting peak. The very good reproducibility is illustrated by the inset, where three successive runs are shown. Furthermore, the melting enthalpy of gallium has been calculated and compared to values from the National Institute of Standards and Technology (NIST). The enthalpy of melting given by the NIST database[15] is 80.097 J/g in a 99.9999% pure Ga standard sample, whereas we calculated the enthalpy from our heat capacity data to be 80.8 ± 0.2 J/g in a 99.999% pure Ga sample, which implies a deviation of less than 1% including deviations due to differences in purity.

III. RESULTS

Since this setup was built for the purpose of characterizing the heat capacity of magnetocaloric materials as function of temperature and applied magnetic field, the sensitivity of the DSC needs to be tested on a much weaker signal e.g., from a magnetic phase transition. The magnetic phase transition from the ferromagnetic (FM) to paramagnetic (PM)

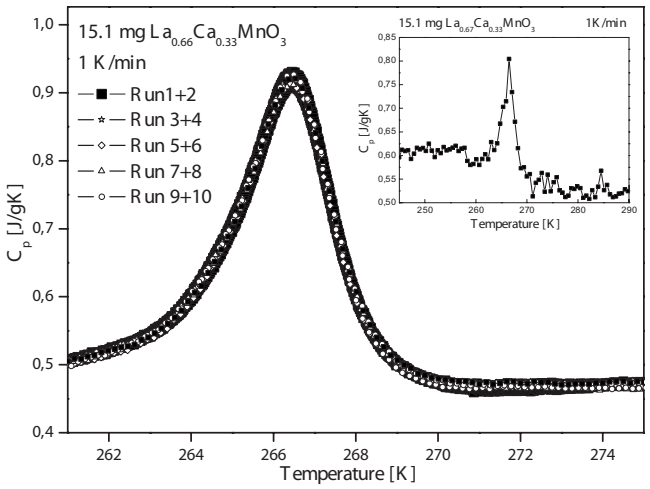

FIG. 4. Heat capacity as function of temperature in ten successive runs on the same 15.1 mg $La_{0.67}Ca_{0.33}MnO_3$ sample in zero magnetic field obtained by the new calorimeter. The inset shows heat capacity data of the same sample obtained in a Seiko DSC-120 commercial DSC setup.

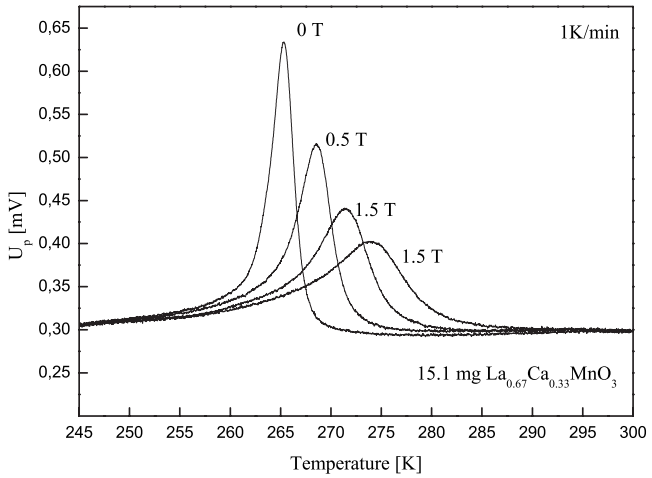

FIG. 5. The 15.1 mg $La_{0.67}Ca_{0.33}MnO_3$ sample measured in four different magnetic fields with the new calorimeter.

state in the $La_{0.67}Ca_{0.33}MnO_3$ system represents a signal, which is more than 50 times weaker than the melting of gallium. $La_{0.67}Ca_{0.33}MnO_3$ (LCMO) was chosen since it is considered to be one of the possible candidate refrigerants in the field of room-temperature magnetic refrigeration and has a transition just around 267 K(Ref. 16) depending on the exact way of synthesis and heat treatment.

Figure 4 shows the results from ten successive runs on a 15.1 mg LCMO sample and heating/cooling rate of 1 K/min. The signal due to the FM to PM transformation is measured to be only around 0.3 mV, whereas the signal from the melting of gallium was of the order 20 mV, i.e., the FM to PM signal is nearly two orders of magnitude smaller. The reproducibility of the signal and an excellent signal-to-noise ratio is, however, upheld, which demonstrates very well the capabilities of this measuring technique and the setup. The characteristic "lambda shape" of the phase transition is also clearly recognized.

The signal-to-noise ratio of the new DSC developed in our laboratory can be estimated by defining a noise band covering all measured data values in a linear part of the data set. This noise band includes the electrical noise of the measurement as well as the main contribution to the noise, namely, fluctuations in the signal derived from thermal fluctuation during the heating/cooling experiment. The width of the noise band can then be evaluated with the signal strength in a given phase transition investigated at a given heating rate. The width of the noise band has been estimated to be maximum 2.5 μV over a 7 K range during heating at 1 K/min. With signal strength similar to the magnetic phase transition peak shown in Fig. 4 peaking around 0.3 mV, this will lead to a signal-to-noise ratio above 100/1. The much stronger signal from the melting of Ga shown in Fig. 3 is exceeding 20 mV at the peak, leading to a signal-to-noise ratio of more than 800/1 in that experiment. A zero-field heat capacity measurement of the same sample (Fig. 4 inset) measured in a commercial DSC setup (Seiko 120-DSC) led to a signal-to-noise ratio of less than 10/1 for the same sample and experiment conditions.

Sample sizes between 10 and 100 mg are typically used in conventional DSC measurements depending on the exact material and experiment. As demonstrated when comparing the results in Fig. 4 and the inset in Fig. 4, the relative low weight when considering conventional DSC measurements of the 15.1 mg LCMO sample results in a very high signal-to-noise ratio in the setup described in this work, whereas to obtain equally good results in the commercial DSC it would be necessary to increase the sample size significantly or to change the heating rate.

On the results presented in Fig. 4 it furthermore becomes evident that even smaller samples would still give a satisfactory signal-to-noise ratios when measuring on FM to PM transitions.

The reproducibility and an excellent signal-to-noise ratio is hereby validated, confirming the results from the Ga runs (Fig. 3). Further, the enthalpy corresponding to the magnetic phase transition for the LCMO sample is more than 50 times smaller than that of the melting enthalpy of Ga, and the reproducibility of the LCMO transition is therefore an important figure of merit for the performance of the new calorimeter.

The calorimeter has also been tested under applied magnetic fields. Figure 5 shows the influence of an applied magnetic field on the magnetic phase transition for the LCMO sample. As expected, the applied magnetic field changes the Curie temperature (T_C) to higher temperatures and tends to broaden the shape of the phase transition. These results correspond well with the results obtained by direct measurements previously reported.[17] The absolute comparison of our results and the results reported in the literature for the same material composition are not possible since the properties of these materials are very sensitive to the preparation procedure. e.g., heat treatment.

For a direct comparison with alternative measuring techniques the same ceramic material was measured in a Quantum Design® physical properties measuring system (PPMS). The results are shown in Fig. 6 and demonstrate an excellent agreement between the two techniques. The PPMS uses a relaxation technique and requires up to 40 min per measuring

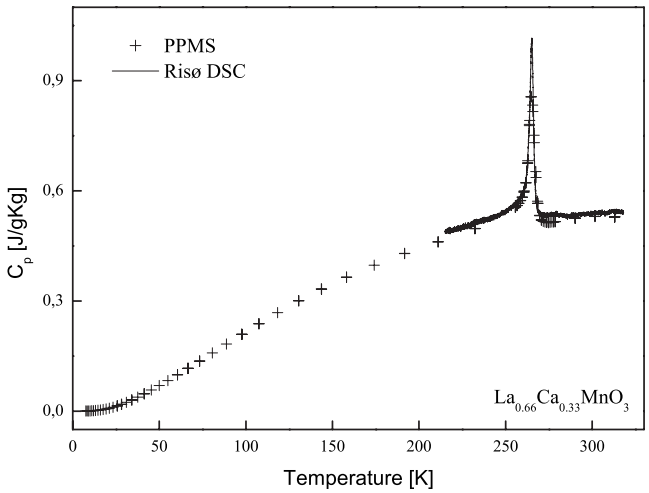

FIG. 6. $La_{0.67}Ca_{0.33}MnO_3$ sample measured in a Quantum Design PPMS system and compared to the measurement from the DSC setup described in this article.

point, whereas scans with the Risø DSC is normally carried out with a scan rate of 1 K/min and 2 Hz data logging frequency. This difference is also easily recognized in Fig. 6 where the data set from the Risø DSC shows much higher density of the data.

IV. CONCLUSION

A novel DSC was constructed for the purpose of characterizing magnetocaloric materials in the near room-temperature range (200–340 K). A significant improvement of the signal-to-noise ratio has been observed when compared to a conventional zero magnetic field DSC. Test results on pure Ga and $La_{0.67}Ca_{0.33}MnO_3$ have been presented to demonstrate the performance of the setup. Test runs as a function of applied magnetic field demonstrate the ability of this device to operate correctly under applied magnetic fields up to 1.8 T. The results from the DSC are in good agreement with results obtained in a commercial PPMS system from Quantum Design®.

ACKNOWLEDGMENTS

The authors acknowledge M. Christensen for carrying out the PPMS measurements in Department of Chemistry at the University of Aarhus, T. Henriksen for carrying out the programming of the LABVIEW interface, A.R. Dinesen for useful discussions during construction of the calorimeter, and A. Junod for helpful correspondence. For technical assistance Jørgen Geyti, Jens F.S Borchsenius, and Jørgen Poulsen are acknowledged.

[1] A. Tishin and Y. Spichkin *The Magnetocaloric Effect and its Applications* (IOP, Bristol, 2003).
[2] B. F. Yu, Q. Gao, B. Zhang, X. Z. Meng, and Z. Chen, Int. J. Refrig. **26**, 622 (2003).
[3] K. A. Gschneidner, Jr., V. K. Pecharsky, and A. O. Tsokol, Rep. Prog. Phys. **68**, 1479 (2005).
[4] E. Bruck, O. Tegus, D. T. C. Thanh, and K. H. J. Buschow, J. Magn. Magn. Mater. **310**, 2793 (2007).
[5] V. K. Pecharsky and K. A. Gschneidner, J. Appl. Phys. **86**, 565 (1999).
[6] V. K. Pecharsky, J. O. Moorman, and K. A. Gschneidner, Rev. Sci. Instrum. **68**, 4196 (1997).
[7] T. Plackowski, Y. X. Wang, and A. Junod, Rev. Sci. Instrum. **73**, 2755 (2002).
[8] J. Marcos, F. Casanova, X. Batlle, A. Labarta, A. Planes, and L. Manosa, Rev. Sci. Instrum. **74**, 4768 (2003).
[9] M. Kuepferling, C. P. Sasso, V. Basso, and L. Giudici, IEEE Trans. Magn. **43**, 2764 (2007).
[10] A. Szewczyk, M. Gutowska, B. Dabrowski, T. Plackowski, N. P. Danilova, and Y. P. Gaidukov, Phys. Rev. B **71**, 224432 (2005).
[11] A. Szewczyk, M. U. Gutowska, K. Piotrowski, M. Gutowski, M. T. Borowiec, V. P. Dyakonov, V. L. Kovarskii, H. Szymczak, and L. Gladczuk, J. Phys.: Condens. Matter **10**, 10539 (1998).
[12] G. W. H. Höhne, W. F. Hemminger, and H. J. Flammersheim, *Differential Scanning Calorimetry* (Springer, Berlin, 2003).
[13] G. Furukawa, W. Saba, and M. Reilly, Natl. Stand. Ref. Data Ser. **18**, 1 (1968).
[14] K. J. Chau, K. M. Rieckmann, and A. Y. Elezzabi, Appl. Phys. Lett. **90**, 131114 (2007).
[15] NIST Standard Reference Materials, 2005, https://srmors.nist.gov/tables/pdf/203_5.pdf
[16] A. R. Dinesen, S. Linderoth, and S. Morup, J. Magn. Magn. Mater. **253**, 28 (2002).
[17] A. R. Dinesen, "Magnetocaloric and magnetoresistive properties of $La_{0.67}Ca_{0.33-x}Sr_xMnO_3$," Ph.D. thesis, Risø National Laboratory, Technical University of Denmark, 2004.

APPENDIX C

Paper presented at The Second IIF-IIR International Conference on Magnetic Refrigeration at Room Temperature, 2007

Paper II

Indirect measurement of the magnetocaloric effect using a novel DSC with magnetic field.
Jeppesen, S.,Linderoth, S., Pryds, N. and Theil Kuhn, L. Conference Proceedings Thermag 2007.

INDIRECT MEASUREMENT OF THE MAGNETOCALORIC EFFECT USING A NOVEL DSC WITH MAGNETIC FIELD

S. Jeppesen*, S. Linderoth, N. Pryds, L. Theil Kuhn
Risø National Laboratory, Fuel Cells and Solid State Chemistry Department
Technical University of Denmark
Frederiksborgvej 399, DK-4000 Roskilde, Denmark

ABSTRACT

A new magnetic field differential scanning calorimeter (DSC) has been built for indirect determination of the magnetocaloric effect. The principle for constructing the calorimeter is based on that suggested by Plackowski et al.[1], where commercial Peltier elements are used as heat-flow sensors. Measurements obtained with the new DSC have been compared with a zero-field commercial DSC. A case study with the LaCaMnO system and gallium has been performed to demonstrate the sensitivity and the accuracy of the setup.

1 INTRODUCTION

Knowledge of the heat capacity of a material as a function of temperature is important in the determination of the thermodynamic properties of a material. The use of calorimetry to investigate the magnetocaloric effect (MCE) is a well-known technique in the field of room temperature magnetic refrigeration. As pointed out by Peckarsky and Gschneider calorimetry provides a method to minimize the systematic errors in the calculation of the isothermal magnetic entropy change from heat capacity data as opposed to magnetization data [2]. DSC is a widely used thermo-analytical technique which provides qualitative and quantitative information about physical or chemical processes in a condensed phase. However, the ability to conduct thermal measurements as function of applied magnetic field is still quite rare {Marcos, 2003 187 /id}. {Marcos, 2003 187 /id}
Different methods to determine the MCE have been suggested in the literature [3-5]:

1. Direct measurement. Measurements of the temperature change ΔT by moving the sample in and out of the magnetic field region.
2. Indirect measurement. Magnetization method: By determining the magnetization curves at various temperatures data on the magnetic contribution to the entropy change ΔS can be extracted.
3. Indirect measurement. Calorimetric method: By measuring specific heat capacity as a function of temperature at various magnetic field strengths.

Method 2 is the most commonly used while methods 1 and 3 require specialized equipment.
Clearly, the determination of the thermodynamic properties of materials, which exhibit a MCE requires a reliable and accurate determination of the heat capacity of a sample under magnetised conditions. Therefore, we have recently constructed a new DSC, which can operate under magnetic field. The aim of this article is to provide the basic information of the DSC setup as well as to report some of the preliminary results obtained by this equipment.

2 EXPERIMENTAL DETAILS

2.1 Construction of the calorimeter

The design of the new calorimeter was guided by the following criteria:

1. Accurate heat capacity measurements under magnetic field.

* Corresponding author: stinus.jeppesen@risoe.dk, Phone: +45 4677 5774, Fax. +45 4677 5858

2. The MCE must be determined around room temperature.
3. The measurement should be performed in near adiabatic conditions.

To meet these requirements the heat flow in the calorimeter is controlled by Peltier elements. This method is based on a previously designed calorimeter by Plackowski et al.[6]. The dimensions of our calorimeter were chosen with a total diameter of 20 mm and a height of 110 mm in order to reach into the magnetic field region and still ensure a stable temperature control. The basic design parameters are given in Table 1. The overall layout of the DSC is shown in Figure 1. In order to eliminate the heat losses to the surroundings the calorimeter unit is placed in a vacuum chamber equipped with reflection shielding to minimize the conduction and radiation losses respectively. Since the operation temperature range of this equipment was designed to be around room temperature, it was sufficient to control the temperature by a single Peltier element (See 2 in Figure 1), which allows a temperature range from –40°C to 50°C. The temperature range can be expanded to lower temperatures by cooling the base plate (See 1 in Figure 1) to lower temperatures.

Table 1 Design parameters for the experimental setup

Element	**Dimension**	**Specification**
Sensor Peltier elements	3mm × 4mm	Supercool PE-018-03-09
Temperature control Peltier element	62mm × 62mm	Supercool PE-127-20-15
Cold finger	110mm × 20mm^{ø}	Copper
Pt100 thermoresistor element	2mm × 3mm	100 Ω
Instek PSH 2018 power supply		20V / 18A
Keithley 2700 Multimeter		40 channels

The device basically consists of Peltier elements which are used as temperature regulator and heat flow sensors. The heat source is connected to a copper bar which acts as a heat sink. The sample (S) and a reference (R) (See Figure 1) are placed on top of two Peltier elements which are used as heat flow sensors. The temperature and process control plus the data acquisition are controlled using a LabView interface.

The heat capacity of this device is calibrated as follows: the flow sensor generates a voltage drop U_P from each element. U_P is proportional to the heat flow j_Q passing through the specific element to the heat sink. A measurement takes place by varying the temperature of the heat sink at constant rate and the heat capacity of the sample may then be derived from [7]

$$C_{P,H}(T_s) = \frac{j_Q}{\dot{T}_s} = -\frac{U_P}{A\dot{T}_s},$$

where T_s is the sample temperature, and $A = U_P / j_Q$ is the so-called sensitivity of the heat flow sensor.
The calibration of the calorimeter is presently being checked by several other methods, such as: (1) electric resistance which can be used to create a well-defined heat-flow through the Peltier element at different temperatures enabling the construction of a transfer function and (2) a conventional 3-step-method (See for example [8]), where the empty crucibles, reference material and sample are measured in analogue experiments. The calibration of the heat capacity of the setup is currently ongoing and will therefore be described at a later stage.

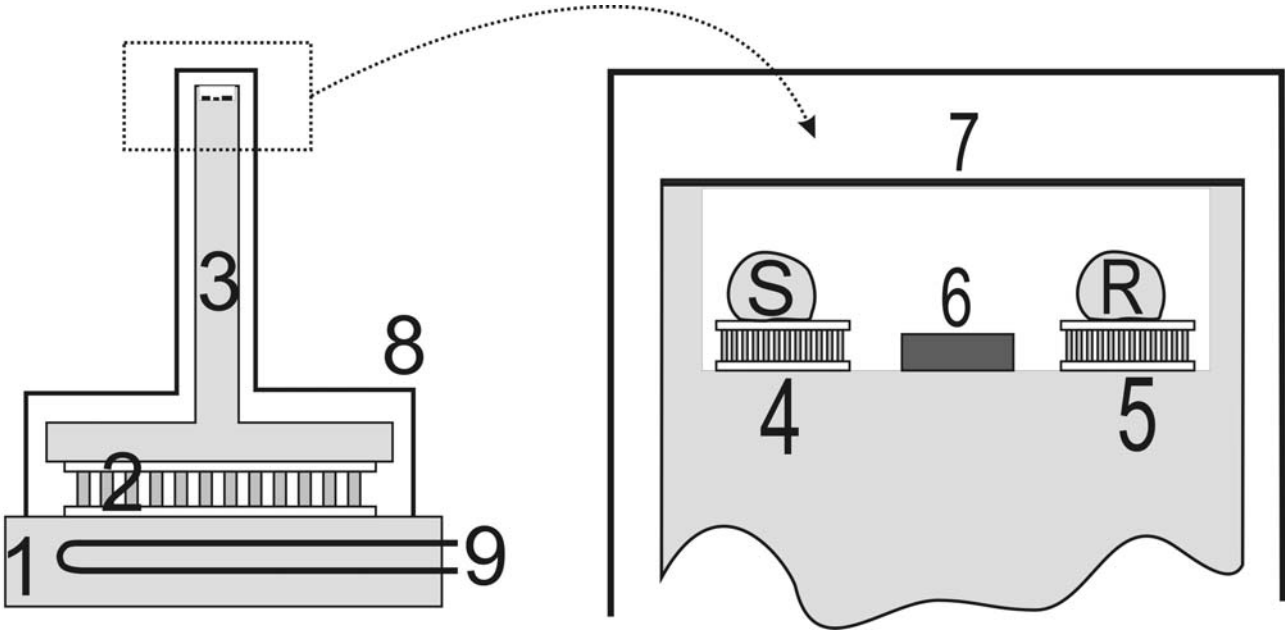

Figure 1 Sketch of the setup A water-cooled bottom plate made of copper (1+9) provides the platform for the setup. On top of the copper plate a large Peltier element (2) is placed in order to either cool or heat the "cold finger" (3) also made from copper. Thermal grease is used to ensure a good thermal contact between the Peltier element, the bottom plate and "cold finger" respectively. The "cold finger" (3) reaching into the magnetic pole gap provides control of the sample temperature inside the magnetic pole gap. The DSC signal is acquired by two differentially connected heat flow sensors (4,5) (Peltier elements) the sample (S) sitting on (4) and the reference (R) on (5). The local temperature is simultaneously logged by a thin-film resistance temperature detector (RTD) (6) (e.g. a Pt100 sensor). The RTD signal is also be used as input signal for the temperature controller. A gold plate (7) thermally anchored to the heat sink is mounted in order to minimize radiation losses to the surroundings, and the entire calorimeter is placed within a vacuum shield (8) made of stainless steel to minimize heat loss or uptake by convection. The joint between the shield and the bottom plate is sealed with an O-ring. A pipefitting mounted at the side of the shield allows for connection of a vacuum turbo pump station.

2.2. Materials

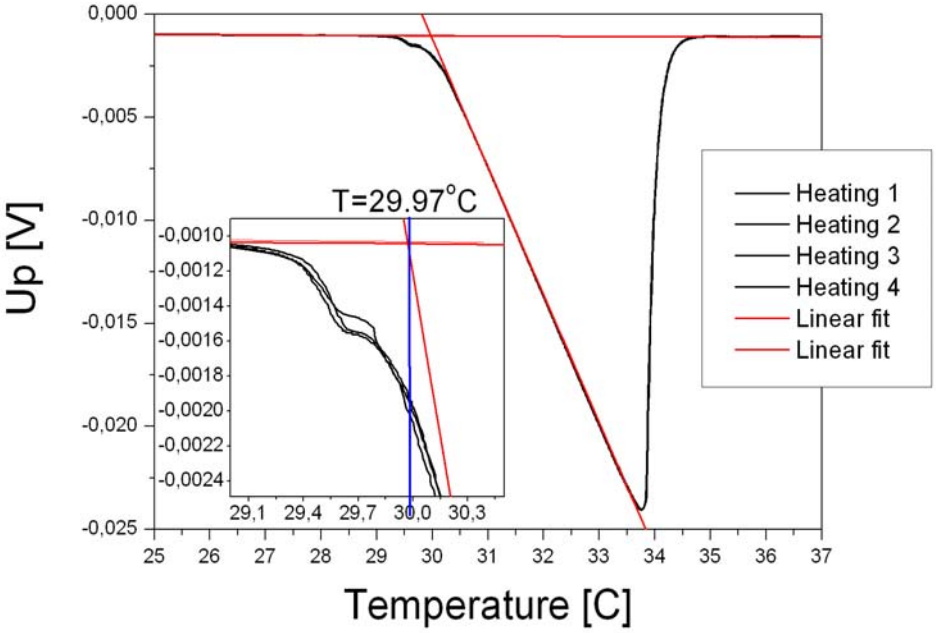

Figure 2 Temperature calibration using the onset melting point of Gallium as reference material. Inserted figure shows a close-up of the onset melting of Gallium.

In the preliminary experiments done with this equipment, different materials have been investigated to examine the stability and the accuracy of the setup. Pure gallium (99.999% purity) was used as the reference material. It was cut and weighed in a micro balance with accuracy better than 0.1 mg. Before the sample was heated to above its melting temperature it was kept isothermally at 26ºC for about 60 min to permit the sample to equilibrate to the surroundings and the Al-crucible. For comparison DSC curves in zero magnetic field were recorded using a heating rate of 1K/min, using both the new calorimeter and a commercial DSC (Netzsch DSC 404C).
The magnetic phase transition from ferromagnetic to paramagnetic in a $La_{0.67}Ca_{0.33}MnO_3$ sample, which is a perovskite ceramic material with Curie temperature T_C of 266K, was also investigated. The sample was prepared by powder synthesis using a glycine-nitrate combustion technique[9] from nitrate solutions of the elements. The powder was calcinated at 1375 K for 5h before pressed into pellets at isostatic pressure of approximately 110 MPa and sintered at 1775 K for 5h. From one pellet a 15.1 mg sample was cut for the experiments. The detailed preparation procedure and magnetic characterization of this sample is given in [10]

3 RESULTS

In order to test the temperature calibration of the setup the onset melting temperature of Gallium has been measured (See Figure 2). Gallium was chosen since the onset temperature of this material is close to room temperature (29.97 ^{O}C for a heating rate of 1 K/min [8]). As one can see from Figure 2, several heating cycles were conducted starting below the melting temperature of Ga. The endothermic reaction is clearly observed and it is attributed to the melting of Ga. The results are highly reproducible proving reliability and stability of the equipment. The onset transition temperature of Ga is therefore used to calibrate the temperature measured in the setup. It should be noted that over a series of temperature cycles, a layer of gallium-aluminium alloy developed at the sample-crucible interface [11]. This layer is the reason for the observation of a double melting peak

(Figure 2 inserted figure). Figure 3 shows a temperature cycle for Ga indicating the importance to perform a complete solidification at temperatures well below the melting point before starting a new measurement of the melting enthalpy dependent on the cooling rate and material properties.

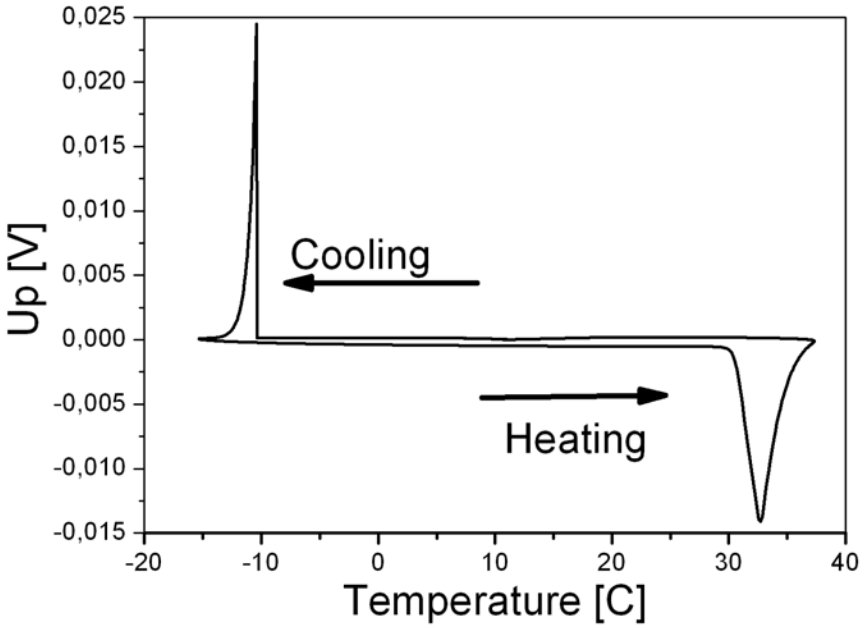

Figure 3: Temperature cycle for Ga indicating the importance to perform a complete solidification at temperatures well below room temperature before starting a new DSC measurement of the melting of Gallium.

Since the calorimeter was built for the purpose of characterizing the MCE of different materials, we would like to demonstrate the ability to observe a magnetic phase transition in a perovskite ceramic material.

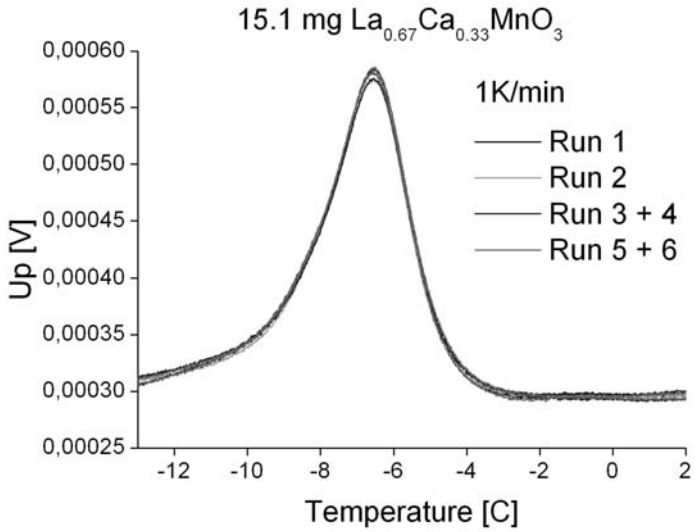

Figure 4: 6 successive runs on the same 15.1 mg LaCaMnO sample in zero magnetic field obtained by the calorimeter presented in this article.

The signal describing the melting enthalpy of Ga is so strong that it does not give a proper picture of the signal-to-noise ratio for the samples of our interest, i.e. magnetic phase transitions. To verify a high signal to noise ratio of our calorimeter

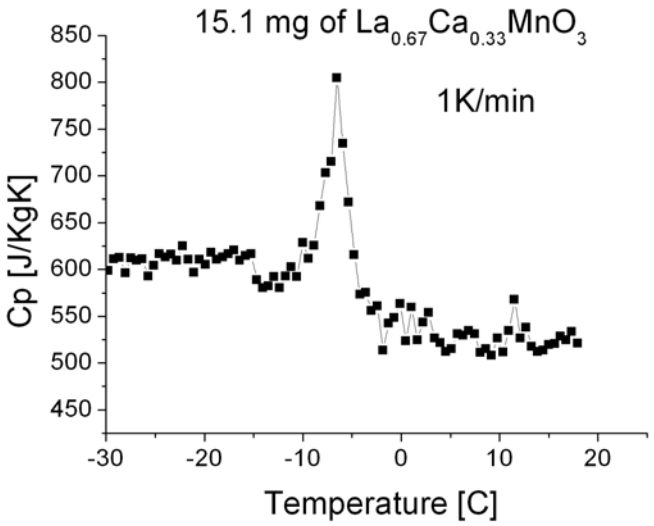

Figure 5 Heat capacity data of 15.1 mg LaCaMnO sample obtained in a Seiko DSC-120 commercial DSC setup

a $La_{0.67}Ca_{0.33}MnO_3$ sample was therefore chosen to demonstrate the quality of the signal. $La_{0.67}Ca_{0.33}MnO_3$ has a ferromagnetic (FM) to paramagnetic (PM) transition at a Curie temperature around room-temperature [12]. $La_{0.67}Ca_{0.33}MnO_3$ has previously been found to have a T_C of -6 °C [13]. This sample was measured in the new calorimeter in zero magnetic field and compared to a commercial DSC setup (Seiko 120-DSC). The peak corresponding to the FM-PM transition using the two equipments is shown in Figures 4 and 5.

As seen from the figures the signal-to-noise ratio of the new DSC developed in our laboratory is much better, actually at least two orders of magnitude superior to the commercial DSC setup. In the new calorimeter the signal to noise ratio is approximately 700/1 compared to a value of approximately 7/1 in the commercial Seiko 120-DSC. Another valuable information which can be extracted from Figure 4 is the reproducibility of the measured signal. Figure 4 shows the plot of the data from 6 successive heating runs of the same LaCaMnO sample (LCM). The reproducibility and an excellent signal-to-noise ratio is hereby validated, confirming the results from Ga (Figure 2). Further, the enthalpy corresponding to the magnetic phase transition for the LCM sample is approximately 100 times smaller than that of the melting enthalpy of Ga, and the reproducibility of the LCM transition is therefore an important figure of merit for the performance of the new calorimeter.

Finally, the calorimeter has been tested under applied magnetic fields. Figure 6 shows the influence of an applied magnetic field on the magnetic phase transition for a $La_{0.67}Ca_{0.33}MnO_3$ sample. As expected, the applied magnetic field changes T_C towards higher temperature and to broaden the peak of the phase transition. These results correspond well with the results made by direct measurements previously reported in [14].

Figure 6 $La_{0.67}Ca_{0.33}MnO_3$ sample measured in different magnetic fields with the calorimeter presented in this article

4 CONCLUSION

We have constructed a novel DSC for the purpose of characterizing magnetocaloric materials in the near room temperature range (233–323 K). A significant improvement of the signal-to-noise ratio has been observed when compared to a conventional zero magnetic field DSC. A few preliminary results on pure Ga and LaCaMnO have been presented to demonstrate the sensitivity of the setup. Test runs as function of applied magnetic field demonstrates the ability of this device to operate correctly under applied magnetic fields up to 1.4 Tesla. These results correspond well with the data published in the literature.

ACKKNOWLEDGEMENTS

The authors acknowledge T. Henriksen for carrying out the programming of the LabView interface, AR Dinesen for useful discussions during construction of the calorimeter, and A. Junod for helpful correspondence.

REFERENCES

Reference List

[1] T. Plackowski, Y.X. Wang, A. Junod, Specific heat and magnetocaloric effect measurements using commercial heat-flow sensors. Review of Scientific Instruments 73 (2002) 2755-2765.

[2] V.K. Pecharsky, K.A. Gschneidner, Magnetocaloric effect from indirect measurements: Magnetization and heat capacity. Journal of Applied Physics 86 (1999) 565-575.

[3] A.R. Dinesen, S. Linderoth, S. Morup, Direct and indirect measurement of the magnetocaloric effect in a La0.6Ca0.4MnO3 ceramic perovskite. Journal of Magnetism and Magnetic Materials 253 (2002) 28-34.

[4] V.K. Pecharsky, K.A. Gschneidner, Magnetocaloric effect from indirect measurements: Magnetization and heat capacity. Journal of Applied Physics 86 (1999) 565-575.

[5] T. Plackowski, Y.X. Wang, A. Junod, Specific heat and magnetocaloric effect measurements using commercial heat-flow sensors. Review of Scientific Instruments 73 (2002) 2755-2765.

[6] T. Plackowski, Y.X. Wang, A. Junod, Specific heat and magnetocaloric effect measurements using commercial heat-flow sensors. Review of Scientific Instruments 73 (2002) 2755-2765.

[7] T. Plackowski, Y.X. Wang, A. Junod, Specific heat and magnetocaloric effect measurements using commercial heat-flow sensors. Review of Scientific Instruments 73 (2002) 2755-2765.

[8] G.W.H. Höhne, W.F. Hemminger, H.J. Flammersheim Differential Scanning Calorimetry, Springer-Verlag, 2003.

[9] L.A. Chick, L.R. Pederson, G.D. Maupin, J.L. Bates, L.E. Thomas, G.J. Exarhos, Glycine Nitrate Combustion Synthesis of Oxide Ceramic Powders. Materials Letters 10 (1990) 6-12.

[10] A.R. Dinesen, S. Linderoth, S. Morup, Direct and indirect measurement of the magnetocaloric effect in La0.67Ca0.33-xSrxMnO3 +/-delta (x is an element of [0; 0.33]). Journal of Physics-Condensed Matter 17 (2005) 6257-6269.

[11] D.M. Price, Temperature calibration of differential scanning calorimeters. Journal of Thermal Analysis 45 (1995) 1285-1296.

[12] A.R. Dinesen, S. Linderoth, S. Morup, Direct and indirect measurement of the magnetocaloric effect in a La0.6Ca0.4MnO3 ceramic perovskite. Journal of Magnetism and Magnetic Materials 253 (2002) 28-34.

[13] A.R. Dinesen, S. Linderoth, S. Morup, Direct and indirect measurement of the magnetocaloric effect in a La0.6Ca0.4MnO3 ceramic perovskite. Journal of Magnetism and Magnetic Materials 253 (2002) 28-34.

[14] A.R. Dinesen. Magnetocaloric and magnetoresistive properties of La0.67Ca0.33-xSrxMnO3. 2004. Risø National Laboratory, August 2004, 103 p., ISBN 87-550-3224-9.
Ref Type: Report

APPENDIX D

Paper from the *Danske Køledage* Conference.

Paper III

Magnetic Refrigeration and the Magnetocaloric Effect
Petersen, TF., Pryds, N., Smith, A., Linderoth, S., and Jeppesen, S.

Magnetic Refrigeration and the Magnetocaloric Effect

Thomas Frank Petersen[1]
Risø National Laboratory,
Materials Research Department,
Frederiksborgvej 399, P.O. 49, DK-4000 Roskilde.
and
Technical University of Denmark,
Department of Mechanical Engineering,
Nils Koppels Allé 403, DK-2800 Lyngby

Nini Pryds, Anders Smith, Søren Linderoth and Stinus Jeppesen
Risø National Laboratory,
Materials Research Department,
Frederiksborgvej 399, P.O. 49, DK-4000 Roskilde.

Hans-Jørgen Høgaard Knudsen
Technical University of Denmark,
Department of Mechanical Engineering,
Nils Koppels Allé 403, DK-2800 Lyngby

Abstract

Magnetic refrigeration at room temperature is an emerging technology for refrigeration, which promises low energy consumption and is environmentally friendly. Magnetic refrigeration is based on the magnetocaloric effect, which manifests itself as a reversible increase in temperature when magnetic materials are placed in a magnetic field. This paper introduces and describes magnetic refrigeration cycles and the magnetocaloric effect, and shows how magnetic refrigeration can be an alternative to vapour-compression refrigeration. A review of the Danish research on magnetic refrigeration at Risø National Laboratory is also provided.

Keywords: Magnetocaloric Effect, Magnetic Refrigeration, Active Magnetic Regenerator, AMR

[1] Corresponding author: Phone:+45 4677 5720, Fax:+45 4677 5758, thomas.frank.petersen@risoe.dk

1 Introduction

Magnetic refrigeration at room temperature is an interesting alternative to conventional refrigeration due to its numerous benefits, among other that, magnetic refrigeration systems are effective and have low energy consumption, the systems are compact and virtually silent and the refrigerants are environmentally friendly.

Magnetic refrigeration uses the magnetocaloric effect (MCE) to provide cooling. The MCE can be observed as an increase in temperature when a magnetic material, kept in thermal isolation (adiabatic conditions), is placed in a magnetic field. This is called the adiabatic temperature change (Figure 1.).

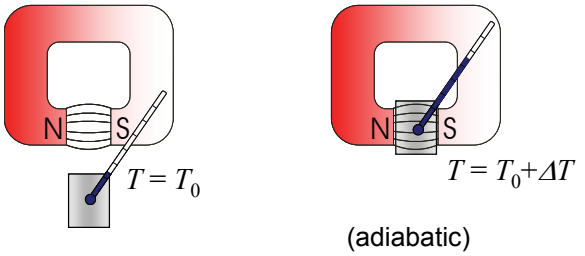

Figure 1: The adiabatic temperature change. The sample has the initial temperature T_0, and is thermally isolated from the surroundings. When the sample is placed in a magnetic field the temperature increases to $T=T_0+\Delta T_{ad}$, illustrated by the thermometer. When the sample is removed from the magnetic field the temperature decreases to T_0 (Dinesen 2004).

Magnetic refrigeration at room temperature is a relatively new field of research, but the MCE has been used in specialized areas of refrigeration since the 1930s. The MCE was discovered in 1881 by Warburg who observed the adiabatic temperature change in iron and in 1918 Weiss and Piccard explained the MCE theoretically. In 1926-1927 Debye and Giauque suggested that the MCE be used to obtain extremely low temperatures (<1 K) using a method called *adiabatic demagnetization* and in 1933 MacDougall verified the method by cooling a sample from 1.5 K to 0.25 K. Giauque was awarded the Nobel price for his research in 1949. Since MacDougall's experiment adiabatic demagnetization has been a standard technique in experimental physics to obtain temperatures from a few kelvin down to a few nano kelvin. In 1976 Brown constructed the first magnetic refrigerator operating at room temperature, using gadolinium as refrigerant and a superconducting magnet. The refrigerator obtained a temperature difference of 51 K (Brown 1976). Subsequently a number of magnetic refrigerators have been build with the most notable development being the magnetic refrigerator constructed in 2001 by the Astronautics Corporation in the USA. This refrigerator uses permanent magnets and eliminates superconducting magnets; an important step for making magnetic refrigeration ready for commercial applications.

Magnetic refrigeration uses the MCE by taking a solid refrigerant through repeated "heat pump" cycles; the general principle is comparable to conventional vapour-compression refrigeration (Figure 2).

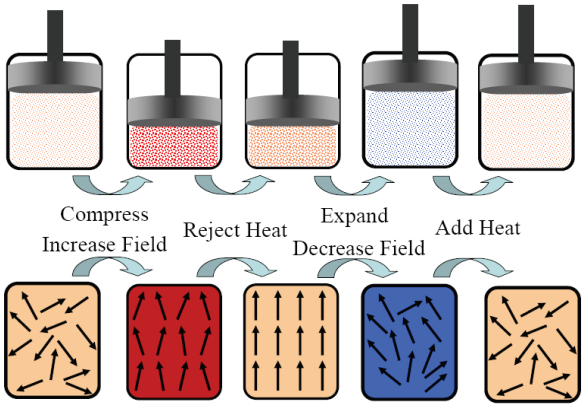

Figure 2: Similarities between vapour-compression and magnetic refrigeration. In the first step the refrigerant (vapour or magnetic solid) is initially at ambient temperature and experiences either a compression or an increased magnetic field to increase the temperature. In the second step the refrigerant rejects heat to the surroundings, and returns to ambient temperature. In the third step the temperature of the refrigerant decreases as it is expanded or the magnetic field is removed. In the fourth step, the refrigerant absorbs heat from the cooling load until it reaches ambient temperature and the cycle can start over. By repeating the cycle the cooling load is continuously cooled (figure from (Nellis et al. 2004)).

The above cooling cycle cannot be used for actual refrigeration because it is limited by the adiabatic temperature change. This is one of the major issues with magnetic refrigeration; even with superconducting magnets, the adiabatic temperature change in gadolinium (the most commonly used material) is approximately 20 K,

and with permanent magnets the change it is approximately 6 K. To increase the MCE, much research is focused towards improving the materials. For the MCE to be used for practical purposes, a magnetic refrigeration system must employ a regenerative cycle, and the AMR (Active Magnetic Regeneration) cycle is the most commonly used today which is explained in detail in section 4. The AMR cycle has been realized in a number of experimental magnetic refrigerators, and virtually all new magnetic refrigerators are based on the AMR cycle.

In the next part of the paper a short review of the research on magnetic refrigeration at Risø in Denmark is presented and in the remainder of the paper magnetic refrigeration cycles and the MCE is described in detail.

2 Magnetic refrigeration at Risø

The Materials Research Department at Risø National Laboratory has investigated the MCE since 2001. The research team currently consists of seven persons, where two are PhD students. The main focus in this research has been the development of new ceramic materials for magnetic refrigerator applications. Recently an AMR refrigerator has also been constructed in order to directly testing the materials suitability for magnetic refrigeration directly. To study and optimize the experimental AMR refrigerator a two-dimensional mathematical model of the AMR is also currently being developed. In the following sections, the three areas of research are described in further detail.

2.1 Materials research

All magnetic materials, to a greater or lesser degree, exhibit the MCE. However, some materials, by virtue of their unique electronic structure or physical nanostructure, display a significantly enhanced MCE, and can potentially be used for magnetic refrigeration. The large magnetic entropy changes at the Curie temperature of certain ceramics (perovskite manganites) have been the focus of much research interests in recent years. The ferromagnetic transition of the $A_{1-x}B_xMnO_y$ type perovskites is accompanied by significant lattice changes at the Curie temperature. The simultaneous occurrence of structural and magnetic transitions can strongly influence the magnetic entropy change. The Curie temperature of these materials covers the entire temperature range from very low temperatures to near 300 K and some show sufficient MCE to be used as magnetic refrigerants. This behaviour indicates that the MCE in these ceramics is high and tuneable and suitable for magnetic refrigerants in a wide temperature interval.

The adiabatic temperature change for $La_{0.67}Ca_{0.33-x}Sr_xMnO_3$ (x=0.0-0.33) was investigated experimentally, and it was found that the Curie temperature can be tuned from 267 K to 369 K, with a corresponding maximum adiabatic temperature change of 1.5 K to 0.5 K respectively (Figure 3).

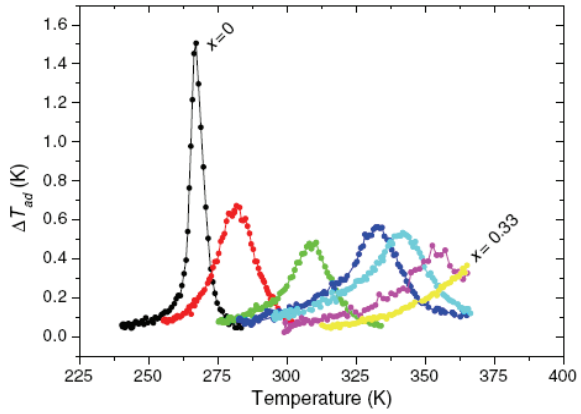

Figure 3: The adiabatic temperature change in $La_{0.67}Ca_{0.33-x}Sr_xMnO_3$ (x=0-0.33) in a magnetic field of 0.7 Tesla. The peak of each curve is centred on the Curie temperature and illustrates that the Curie temperature can be adjusted by changing the composition (Dinesen et al. 2005)

The experimental results show that these ceramics are potential candidates for magnetic refrigeration over a wide temperature range. This work is described in detail in (Dinesen 2004) and (Dinesen et al. 2005). Presently, the materials research has resulted in two scientific articles and a PhD report, and Risø is currently pursuing patents. The materials research is currently continued through a PhD project.

2.2 Experimental active magnetic regenerator refrigerator

Risø has designed, fabricated, and is currently testing a proof-of-concept, magnetic refrigerator based on the concept in Figure 8. The experimental AMR refrigerator uses a linear motion of the refrigerant situated within an electromagnet with a maximum field of about 0.8

T. The motion of the refrigerant is arranged to pass through a gap in the magnet where the magnetic field is concentrated. As it passes through the field, the refrigerant exhibits a MCE and heats up. After entering the field, a stream of water is pushed through the refrigerant to draw the heat out of the material by means of pistons. When the refrigerant leaves the magnetic field, it cools down due to the MCE. A second stream of water is then cooled by the refrigerant. Heat exchangers in each end of the AMR refrigerator provide a heat sink and a cooling load.

2.3 Mathematical modelling of an Active Magnetic Regenerator

The experimental AMR refrigerator executes a complex thermodynamic cycle which cannot by analysed in a simple way. To understand and analyze the AMR cycle it is necessary to use numerical methods, and mathematical modelling has been the subject of several projects in recent years. As part of a PhD project, Risø has developed a two-dimensional model to analyze the experimental AMR refrigerator. The model accounts for the coupled problem of heat transfer and periodic fluid flow under alternating magnetization and demagnetization. The finite element method was used to implement and solve the problem numerically. The model is able to predict the magnetic refrigerator performance at many conditions and will be used to optimize geometry, choice of materials, operating frequency etc. The model is currently used to study the design of the proof-of-concept AMR in detail and publications are forthcoming.

3 Magnetic refrigeration cycles

Magnetic refrigeration can be realized with different thermodynamic cycles; in the following the magnetic Carnot, Brayton, Eriksson and AMR cycles are explained in detail. There are three new types of thermodynamic processes, used in magnetic refrigeration:

- Isothermal magnetization, where the refrigerant is magnetised while the temperature is kept constant; during this process the MCE manifests as a change in entropy (see section 4)
- Adiabatic magnetization, where the temperature of the refrigerant increases due to the adiabatic temperature change.
- The isofield process, where the magnetic field is kept constant.

For a cyclic process the 1st law of thermodynamics is written as:

$$\oint du = \oint dw + \oint dq = 0 \qquad (2.1)$$

where dw refers to the external or technical work. Using the 2nd law of thermodynamics the cyclic work can also be written as:

$$w = -\oint T ds \qquad (2.2)$$

The coefficient of performance (COP) is used to evaluate the effectiveness of a magnetic refrigeration cycles.

$$COP = \frac{q_c}{w} \qquad (2.3)$$

where q_c is the cooling load.

3.1 The Carnot cycle

In magnetic refrigeration cycles the Carnot cycle can be considered the reference cycle. The cycle consists of two isothermal and two adiabatic processes and can be illustrated in a schematic T-S diagram between two isofield lines (Figure 4)

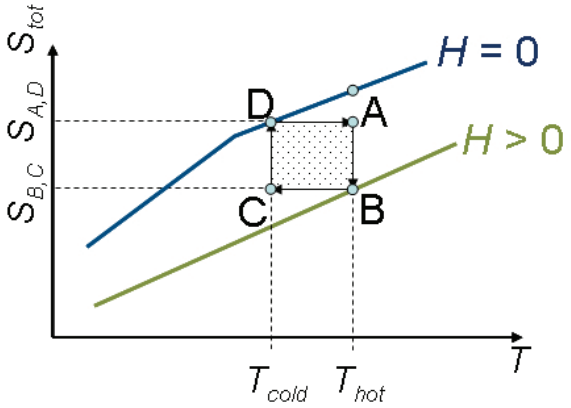

Figure 4: The magnetic Carnot cycle consists of four steps; isothermal magnetization from A to B, adiabatic demagnetization from B to C, isothermal demagnetization from C to D and finally adiabatic magnetization from D to A.

Although the Carnot cycle looks simple, it is complex to realize, and it will be explained in further detail. The cycle starts at point A at the temperature of the hot heat exchanger and a partial magnetic field. From point A to B there is isothermal magnetization as the refrigeration rejects heat while the magnetic field is increased to its maximum strength. From point B to C the temperature of the refrigerant is reduced by

partial adiabatic demagnetization. From point C to D there is isothermal demagnetization as the magnetic field is removed while the refrigerant adsorbs heat from the cold heat exchanger. Finally, from point D to A the refrigerant undergoes partial adiabatic magnetization as the magnetic field is increased until the refrigerant reaches the initial state. The work (the area ABCD) can be calculated from equation (2.2):

$$w = -\oint Tds = -\int_A^B Tds - \int_C^D Tds = T_{hot}\left(s_A - s_B\right) - T_{cold}\left(s_D - s_C\right) \quad (2.4)$$

The cooling load is the heat absorbed during process CD, which can be calculated as:

$$q_c = \int_C^D Tds = T_{cold}\left(s_D - s_C\right) \quad (2.5)$$

The COP is then:

$$COP = \frac{q_c}{w} = \frac{T_{cold}\left(s_D - s_C\right)}{T_{hot}\left(s_A - s_B\right) - T_{cold}\left(s_D - s_C\right)} \quad (2.6)$$

Since the adiabatic process AB and CD have the same entropy difference, equation (2.6) can be further simplified, which leads to the following well know result for the COP of a Carnot cycle:

$$COP = \frac{T_{cold}}{T_{hot} - T_{cold}} \quad (2.7)$$

For practical refrigeration, the temperature span between the hot and cold sink is limited by the high and low isofield curves. Consequently, the hot and cold temperature cannot be chosen freely. Furthermore, the cycle uses a varying magnetic field, as each of the four points experiences a unique magnetic field. This requires an electromagnet or superconducting magnet where the field can be manipulated; this is energy inefficient and makes the Carnot cycle unsuitable for normal refrigeration.

3.2 The Ericsson cycle

For magnetic refrigeration to be used under normal conditions, it is necessary to make the temperature span independent of the cycle. This can be accomplished with regeneration. The Ericsson cycle consists of two isotherms and two isofields and uses regeneration (Figure 5).

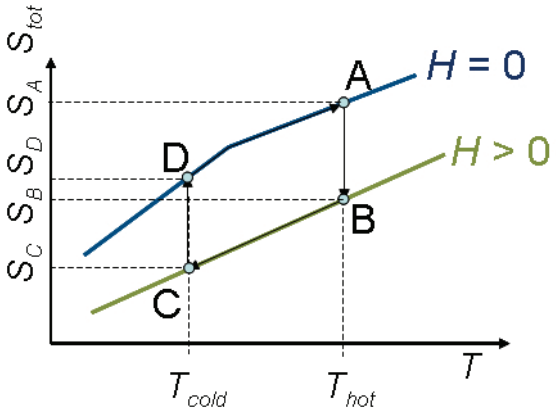

Figure 5: The Ericsson cycle. From A to B there is isothermal magnetization and heat rejection, from B to C isofield cooling and regeneration, from C to D isothermal demagnetization and heat absorption and from D to A isofield heating with regeneration.

Brown used the Ericsson cycle when he built his magnetic refrigerator; as regenerator he used a cylinder filled with a water/alcohol mixture, and the refrigerant, gadolinium, was formed as concentric cylinders, which could slide up and down the length of the regenerator. In each end of the regenerator a heat reservoir was placed to provide isothermal conditions (Figure 6).

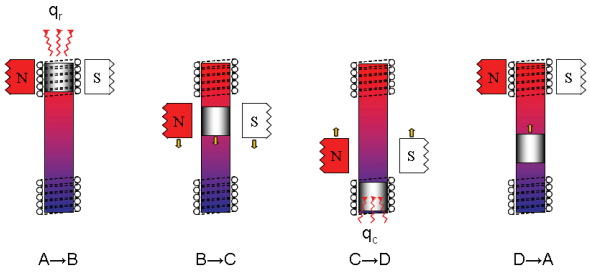

Figure 6: The use of a regenerator in the Ericsson refrigeration cycle. The position of the magnet and refrigerant inside the regenerator during the four steps of the Ericsson cycle shown on Figure 5 is illustrated on the four figures from left to right.

At steady-state there is a temperature gradient along the regenerator and the machine starts with the gadolinium and the magnet positioned at the hot reservoir of the generator. The gadolinium is magnetized and the produced heat is rejected to the hot reservoir which provides isothermal conditions. The gadolinium and the magnet is simultaneously moved down through the regenerator at constant magnetic field during which the gadolinium rejects heat to the regenerator until it reaches the temperature of the cold reservoir. The magnet is moved up to the hot reservoir and the gadolinium is

demagnetized while the gadolinium absorbs heat from the cold reservoir. Finally, the gadolinium is moved up through the regenerator and absorbs heat until it reaches the temperature of the hot reservoir. The regenerator is used to bring the refrigerant from the temperature of the cold heat reservoir to the temperature of the hot reservoir and vice versa. However, because regeneration is driven by temperature differences, it is an irreversible process which decreases the efficiency of the cycle.

The absorbed heat can be determined as:

$$q_c = \int_C^D Tds = T_{cold}\left(s_D - s_C\right) \qquad (2.8)$$

The rejected heat can likewise be determined as:

$$\mathrm{q_r} = \int_A^B Tds = T_{hot}\left(s_B - s_A\right) \qquad (2.9)$$

Finally, the work can be determined as:

$$w = -q_r - q_c = T_{hot}\left(s_A - s_B\right) - T_{cold}\left(s_D - s_C\right) \qquad (2.10)$$

The COP can be calculated from equation (2.8) and (2.10) :

$$COP = \frac{T_{cold}\left(s_D - s_C\right)}{T_{hot}\left(s_A - s_B\right) - T_{cold}\left(s_D - s_C\right)} \qquad (2.11)$$

By letting T_{cold} go to T_{hot} the limit of the COP for the Ericsson cycle becomes that of the Carnot cycle (Kitanovski and Egolf 2005):

$$\lim_{T_{cold}\to T_{hot}} COP = \frac{T_{cold}}{T_{hot} - T_{cold}} \qquad (2.12)$$

3.3 The Brayton cycle

The Brayton cycle is a regenerative cycle similar to the Ericsson cycle; the only difference being that it uses adiabatic instead of isothermal magnetization and demagnetization (Figure 7).

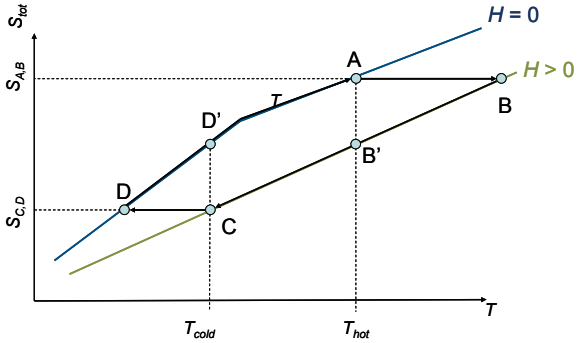

Figure 7: The Brayton cycle: From A to B there is adiabatic magnetization, from B to C isofield heat rejection, and regeneration, from C to D adiabatic demagnetization and from D to A isofield heat absorption with regeneration.

The Brayton cycle uses adiabatic magnetization and demagnetization and heat rejection and absorption must occur during process BC and process DA; this is illustrated on the figure as process BB' and DD'.

The absorbed heat from the cooling load can be determined as:

$$q_c = \int_D^A Tds \qquad (2.13)$$

The rejected heat can likewise be determined as:

$$\mathrm{q_r} = \int_B^C Tds \qquad (2.14)$$

The work is determined from the conservation of energy:

$$w = -q_r - q_c = -\left(\int_B^C Tds + \int_D^A Tds\right) \qquad (2.15)$$

The COP is calculated from equation (2.15) :

$$COP = \frac{\int_D^A Tds}{-\left(\int_B^C Tds + \int_D^A Tds\right)} \qquad (2.16)$$

3.4 The Active Magnetic Regenerator cycle

The AMR cycle consists of adiabatic magnetization and demagnetization and two isofield processes, which make the AMR cycle identical to the Brayton cycle. However, in the AMR the refrigerant provides both refrigeration and regeneration. The essential part of an AMR is a porous regenerator "bed" made of the magnetocaloric refrigerant. Heat exchangers integrated with the refrigerator transport heat from the regenerator to the surroundings and from the cooling load to the regenerator. Because the refrigerant is a solid, the AMR includes a "heat transfer fluid" which couples the refrigerant to the heat exchangers The regenerator bed is immersed in the heat transfer fluid and by means of pistons or pumps the heat transfer fluid can move back and fourth though the regenerator. A refrigerator based on the AMR cycle is best explained with a graphic illustration (Figure 8).

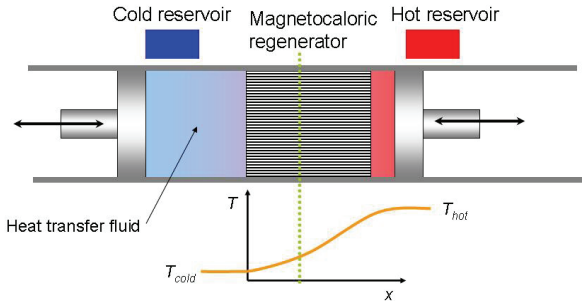

Figure 8: Magnetic refrigerator based on the AMR cycle. The magnetocaloric regenerator is placed in the middle of the refrigerator surrounded by heat transfer fluid. In one end of the regenerator bed a cold reservoir is placed and a hot reservoir is placed in the other end. Pistons in each end can move the heat transfer fluid through the regenerator. The figure inserted at the bottom show the temperature profile through the refrigerator at steady-state.

The AMR cycle starts with the refrigerator in the position shown on Figure 8, with a given temperature gradient through the regenerator bed. The magnetic field is applied which heats the regenerator bed which in turn rejects heat to the heat transfer fluid within the regenerator bed. This results in a new temperature profile. Subsequently the heat transfer liquid is displaced from the cold reservoir towards the hot reservoir (the cold blow). The displacement moves all the heat transfer fluid with a temperature higher than the hot reservoir from the regenerator bed and replace it with cold heat transfer fluid. At the hot reservoir, the heat transfer fluid rejects heat to the surroundings which results in new temperature gradient in the regenerator. The regenerator bed is cooled by demagnetization and absorbs heat from the heat transfer liquid. Finally, the heat transfer liquid is displaced from the hot reservoir to the cold reservoir (the hot blow). The heat transfer fluid with a lower temperature than the cold reservoir is replaced with warm fluid and the cold heat transfer fluid absorbs heat from the cold reservoir (i.e. the cooling load). This returns the temperature gradient to its original level. The essential action of the AMR is the manipulation of the temperature gradient in the regenerator bed to produce liquid with a temperature, which is higher or lower than the temperature of the hot and cold reservoirs respectively. A simplified temperature gradient throughout the cycle can be illustrated in four steps (Figure 9).

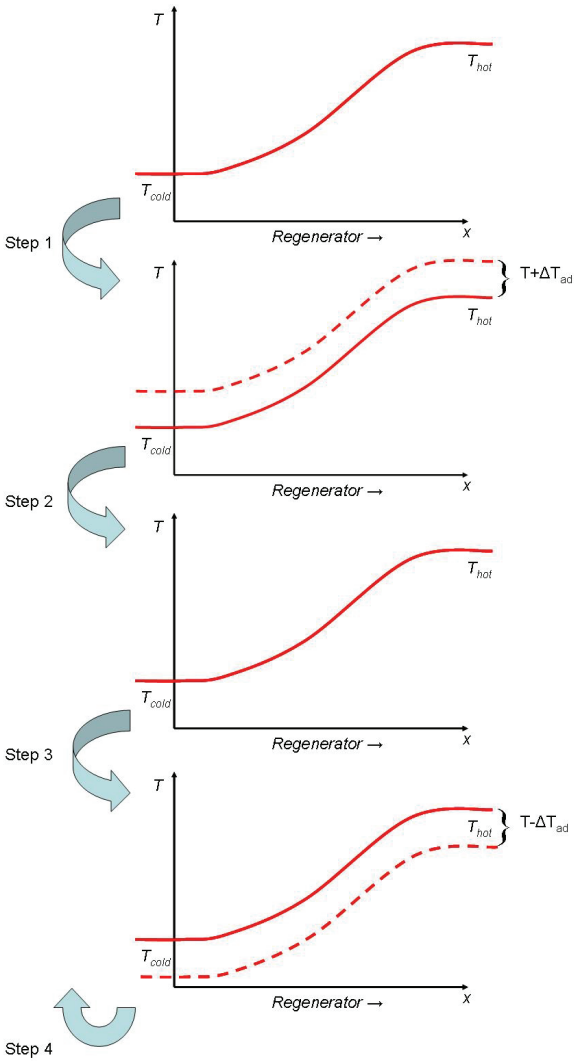

Figure 9: Temperature profile in an AMR during operation, starting from the top. The cycle starts with a temperature gradient along the regenerator. In step 1 the AMR is magnetized, the temperature in the regenerator is increased and the gradient is "lifted" upwards. In step 2 the fluid is shifted from left to right and the hot fluid is moved out to the hot reservoir where heat is rejected, resulting in a new temperature distribution. In step 3 the AMR is demagnetized shifting the gradient "downwards". Finally, in step 4 the fluid is shifted from right to left letting the cold fluid absorb heat from the cold reservoir; this returns the AMR to its original temperature distribution.

The AMR cycle cannot be illustrated by in a T-S diagram as each part of the regenerator bed executes an individual thermodynamic cycle, which is linked to each other through the heat transfer liquid. The AMR is a complex cycle, but offers the optimal utilization of the MCE.

4 Theory of the magnetocaloric effect

The magnetocaloric effect is intrinsic to all magnetic materials and is caused by changes of the entropy of the material. In general, the magnetocaloric effect itself manifests as either absorption or emission of heat when a magnetic material (e.g. iron) is placed in a magnetic field (Tishin and Spichkin 2003). This is caused by the coupling between the magnetic spin system and the thermal properties. The MCE is most easily observed as the adiabatic temperature change, ΔT_{ad}, but can also be measured indirectly as the isothermal entropy change, Δs_M. The latter is obtained when the sample is magnetized under isothermal conditions. The relationship between the two properties can be illustrated using a schematic T-S diagram (Figure 10).

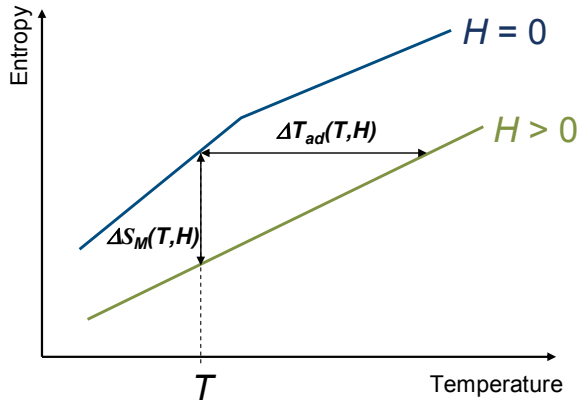

Figure 10: The adiabatic temperature change and the isothermal entropy change. The first occurs when entropy is kept constant, while the second occur when the temperature is kept constant.

If hysteresis[2] is neglected, the magnetization can be assumed reversible, i.e. the magnetic spin system returns to its initial alignment when the magnetic field is removed; this assumption is used in the remainder of the paper.

To explain the isothermal entropy change consider a magnetic sample with a given magnetic spin system under isothermal conditions. When an external magnetic field is applied, the magnetic spin system become aligned with the field, which increase the magnetic ordering and decrease the magnetic entropy (Figure 11).

[2] Hysteresis is an effect, which occurs if a ferromagnetic sample retains some remnant magnetization even when removed from the magnetic field.

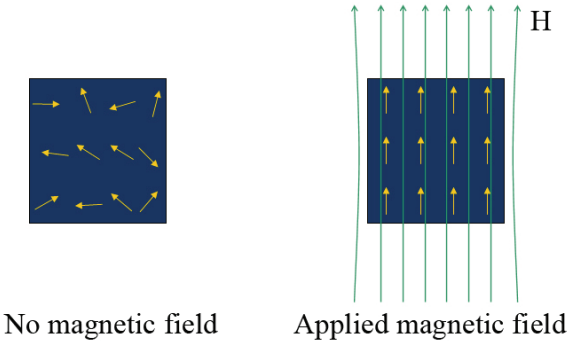

Figure 11: The ordering of the magnetic spin system of an isothermal sample before and after a magnetic field is applied. The individual magnetic moments become aligned with the external field which decreases the magnetic entropy of the sample. If the magnetic field is removed the magnetic spin system reverts to its original alignment

The adiabatic temperature change can be explained in a similar fashion. The total entropy of the sample can be split into three sources; the *magnetic entropy* from the magnetization of the material; the *lattice entropy* from the lattice vibrations of the material and the *electronic entropy* from the free electrons of the material (denoted s_m, s_l and s_e respectively) (Dinesen 2004). The lattice and the electronic entropy can be regarded as independent of the magnetic field and only depends on temperature, but the magnetic entropy is strongly dependent on both the magnetic field and the temperature. The total entropy can be written as a sum of entropy functions:

$$s_{tot}(H,T) = s_m(H,T) + s_l(T) + s_e(T) \qquad (3.1)$$

If the magnetic field is applied under adiabatic conditions, the total entropy remains constant during the magnetization process. Thus, when the magnetic entropy is decreased, the lattice and electronic entropy must increase along with the temperature to compensate. When the external field is removed, the magnetic spin system reverts to its original alignment, which decreases the thermal entropy and returns the sample to its original temperature.

4.1 Thermodynamic theory of the magnetocaloric effect

The thermodynamic system used to develop the thermodynamics of the MCE consists of a magnet and a ferromagnetic sample (Figure 12).

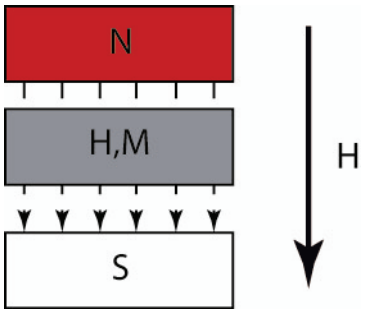

Figure 12: The thermodynamic system consists of the magnetic sample (grey area) and the magnet (read and white area), the arrow denotes the direction and strength of the magnetic field. Within the sample the total magnetic field is increased due to the magnetization of the sample.

From the 1st law of thermodynamics the change in internal energy is defined as the sum of the changes in heat and work:

$$du = dq + dw \qquad (3.2)$$

However, two different systems can be defined as either the magnet *and* the magnetic sample or the magnetic sample alone. Here only the sample is considered and the correct definition is (Adib 2002) :

$$du = Tds + \mu_0 Hd\sigma \qquad (3.3)$$

where μ_0 is the permeability of free space, H the external magnetic field and σ the specific magnetization. The infinitesimal change in internal entropy can be written in the general form:

$$ds = \left(\frac{\partial s}{\partial T}\right)_H dT + \left(\frac{\partial s}{\partial H}\right)_T dH \qquad (3.4)$$

For an isobaric process at constant magnetic field the 2nd law of thermodynamics yields the entropy dependence on temperature:

$$\left(\frac{\partial s}{\partial T}\right)_H = \frac{c_H}{T} \qquad (3.5)$$

where c_H is the total heat capacity at constant pressure and magnetic field. The entropy dependence on the magnetic field can be expressed in terms of the magnetization according to (Morrish 1965):

$$\left(\frac{\partial s}{\partial H}\right)_T = -\mu_0 \left(\frac{\partial \sigma}{\partial T}\right)_H \qquad (3.6)$$

Equation (3.5) and (3.6) are introduced into equation (3.4) to obtain an expression for the entropy:

$$ds = \frac{c_H}{T} dT + \mu_0 \left(\frac{\partial \sigma}{\partial T}\right)_H dH \qquad (3.7)$$

The total specific heat capacity at constant field can be written as:

$$c_H = \left(\frac{\partial q}{\partial T}\right)_H \qquad (3.8)$$

Using the 2nd law of thermodynamics and equation (3.8) this leads to the following relation:

$$\begin{aligned} c_H &= T\left(\frac{\partial s}{\partial T}\right)_H = T\left(\frac{\partial}{\partial T}\left(= s_m + s_l + s_e\right)\right) \\ &\Rightarrow T\left(\frac{\partial s_m}{\partial T}\right)_H + T\left(\frac{\partial s_l}{\partial T}\right)_H + T\left(\frac{\partial s_e}{\partial T}\right)_H \\ &\Rightarrow c_m + c_l + c_e \end{aligned} \qquad (3.9)$$

Thus, like the specific entropy, the specific heat capacity is also the sum of the magnetic[3], lattice and electronic contributions.

For isothermal magnetization the entropy change can be determined from equation (3.7) by setting dT equal to zero. Integrating over the change in the magnetic field results in the following expression:

$$\Delta s_M = -\mu_0 \int_{H1}^{H_2} \left(\frac{\partial \sigma}{\partial T}\right)_H dH \qquad (3.10)$$

For a ferromagnetic material the magnetization decreases with temperature and $(\partial\sigma/\partial T)$ is negative, which means that an increased magnetic field reduces the entropy as expected.

The adiabatic temperature change can be determined from equation (3.7) by setting ds to zero and integrating over the change in the magnetic field.

$$\Delta T_{ad} = -\mu_0 \int_{H1}^{H_2} \frac{T}{c_H} \left(\frac{\partial \sigma}{\partial T}\right)_H dH \qquad (3.11)$$

The adiabatic temperature change is directly proportional to the temperature and inversely proportional to the heat capacity. Since $(\partial\sigma/\partial T)$ is negative, an increase in the magnetic field results in a positive adiabatic temperature change as both the temperature and heat capacity are positive, again as expected.

From equation (3.10) and (3.11) it can be concluded that the MCE will be large if:

- The magnetic field change is large

[3] The subscript, *m*, denotes that c_m is the magnetic contribution to the total heat capacity. This should not be confused with the total heat capacity at constant magnetization.

- The magnetization changes rapidly with temperature (i.e. $|\partial\sigma/\partial T|$ is large)
- The heat capacity is small

From the second point one can expect a large MCE near the Curie temperature of ferromagnetic materials, where the material changes phase from an ordered ferromagnetic spin system to a random paramagnetic spin system. This transition is associated with a large reduction of magnetization, and thus a large MCE (Figure 13).

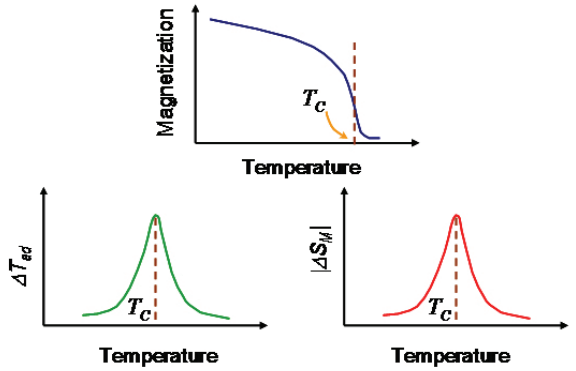

Figure 13: The relationship between the temperature dependence of the magnetization and the magnetocaloric effect. The magnetocaloric effect is largest around the Curie temperature where the material experiences a phase transition. The adiabatic temperature change will have a positive peak and the isothermal entropy change will have a negative peak.

4.2 Materials for magnetic refrigeration

For a material to be suitable for magnetic refrigeration it must have a Curie temperature in the vicinity of the temperature regime where the refrigerator will operate. Furthermore, for magnetic refrigeration system commercially usable the material must be chemically stable to avoid corrosion and be "cheap enough".

The magnitude of the MCE in real materials has not yet been discussed, i.e. how large a temperature difference is it possible to achieve in different magnetic fields. The "prototype" material is gadolinium, which has been used since the 1970s. The adiabatic temperature change for gadolinium in different magnetic fields is shown as an example (Figure 14).

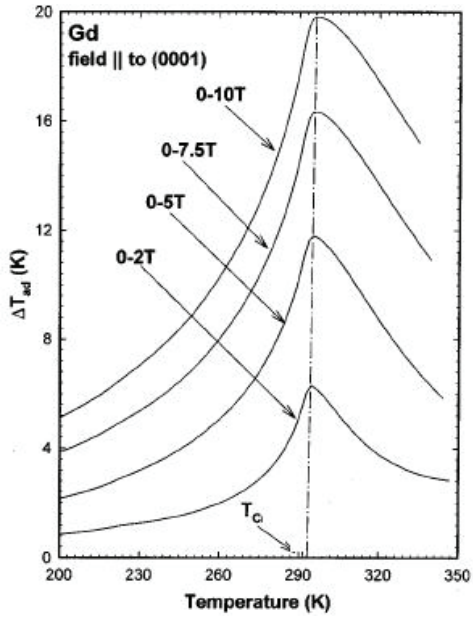

Figure 14: The adiabatic temperature change in gadolinium as a function of temperature in magnetic fields ranging from 2 to 10 T. Magnetic fields above approximately. 2 T can only be achieved from superconducting magnets (Tishin et al. 1999)

The figure reveals one of the greatest problems when using the MCE for refrigeration; the obtainable temperature difference is small. It is only around 20 K even in a magnetic field of 10 T, which can only be obtained using superconducting magnets. For permanent magnets it is only possible to obtain magnetic field changes of approximately 2 T, the temperature difference is approx. 6 K. This is one of the primary reasons for the need for regeneration in magnetic refrigeration; the MCE cannot directly obtain the temperature span needed for conventional household refrigeration.

Finally, it should be mentioned that is possible to model the magnetocaloric effect using a phenomenological model of magnetism as the one presented in (Dinesen 2004). The model may be used with the equations presented in this paper for basic investigations of the MCE and magnetic refrigeration cycles.

5 Conclusion and outlook

Magnetic refrigeration offers a more energy effective alternative to vapour-compression based refrigeration. This is because magnetic refrigeration uses the magnetocaloric effect, a virtually reversible thermodynamic process, which occurs when a magnetic material is placed

in a magnetic field. However, it is not possible to use the magnetocaloric effect directly for refrigeration. Specialized refrigeration cycles with regeneration are required for magnetic refrigeration to be used for conventional refrigeration. Experimental refrigerators have been constructed to demonstrate the concept.

Risø National Laboratory has investigated the magnetocaloric effect in ceramics since 2001, and the results are promising. The research activities have recently been extended into two new areas: Risø has constructed a proof-of-concept magnetic refrigerator to test the ceramics suitability for magnetic refrigeration and a detailed finite element model was developed to optimize the design of the magnetic refrigerator. Publications on these new research areas are forthcoming.

It is the aim of Risø that the old and new research areas complement each other and produce knowledge and patents which help magnetic refrigeration become commercial.

6 Nomenclature

Symbol	Unit
c_H	$Jkg^{-1}K^{-1}$
c_m	$Jkg^{-1}K^{-1}$
c_l	$Jkg^{-1}K^{-1}$
c_e	$Jkg^{-1}K^{-1}$
H	Am^{-1}
μ_0	NA^{-2}
q	W
T	K
T_C	K
ΔT_{ad}	K
σ	Am^{-1}
Δs_m	$JK^{-1}kg^{-1}$
s	$JK^{-1}kg^{-1}$
s_m	$JK^{-1}kg^{-1}$
s_l	$JK^{-1}kg^{-1}$
s_e	$JK^{-1}kg^{-1}$

7 Acknowledgements

The authors would like to thank Louise Theil Kuhn, and Frank Petersen for proof-reading the manuscript, Kristian Nim Sørensen for technical support during construction of the AMR and Toke Henriksen for LabView support for the AMR control and data acquisition software.

8 References

Adib, A. B. (2002). "Free energies for magnetic systems.".

Brown, G. V. (1976). "Magnetic heat pumping near room temperature." *Journal of Alloys and Compounds*, 47(8), 3673-3680.

Dinesen, A. R., Linderoth, S., and Morup, S. (2005). "Direct and indirect measurement of the magnetocaloric effect in La0.67Ca0.33-xSrxMnO3 +/-delta (x is an element of [0; 0.33])." *Journal of Physics-Condensed Matter*, 17(39), 6257-6269.

Dinesen, A. R. (2004). "Magnetocaloric and magnetoresistive properties of La0.67Ca0.33-xSrxMnO3." Risø National Laboratory, August 2004, 103 p., ISBN 87-550-3224-9.

Kitanovski, A., and Egolf, P. W. (2005). "Thermodynamics of magnetic refrigeration." *International journal of refrigeration*, 29(3-12), 3-21.

Morrish, A. H. (1965). *The Physical Principles of Magnetism*., John Wiley & Sons, Inc..

Nellis, G., Engelbrecht, K., Klein, S., Zimm, C., and Russek, S.(2004). "Model and Evaluation Tools for Assessing Magnetocaloric Effect for Space Conditioning and Refrigeration Applications.".

Tishin, A. M., Gschneidner, K. A., and Pecharsky, V. K. (1999). "Magnetocaloric effect and heat capacity in the phase-transition region." *Physical Review B*, 59(1), 503-511.

Tishin, A., and Spichkin, Y. (2003). *The Magnetocaloric Effect and its Applications*., Institute of Physics Publishing.

APPENDIX E

US Patent Application US61/078886 and UK Patent Application 0815447.8

Paper IV

Magnetocaloric Refrigerators
Jeppesen, S., Linderoth, S. and Vang Hendriksen, P.

Magnetocaloric Refrigerators

The present invention relates to the production of magnetocaloric refrigerators, i.e. refrigerators operating by magnetic refrigeration.

Most of refrigeration technologies for use in the near room temperature region such as refrigerators, freezers, and air-conditioners use a gas compression cycle and suffer from the disadvantage of using potentially environmentally damaging fluid refrigerants.

Magnetic refrigeration technologies use the magnetocaloric effect of magnetic materials in a refrigeration cycle instead of a gas compression cycle. Specifically, the refrigeration cycle is realized by using a magnetic entropy change of the magnetic material associated with a magnetic phase transition (phase transition between a paramagnetic state and a ferromagnetic state). In order to obtain highly efficient magnetic refrigeration, it is crucial to use a magnetic material which exhibits a high magnetocaloric effect around the temperature of operation, possibly in conjunction with other magnetocaloric materials exhibiting such an effect at selected adjacent temperatures.

The magnetocaloric effect has been studied in several lanthanum containing materials. These include manganite perovskite type materials and $NaZn_{13}$-type structure materials. In some cases the effect of substituting another lanthanide element for part of the lanthanum has been investigated (US2006/0231163; CN1170749; Chen et al, Journal of Magnetism and Magnetic Materials, 257 (2003), 254-257; Wang et al, Journal of Applied Physics, Vol 90, No. 11, 1 Dec 2001)). The specific materials for which data is presented contain lanthanum plus just one other lanthanide.

The lanthanum containing refrigerant materials are produced from raw materials comprising highly purified lanthanum or lanthanum

sources such as oxides or nitrates and if desired another pure lanthanide.

We have now appreciated that satisfactory magnetocaloric refrigerant materials containing lanthanum can be produced using 'lanthanum concentrate', a commercially available mixed oxide containing lanthanum, cerium, praseodymium and neodymium as lanthanide components. This avoids the need to refine the original lanthanide bearing raw materials into separate pure lanthanides or reduces the necessary extent of the use of highly refined material where relative proportions of these lanthanides differing from those in lanthanide concentrate is desired. An alternative mixed lanthanide source that may be used in at least some instances is the lanthanum-rich mischmetal.

Thus, the present invention provides in a first aspect the use in the construction or operation of a magnetocaloric refrigerator of a La containing magnetocaloric refrigerant also containing Ce, Pr and Nd. In a further aspect it provides a method of making a magnetocaloric refrigerator comprising preparing a magnetocaloric refrigerant material from starting materials which include lanthanum concentrate or a La-rich mischmetal and incorporating said magnetocaloric refrigerant material into a magnetocaloric refrigerator as the working refrigerant thereof. The invention includes in a further aspect a magnetocaloric refrigerator having as a working refrigerant a La containing magnetocaloric refrigerant material also containing Ce, Pr and Nd.

Lanthanide concentrate is obtainable from for instance Molycorp, Inc. Mountain Pass Calif. as product entitled 'Code 5210 Lanthanum Concentrate'. The other large source of rare earths in the world is the Baotou Ore in Baotou, Inner Mongolia, where La is like in the Mountain Pass ore refined from bastnaesite.

Whilst the exact composition of lanthanide concentrate may vary somewhat between suppliers, it is an intermediate product produced during the purification of lanthanides from lanthanide ores. It

generally contains La_2O_3, CeO_2, Pr_6O_{11} and Nd_2O_3 in weight proportions on an oxide basis 100 La_2O_3: 5-30 CeO_2: 5-20 Pr_6O_{11}: 20-40 Nd_2O_3 or more commonly 100 La_2O_3: 10-21 CeO_2: 12-14 Pr_6O_{11}: 28-34 Nd_2O_3.

The use of lanthanum concentrate necessarily brings with it not only lanthanum but also each of the three other named lanthanides. However, the elements do not have to be in the above proportions in the magnetocaloric refrigerant, as additional purified lanthanide oxides can be added in the manufacture of the product so as to increase the proportion of any of the four lanthanides or to provide one or more further lanthanide elements.

Preferably, the lanthanum content of the refrigerant derives from a mixture of lanthanum concentrate and a more pure source of lanthanum.

An alternative mixed lanthanide source for use in the invention is a mischmetal. These materials which are again commercially available from Tianjiao International Co. 'Code 9003 La Rich Mischmetal'. La-rich mischmetal typically contain:

La wt 58-65%

Ce wt 2-29%

Pr wt 3-35%

Nd wt 2-8%

A typical example is 61 wt% La, 2 wt% Ce, 35 wt% Pr, and 2 wt% Nd. In these materials the lanthanides are present as elemental metal rather than as oxides. This is convenient for making some of the materials described below.

The magnetocaloric refrigerant may be of the manganite perovskite type, in which case preferably, the refrigerant is of the general formula:

$$La_l\ Ce_c\ Pr_p\ Nd_n\ RE_r\ A_a\ MnX_xO_{3-\delta}$$

wherein:

A is at least one of the alkaline earth metals

X if present is at least one metal selected from the group consisting of Co, Mn, Fe, Ni, Zn, Cu, Al, V, Ir, Mo, W, Pd, Pt, Mg, Ru, Rh, Cr and Zr.

RE, if present, is at least one lanthanide other than La, Ce, Pr and Nd,

the ratio of (l + c + p + n + r + a):(1 + x) is from about 1:0.95 to about 1:1.15,

the ratio of (l + c + p + n + r):(a) is from about 5:4 to about 7:2,

x is from 0 to about 0.15, and

$-1<\delta<1$.

Preferred alkaline earth metals are magnesium, calcium, strontium and barium.

Preferably, l:(c + p + n + r) < 10, more preferably < 5, still more preferably < 3. For instance, l:(c + p + n + r) may be from 10 to 1, more preferably from 5 to 1.25, still more preferably from 2.5 to 1.7, e.g. about 2.

Preferably, l:c < 100 and more preferably l:c < 50, and still more preferably < 33 and still more preferably < 25 and still more preferably < 20.

Preferably, l:p <100 and more preferably l:p < 50, and still more preferably < 33 and still more preferably < 25 and still more preferably < 20.

Preferably, l:n <50 and more preferably l:n < 17, and still more preferably < 10 and still more preferably < 7 and still more preferably < 5.

Preferred compositions include:

$La_{0.40-0.48}Ce_{0.01-0.05}Pr_{0.02-0.08}Nd_{0.11-0.19}Ca_{0.30-0.36}Mn_{0.95-1.05}O_{3+delta}$, and

$(La_{0.44}Ce_{0.03}Pr_{0.05}Nd_{0.15})_{1-x}\ La_x\ Ca_{0.33}Mn_{1.05}O_3$, $x=[0:0.8]$

Preferably, the total lanthanide sums to from 0.63 to 0.71, more preferably from 0.64 to 0.70, and most preferably to 0.66-0.68.

One preferred material is of the formula:

$La_{0.44}Ce_{0.03}Pr_{0.05}Nd_{0.15}Ca_{0.33}Mn_{1.05}O_3$

The specific content of the various lanthanides may be chosen to provide suitability for use as a refrigerant in a respective temperature range.

For instance, materials of the formula $La_{0.40-0.48}Ce_{0.01-0.05}Pr_{0.02-0.08}Nd_{0.11-0.19}Ca_{0.30-0.36}Mn_{0.95-1.05}O_{3+delta}$ may be used as refrigerant in the temperature interval -100 °C to -70 °C.

Materials of the formula $La_{0.6-0.65}Ce_{0.006-0.03}Pr_{0.01-0.05}Nd_{0.07-0.13}Ca_{0.30-0.36}Mn_{0.95-1.05}O_{3+delta}$ may be used as refrigerant in the temperature interval -80 °C to -50 °C.

Materials of the formula $La_{0.75-0.78}Ce_{0.002-0.02}Pr_{0.004-0.02}Nd_{0.02-0.04}Ca_{0.30-0.36}Mn_{0.95-1.05}O_{3+delta}$ may be used as refrigerant in the temperature interval -50 °C to -20 °C.

The magnetocaloric refrigerant may be of the $NaZn_{13}$-type crystal structure, in which case it preferably is of the general formula:

$La_l,\ Ce_c,\ Pr_p,\ Nd_n,\ RE_r,\ (Fe_{1-d-e}\ D_d\ E_e)_{13}\ G_g$

wherein:

RE if present is at least one lanthanide other than La, Ce, Pr and Nd.

D if present is at least one element selected from the group consisting of Co, Ni, Zn, Cu, Mn, Al, V, Ir, Mo, W, Pd, Pt, Mg, Ru, Rh, Cr and Zr.

E if present is at least one element from the group (B, Al, Ga, In, Tl, C, Si, Ge, Sn, Pb),.

G is at least one selected from the group (C, H, B).

The ratio of (l' + c' + p' + n' + r'):1 is from about 1:12 to about 1:14, the ratio of l': (c' + p' + n') is from about 10:1 to about 1:1, more preferably from 5:1 to 2:1,

d is from 0 to about 0.2,

e is from 0 to about 0.2,

g is from 0 to 2, more preferably in the range 0.5-1.6.

Regarding E, it is preferred that this is Si, Co, Al, Mn, Cr, or Ni.

Regarding G, this is preferably H, but may be B or C, although carbon tends to lower the effective entropy change.

The use of La-rich mischmetal is more conveniently applied to this type of magnetocaloric material as in making this type of material it would normally be necessary to reduce an oxide starting material to the pure element.

The materials described as cell materials for use in solid oxide fuel cells in US 5,759,936 can be used as the magnetic refrigerant according to the present invention.

In an alternative aspect the invention includes the use in the construction or operation of a magnetocaloric refrigerator of a La containing magnetocaloric refrigerant also containing Ce, Pr and Nd which may be any of the magnetocaloric refrigerant materials as described above.

The invention further includes a method of making a magnetocaloric refrigerator having a working refrigerant, comprising preparing a magnetocaloric refrigerant material from starting materials which include lanthanum concentrate or a lanthanum-rich mischmetal and incorporating said magnetocaloric refrigerant material into a magnetocaloric refrigerator as the working refrigerant thereof.

A refrigerator in accordance with the invention may further comprise a source of magnetic field operable to increase and then decrease (optionally to zero) repeatedly a said magnetic field applied to said working refrigerant.

The refrigerator may further comprise a hot side heat exchanger and a cold side heat exchanger and a heat transfer fluid contained in a flow path for said heat transfer fluid connecting said hot side heat exchanger and said cold side heat exchanger via a location in which said heat transfer fluid is in heat exchange relationship with said working refrigerant.

The refrigerator may further comprise a pump mechanism connected to pump said heat transfer fluid from said location to said hot side heat exchanger after application of said magnetic field to said working refrigerant and to return said working fluid to said location and then to said cold side heat exchanger after reduction of said magnetic field applied to said working refrigerant.

The invention will be further described and illustrated with reference to the accompanying drawings in which:

Figure 1 shows a schematic representation of an example of a magnetic refrigerator according to the invention; and

Figure 2 shows a plot of the Curie temperature of a range of magnetocaloric materials of the general formula:

$La_{(1-x)}Ln_xCa_{0.33}Mn_{1.05}O_3$,x=[0,0.33,0.66,1] where Ln = $La_{0.44}Ce_{0.03}Pr_{0.05}Nd_{0.15}$

The materials described herein may be used in essentially any form of magnetic refrigerator. This includes use in a magnetic refrigerator generally as described in WO2006/74790. As described there, the active component of a magnetic refrigerator, referred to as a magnetic regenerator, is formed of a magnetocaloric material, i.e. a material that heats up when placed in an applied magnetic field and cools when the field is removed. Such materials have been known for a long time and it has been recognised that they could be used for cooling purposes. Specifically, a typical active magnetic refrigerator comprises a magnetic regenerator arranged between a hot-side heat exchanger and a cold-side heat exchanger. A source of magnetic field is also provided. A heat transfer fluid is arranged to flow back and forth from the cold-side heat exchanger towards the hot-side heat exchanger through the magnetic regenerator in a cycle. A magnetic field is repeatedly applied to and removed from the magnetic regenerator, thereby causing it to heat up and cool down.

There are four stages to an active magnetic regenerator cycle. First, the application of a magnetic field warms the magnetic regenerator by the magnetocaloric effect, causing the heat transfer fluid within the regenerator to heat up. Second, heat transfer fluid flows in the direction from the cold-side heat exchanger to the hot-side heat exchanger. Heat is then released from the heat transfer fluid to the hot-side heat exchanger. Third, the magnetic regenerator is demagnetised, cooling the magnetocaloric material and the heat transfer fluid in the bed. Last, the heat transfer fluid flows through the cooled bed in the direction from the hot-side heat exchanger to the cold-side heat exchanger. The fluid takes up heat from the cold-side heat exchanger. The cold-side heat exchanger can then be used to provide cooling to another body or system.

Figure 1 shows a schematic representation of an example of a magnetic refrigerator according to an embodiment of the present invention. The refrigerator comprises a magnetocaloric unit (4) arranged in thermal communication with each of a cold-side heat exchanger (6) and

a hot-side heat exchanger (8). A heat transfer fluid (10) is provided for being forced back and forth through the magnetocaloric unit (4). In the example shown pistons (12) and (14) are provided for forcing the heat transfer fluid (10) through the magnetocaloric unit (4).

A magnet (not shown) is also provided for selectively applying a magnetic field to the magnetocaloric unit (4) and removing the magnetic field. The magnet may be a permanent magnet or an array of such magnets, an electromagnet or a solenoid. For low temperature applications the solenoid may be formed of superconductive material and be cooled by a cryogenic liquid such as liquid nitrogen.

In the specific example shown, a vertical section through the magnetocaloric unit is shown. The magnetocaloric unit (4) comprises plates (16) defining therebetween passages or paths (18) along which the heat transfer fluid flows.

In the embodiment shown, the magnetocaloric material used is graduated in composition across the magnetocaloric unit by variation of the chemical composition to alter the Curie temperature thereof. Decreasing the La content with respect to the other or total lanthanides produces a decreasing Curie temperature as shown in Figure 2. Alternatively, the Curie temperature can be adjusted by varying the alkaline earth metal (e.g. Ca) content or by the extent of replacement of Mn by the element X in the manganite system or equally changing the Curie temperature in the $NaZn_{13}$-type crystal structure system by varying d, e, or g.

This is illustrated in Figure 1 by a graph of the variation of temperature of the magnetocaloric unit in the direction x, from the cold-side heat exchanger to the hot-side heat exchanger. A temperature gradient is established between the cold-side heat exchanger (6) and the hot-side heat exchanger (8). The temperature T(x) at any position x varies between temperatures T_{cold} and T_{hot}. In view of the recognised fact that the magnetocaloric effect of a

material varies with temperature and is at a maximum at or near the magnetic transition temperature of the material, the plates are formed such that the magnetic transition temperature of the plates (16) within the magnetocaloric unit (4) varies in the direction between the cold-side heat exchanger (6) and the hot-side heat exchanger (8).

To optimise the performance of the refrigerator, the material used in the form of the magnetocaloric unit (4) is selected so that at the position x_0, the unit (4) has a maximum magnetocaloric effect at temperature T_0. This ensures that the maximum possible magnetocaloric effect is achieved by the device. As will be explained below, this may be achieved by controlling and/or varying the composition of the material or powder used to form the unit (4).

The material or materials used to form the plates (16) of the magnetocaloric unit (4) in the example shown in Figure 1 may be non-corroding materials, i.e. they are materials that substantially do not corrode upon exposure to a liquid such as a heat transfer fluid. The use of ceramic materials is particularly preferred due to its chemical stability towards corrosion.

In an example, two or more systems such as the one shown in Figure 1 are arranged either in parallel or series. A moveable permanent magnet is provided enabling the magnet to be utilised continuously. When one regenerator is demagnetised the magnet can be used to magnetise one of the others.

In use, initially, the magnetocaloric unit (4) is demagnetised. Upon application of a magnetic field, the temperature of the magnetocaloric unit(4)rises due to a decrease in magnetic entropy and a corresponding increase in thermal entropy of the magnetic regenerator. Heat transfer fluid within the magnetocaloric unit increases in temperature with the magnetocaloric unit (4). The pistons (12) and (14) are then actuated to move to the right thereby forcing heat transfer fluid (10) to the left of the magnetocaloric unit into the spaces between the plates (16) and the heat transfer

fluid that is within the magnetocaloric unit and therefore heated due to the rise in temperature of the magnetocaloric unit towards the hot-side exchanger (8).

In other words, the heat transfer fluid that is initially within the magnetic regenerator and is heated upon application of the magnetic field is forced towards the hot-side heat exchanger where it gives up some of the heat it has gained as a result of the application of the magnetic field.

The magnetic field is then removed, e.g., by the switching off of the magnetic field. This causes an increase in magnetic entropy and a corresponding decrease in thermal entropy. The magnetocaloric unit(4)thereby reduces in temperature. The heat transfer fluid within the magnetocaloric unit(4)at this stage undergoes a similar temperature drop due to the drop in temperature of the magnetocaloric unit (4). As the pistons move towards the left (in Figure 1) this cooled heat transfer fluid is then forced, by the pistons (12) and (14), towards the left hand side of the refrigerator (the actual configuration shown in Figure 1) and the cold-side heat exchanger (6) where it can receive heat, e.g. from an article being cooled. The cycle can then be repeated.

If a single magnetocaloric material is used, its operating range is likely to be narrow. This can be circumvented by using a series of materials each tuned to have optimum properties in a given temperature interval. The materials of the present invention have tunable magnetocaloric properties, where the substitution of La with cheaper materials not only leads to better commercial performance but also leads to better technical performance by the ability to design the magnetocaloric refrigerant material to perform in a certain working temperature range. Thus, changing the chemical composition makes it possible to control a variety of technologically important properties such as the magnitude of the magnetocaloric effect (MCE) and the usable temperature range as refrigerant i.e. the ferro- to paramagnetic transition temperature. By substituting some of the

lanthanum in the composition with the less expensive lanthanum concentrate the price is lowered, and furthermore the technical performance of the material is improved.

The following examples illustrate materials suitable for use in a refrigerator according to the invention.

EXAMPLE 1

Commercial Lanthanum-rich mischmetal containing 61 wt% La, 2 wt% Ce, 35 wt% Pr, and 2 wt% Nd is mixed with pure powders of Fe, Si in quantities according to the chemical formula:

$$La_{0.44}Ce_{0.03}Pr_{0.05}Nd_{0.15}\left(Fe_{0.88}Si_{0.12}\right)_{13}H_{1.6}$$

The resulting powder is placed in an evacuated container and afterwards heat treated for several days in a hydrogen atmosphere to obtain a hydrogenated single phase $NaZn_{13}$-type crystal structure.

Co can be substituted for Fe in amounts of a few to 15% of the Fe in order to tune the Curie temperature. An example of the composition could be:

$$La_{0.44}Ce_{0.03}Pr_{0.05}Nd_{0.15}\left(Fe_{0.80}Si_{0.12}Co_{0.08}\right)_{13}H_{1.6}$$

Example 2

Commercial Lanthanum Concentrate containing 40% La_2O_3, 4% CeO_2, 5.5% Pr_6O_{11} and 13,5% Nd_2O_3 plus 1% other lanthanides is dissolved in 65% HNO_3. This solution is mixed with solutions of $Ca(NO_3)_2$, $Sr(NO_3)_2$ and $Mn(NO_3)_2$ in quantities according to the chemical formula:

$$La_{0.44}Ce_{0.03}Pr_{0.05}Nd_{0.15}Ca_{0.33}Mn_{1.05}O_3$$

The resulting mixed salt solution is added glycine in order to obtain a glycine/nitrate ratio of approximately 0.6. The solution is boiled down to remove excess water. Finally the viscous solution starts to form a foam before it self-ignites making a ceramic powder. The powder is afterwards heat treated to obtain single phase perovskite. The powder can be used as refrigerant by sintering into different shapes obtained by pressing, tapecasting, rolling etc. for the appropriate shape.

In this specification, unless expressly otherwise indicated, the word 'or' is used in the sense of an operator that returns a true value when either or both of the stated conditions is met, as opposed to the operator 'exclusive or' which requires that only one of the conditions is met. The word 'comprising' is used in the sense of 'including' rather than in to mean 'consisting of'. All prior teachings acknowledged above are hereby incorporated by reference. No acknowledgement of any prior published document herein should be taken to be an admission or representation that the teaching thereof was common general knowledge in Australia or elsewhere at the date hereof.

CLAIMS

1. A magnetocaloric refrigerator having as a working refrigerant an La containing magnetocaloric refrigerant material also containing Ce, Pr and Nd.

2. A refrigerator as claimed in claim 1, further comprising a source of magnetic field operable to increase and then decrease repeatedly a said magnetic field applied to said working refrigerant.

3. A refrigerator as claimed in claim 2, further comprising a hot side heat exchanger and a cold side heat exchanger and a heat transfer fluid contained in a flow path for said heat transfer fluid connecting said hot side heat exchanger and said cold side heat exchanger via a location in which said heat transfer fluid is in heat exchange relationship with said working refrigerant.

4. A refrigerator as claimed in claim 3, further comprising a pump connected to pump said heat transfer fluid from said location to said hot side heat exchanger after application of said magnetic field to said working refrigerant and to return said working fluid to said location and then to said cold side heat exchanger after reduction of said magnetic field applied to said working refrigerant.

5. A refrigerator as claimed in claim 1, wherein said magnetocaloric refrigerant material is of the general formula:

$$La_l\ Ce_c\ Pr_p\ Nd_n\ RE_r\ A_a\ MnX_xO_{3-\delta}$$

wherein:

A is at least one of the alkaline earth metals
X if present is at least one metal selected from the group consisting of Co, Mn, Fe, Ni, Zn, Cu, Al, V, Ir, Mo, W, Pd, Pt, Mg, Ru, Rh, Cr and Zr,
RE if present is at least one lanthanide other than La, Ce, Pr and Nd,
the ratio of (1 + c + p + n + r + a):(1 + x) is from about 1:0.95 to about 1:1.15,
the ratio of (1 + c + p + n + r):(a) is from about 5:4 to about 7:2,
x is from 0 to about 1:0.15, and
$-1<\delta<1$.

6. A refrigerator as claimed in claim 5, wherein 1:(c + p + n + r) < 1:0.1.

7. A refrigerator as claimed in claim 6, wherein 1:(c + p + n + r) < 1:0.2.

8. A refrigerator as claimed in claim 7, wherein 1:(c + p + n + r) < 1:0.3.

9. A refrigerator as claimed in claim 5, wherein 1:(c + p + n + r) is from 1:0.1 to 1:1.

10. A refrigerator as claimed in claim 9, wherein 1:(c + p + n + r) is from 1:0.2 to 1:0.8.

11. A refrigerator as claimed in claim 10, wherein 1:(c + p + n + r) is from 1:0.4 to 1:0.6.

12. A refrigerator as claimed in claim 5, wherein said magnetocaloric material is of the general formula:

$La_{0.40-0.48}Ce_{0.01-0.05}Pr_{0.02-0.08}Nd_{0.11-0.19}Ca_{0.30-0.36}Mn_{0.95-1.05}O_{3+delta}$, wherein the total lanthanide sums to from 0.63 to 0.71.

13. A refrigerator as claimed in claim 1, wherein said magnetocaloric material is of the general formula:
$La_{l'}\ Ce_{c'}\ Pr_{p'}\ Nd_{n'}\ RE_{r'}\ (Fe_{1-d-e}\ D_d\ E_e)_{13}\ G_g$

wherein:
RE is at least one of the rare earth elements,
D if present is at least one metal selected from the group consisting of Co, Ni, Zn, Cu, Mn, Al, V, Ir, Mo, W, Pd, Pt, Mg, Ru, Rh, Cr and Zr,
E if present is at least one element from the group (B, Al, Ga, In, Tl, C, Si, Ge, Sn, Pb),
G is at least one selected from the group of C, H, B,
the ratio of (l' + c' + p' + n' + r'):1 is from about 1:12 to about 1:14,
the ratio of l': (c' + p' + n') is from about 10:1 to about 1:1, more preferably from 5:1 to 2:1,
d is is from 0 to about 0.2,
e is from 0 to about 0.2, and
g is from 0 to 2, more preferably in the range 0.5-1.6

14. A refrigerator as claimed in claim 13, wherein l': (c' + p' + n') is from 5:1 to 2:1.

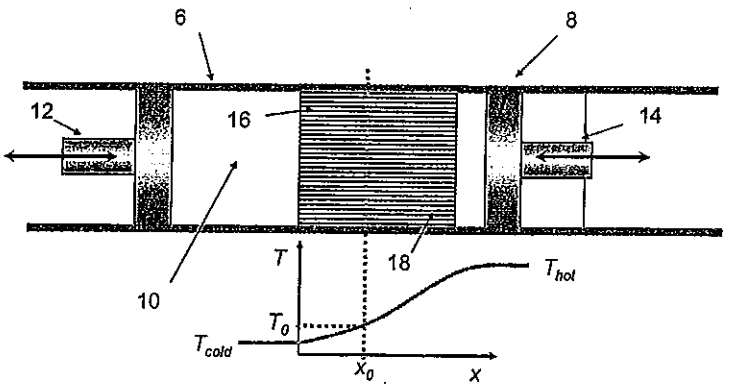

Figure 1

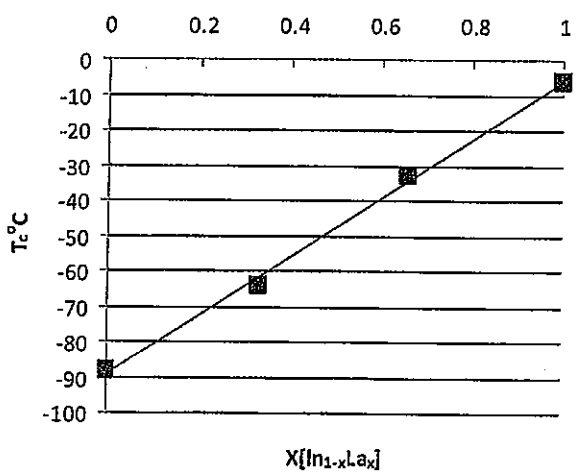

Figure 2

APPENDIX F

Paper in preparation.

Paper V

Effect of low level Cu-doping on the magnetocaloric properties of $La_{0.66}Ca_{0.33}$-$Mn_{1.05}0_3$

S. Jeppesen , S. Linderoth, N. Pryds and C.R.H. Bahl

Abstract:
An enhancement of the magnetocaloric effect (MCE) caused by Cu doping of the Mn-site has been found in single phased, polycrystalline samples of the over-stoichiometric $La_{0.66}Ca_{0.33}Mn_{1.05}0_3$ perovskite system. The MCE can be enhanced to an optimum around 3% Cu doping for the investigated compounds. Furthermore, low level Cu doping could be used to tune the working range of the material as magnetic refrigerant, without deteriorating the MCE. The Cu ions are believed to be soluble in small amounts below 3%, where the Cu ions are diluting the magnetic interaction confirmed by a decreasing Curie transition and decreasing saturation magnetization, but enhancing the quality of the transition, which then leads to an increased entropy change.

Bibliography

[1] E. Warburg. Magnetische Untersuchungen. *Ann.Phys.(Leipzig)*, 13:141–164, 1881.

[2] P. Weiss and A. Piccard. A new thermomagnetic phenomenon. *Comptes Rendus Hebdomadaires des Seances de l'Academie des Sciences*, 166:352–354, 1918.

[3] W.F. Giauque. A thermodynamic treatment of certain magnetic effects. A proposed. *Journal of the American Chemical Society*, 49:1864–1870, 1927.

[4] P. Debye. Magnetisation at low temperatures. *Annalen der Physik*, 81:1154–1160, 1926.

[5] W.F. Giauque and D.P. MacDougall. Production of temperatures below 1 degrees K by adiabatic demagnetisation. *Journal of the American Chemical Society*, 57:1175–1185, 1935.

[6] G.V. Brown. Magnetic heat pumping near room temperature. *Journal of Alloys and Compounds*, 47(8):3673–3680, 1976.

[7] K. Nielsen, H. Nielsen, and H. Siggard Jensen. *Skruen uden ende - Den vestlige teknologis historie*. Ingenioren Boger, 2nd edition, 2004.

[8] C. Bahl. Personal communication. 2008.

[9] K.A. Gschneidner and V.K. Pecharsky. Thirty years of near room temperature magnetic cooling. *International Journal of Refrigeration*, 31:945–961, 2008.

[10] K.A. Gschneidner, V.K. Pecharsky, and A.O. Tsokol. Recent developments in magnetocaloric materials. *Reports on Progress in Physics*, 68(6):1479–1539, 2005.

[11] B.F. Yu, Q. Gao, B. Zhang, X.Z. Meng, and Z. Chen. Review on research of room temperature magnetic refrigeration. *International Journal of Refrigeration-Revue Internationale du Froid*, 26(6):622–636, 2003.

[12] E. Bruck. Developments in magnetocaloric refrigeration. *Journal of Physics D-Applied Physics*, 38(23):R381–R391, 2005.

[13] A.M. Tishin and Y.I. Spichkin. *The Magnetocaloric Effect and its Applications*. Institute of Physics Publishing, Temple Back, Bristol, UK, 2003.

[14] A. Kitanovski and P.W. Egolf. Thermodynamics of magnetic refrigeration. *International Journal of Refrigeration*, 29:3–21, 2006.

[15] N. A. Oliveira. Magnetocaloric effect under applied pressure and the barocaloric. *Journal of Physics: Condensed Matter*, 20:175209, 2008.

[16] A.H. Morrish. *The Physical Principles of Magnetism*. John Wiley & Sons, Inc., 1965.

[17] V.K. Pecharsky and K.A. Gschneidner. Magnetocaloric effect from indirect measurements: Magnetization and. *Journal of Applied Physics*, 86(1):565–575, 1999.

[18] V. Basso, M. Kuepferling, C.P. Sasso, and L. Giudici. A Peltier cell calorimeter for the direct measurement of the isothermal. *Review of Scientific Instruments*, 79:063907, 2008.

[19] T. Plackowski, Y. Wang, and A. Junod. Specific heat and magnetocaloric effect measurements using commercial. *Review of Scientific Instruments*, 73(7):2755–2765, 2002.

[20] J. Marcos, F. Casanova, X. Batlle, A. Labarta, A. Planes, and L. Manosa. A high-sensitivity differential scanning calorimeter with magnetic. *Review of Scientific Instruments*, 74:4768, 2003.

[21] V.K. Pecharsky, J.O. Moorman, and K.A. Gschneidner. A 3-350 K Fast Automatic Small Sample Calorimeter. *Rev.Sci.Instr.*, 68(11):4196–4207, 1997.

[22] J.H. Van Santen and G.H. Jonker. Electrical conductivity of ferromagnetic compounds of manganese with. *Physica*, 16:599–600, 1950.

[23] C. Zener. Interaction between the d-Shells in the Transition Metals. II. Ferromagnetic. *Physical Review*, 82:403–405, 1951.

[24] J. Volger. Further Experimental Investigations on Some Ferromagnetic Oxidic. *Physica*, 20:49–66, 1954.

[25] S. Jin, T.H. Tiefel, M. McCormack, R.A. Fastnacht, R. Ramesh, and L.H. Chen. Thousandfold Change in Resistivity in Magnetoresistive La-Ca-Mn-O. *Science*, 264:413–415, 1994.

[26] E.O. Wollan. Neutron Diffraction Study of the Magnetic Properties of the Series of Perovskite-Type Compounds $La_{1-x}Ca_xMnO_3$. *Physical Review*, 100(2):545–563, 1955.

[27] H.U. Anderson. Review of p-type doped perovskite materials for sofc and other applications. *Solid State Ionics*, 52(1-3):33–41, 1992.

[28] A.J. Morelli, A.M. Mance, J.V. Mantese, and A.L. Micheli. Magnetocaloric properties of doped lanthanum manganite films. *Journal of Applied Physics*, 79:373–375, 1996.

[29] V.M. Goldschmidt. Die Gesetze der Krystallochemie. *Naturwissenschaften*, 14:477, 1926.

[30] A.R. Dinesen. *Magnetocaloric and magnetoresistive properties of* $La_{0.67}Ca_{0.33-x}Sr_xMnO_3$. PhD thesis, Technical University of Denmark, 2004.

[31] R.D. Shannon. Revised effective ionic radii and systematic studies of interatomic. *Acta Crystallographica*, 32:751–767, 1976.

[32] A.R. West. *Solid State Chemistry and Its Applications*. Wiley, 1985.

[33] A.R. West. *Basic Solid State Chemistry*. John Wiley and Sons, 1999.

[34] S. Blundell. *Magnetism in condensed matter*. Oxford University Press, 2001.

[35] P. Hedegaard. Magnetism and Magnetic Materials. *Lectures at University of Copenhagen*, 2006.

[36] Ashcroft and Mermin. *Solid State Physics*. Saunders College Publishing, 1976.

[37] K. Yosida. *Theory of Magnetism*. Springer-Verlag, 1996.

[38] J.M.D. Coey, M. Viret, and S. Von Molnar. Mixed-valence manganites. *Advances in Physics*, 48:167–293, 1999.

[39] G.H. Jonker and J.H. Van Santen. Ferromagnetic compunds of manganese with perovskite structure. *Physica*, 16, 1950.

[40] C. Zener. Interaction between the d-shells in the transition metals. *Physical Review*, 81:440–444, 1951.

[41] P.W. Anderson and H. Hasegawa. Considerations on double exchange. *Physical Review*, 100:675–681, 1953.

[42] J.B. Goodenough. Theory of the Role of Covalence in the Perovskite-Type Manganites. *Physical Review*, 100(2):564–573, 1955.

[43] H.Y. Chen, C. Lin, and D.S. Dai. Magnetocaloric effect in $(La,R)_{2/3}Ca_{1/3}MnO_3$ (R = Gd, Dy, Tb, Ce). *Journal of Magnetism and Magnetic Materials*, 257(2-3):254–257, 2003.

[44] A.R. Dinesen, S. Linderoth, and S. Mørup. Direct and indirect measurement of the magnetocaloric effect in $La_{0.67}Ca_{0.33-x}Sr_xMnO_3$. *Journal of Physics-Condensed Matter*, 17(39):6257–6269, 2005.

[45] H. Gencer, S. Atalay, H.I. Adiguzel, and V.S. Kolat. Magnetocaloric effect in the $La_{0.62}Bi_{0.05}Ca_{0.33}MnO_3$ compound. *Physica B-Condensed Matter*, 357(3-4):326–333, 2005.

[46] N.V. Dai, N.C. Thuan, L.V. Hong, and N.X. Phuc. Magnetoresistance effect in $La_{0.7}Sr_{0.3}MnO_3$ thin films fabricated by using pulsed laser deposition. *Journal of the Korean Physical Society*, 52(5):1452–1455, 2008.

[47] J.S. Park, K.K. Yu, H.K. Lee, H.R. Bae, Y.P. Lee, and V.G. Prokhorov. Magnetic inhomogeneity in $La_{0.7}Ca_{0.3}MnO_3$ films with structural disorder. *Journal of the Korean Physical Society*, 46:8201–8204, 2005.

[48] K.A. Gschneidner and V.K. Pecharsky. Magnetic refrigeration materials (invited). *Journal of Applied Physics*, 85(8):5365–5368, 1999.

[49] K.A. Gschneidner, V.K. Pecharsky, A.O. Pecharsky, and C.B. Zimm. Recent developments in magnetic refrigeration. *Rare Earths '98*, 315-3:69–76, 1999.

[50] Y. Xu, M. Meier, P. Das, M.R. Koblischka, and U. Hartmann. Perovskite manganites: potential materials for magnetic cooling at. *Crystal Engineering*, 5(3-4):383–389, 2002.

[51] S.V. Trukhanov, I.O. Troyanchuk, A.V. Trukhanov, I.A. Bobrikov, V.G. Simkin, and A.M. Balagurov. Concentration-dependent structural transition in the $La_{0.7}Sr_{0.3}MnO_{3-\delta}$ system. *Jetp Letters*, 84(5):254–257, 2006.

[52] M.H. Phan, S.C. Yu, N.H. Hur, and Y.H. Jeong. Large magnetocaloric effect in a $La_{0.7}Ca_{0.3}MnO_3$ single crystal. *Journal of Applied Physics*, 96(2):1154–1158, 2004.

[53] X.D. Liu, Z.K. Jiao, K. Nakamura, T. Hatano, and Y.W. Zeng. The grain size dependence of the resistance behaviors in doped lanthanum manganite polycrystalline films. *Journal of Applied Physics*, 87(5):2431–2436, 2000.

[54] J.P. Holman. *Heat Transfer*. McGraw-Hill, 1986.

[55] L.A. Chick, L.R. Pederson, G.D. Maupin, J.L. Bates, L.E. Thomas, and G.J. Exarhos. Glycine Nitrate Combustion Synthesis of Oxide Ceramic Powders. *Mat.Lett.*, 10(1-2):6–12, 1990.

[56] J. Als-Nielsen and D. McMorrow. *Elements of Modern X-ray Physics*. John Wiley & Sons Ltd., 2001.

[57] S.J. Hibble, S.P. Cooper, A.C Hannon, I.D. Fawcett, and M. Greenblatt. Local distortions in the collosal magnetoresistive manganates. *Journal of Physics : Condensed Matter*, 11:9221–9238, 1999.

[58] H.M. Rietveld. Line profiles of neutron powder-diffraction peaks for structure refinement. *Acta Crystallographica A*, 22:151–152, 1967.

[59] H.M. Rietveld. A profile refinement method for nuclear and magnetic structures. *Journal of Applied Crystallography*, 2:65:196, 1969.

[60] J. Rodriguez-Carvajal. Recent advances in magnetic structure determination by neutron powder diffraction. *Physica B*, 192:55–69, 1992.

[61] R.A. Young, editor. *The Rietveld Method*. Oxford University Press, 1995.

[62] S. Foner. Versatile and Sensitive vibrating-sample magnetometer. *Review of Scientific Instruments*, 30:548–57, 1959.

[63] A. Szewczyk, M.U. Gutowska, K. Piotrowski, M. Gutowski, M.T. Borowiec, V.P. Dyakonov, V.L. Kovarskii, H. Szymczak, and L. Gladczuk. Specific heat and the cooperative Jahn-Teller effect. *J.Phys.- Cond.Mat.*, 10(47):10539–10548, 1998.

[64] R.D. McMichael, J.J. Ritter, and R.D. Shull. Enhanced magnetocaloric effect in GdGaFeO. *Journal of Applied Physics*, 73:6946, 1993.

[65] S.Y. Dankov, Y.I. Spichkin, and A.M. Tishin. Magnetic entropy and phase transitions in Gd, Tb, Dy and Ho. *Journal of Magnetism and Magnetic Materials*, 152(1-2):208–212, 1996.

[66] M. Foldeaki, R. Chahine, and T.K. Bose. Magnetic Measurements - A Powerful Tool in Magnetic Refrigerator. *Journal of Applied Physics*, 77(7):3528–3537, 1995.

[67] A.R. Dinesen, S. Linderoth, and S. Mørup. Direct and indirect measurement of the magnetocaloric effect in a. *Journal of Magnetism and Magnetic Materials*, 253(1-2):28–34, 2002.

[68] S. Jeppesen, S. Linderoth, N. Pryds, L. Theil Kuhn, and J. Buch Jensen. Indirect measurement of the magnetocaloric effect using a novel differential scanning calorimeter with apllied magnetic field. *Review of Scientific Instruments*, 79(8):083901, 2008.

[69] M. Kuepferling, C.P. Sasso, V. Basso, and L. Giudici. An isothermal Peltier cell calorimeter for measuring the magnetocaloric. *IEEE Trans.Magn.*, 43(6):2764–2766, 2007.

[70] A. Szewczyk, M. Gutowska, B. Dabrowski, T. Plackowski, N.P. Danilova, and Y.P. Gaidukov. Specific heat anomalies in $La_{1-x}Sr_xMnO_3$ ($0.12 \leq x \leq 0.2$). *Physical Review B*, 71(22):–, 2005.

[71] G.W.H Höhne, W.F. Hemminger, and H.J. Flammersheim. *Differential Scanning Calorimetry*, volume Second Edition. Springer-Verlag, 2003.

[72] G.T. Furukawa, W.G. Saba, and M.L. Reilly. Critical Analysis of the Heat Capacity Data of the Literature and. Technical report, NIST, 1968.

[73] K.J. Chau, K.M. Rieckmann, and A.Y. Elezzabi. Subsurface probing of terahertz particle plasmons. *Appl.Phys.Lett.*, 90(13):131114–, 2007.

[74] NIST. Standard Reference Materials. Technical report, National Institute of Standards and Technology, 2005.

[75] M.H. Phan and S.C. Yu. Review of the magnetocaloric effect in manganite materials. *Journal of Magnetism and Magnetic Materials*, 308(2):325–340, 2007.

[76] M.H. Phan, H.X. Peng, S.C. Yu, N.D. Tho, and N. Chau. Large magnetic entropy change in Cu-doped manganites. *Journal of Magnetism and Magnetic Materials*, 285(1-2):199–203, 2005.

[77] A.I. Tovstolytkin, A.N. Pogorilyi, E.V. Shypil, and D.I. Podyalovski. An abnormal effect of low level Cu doping on the magnetism and conductivity of $La_{0.7}Ca_{0.3}MnO_{3-\delta}$. *Physics of Metals and Metallography*, 91:S214–S218, 2001.

[78] S.A. Sergeenkov, H. Bougrine, M. Ausloos, and R. Cloots. A sharp decrease of resistivity in $La_{0.7}Ca_{0.3}Mn_{0.96}Cu_{0.04}O_3$: Evidence for Cu-assisted coherent tunneling of spin polarons. *JETP Letters*, 69(11):858–862, 1999.

[79] S. Sergeenkov, M. Ausloos, H. Bougrine, A. Rulmont, and R. Cloots. Anomalous temperature behavior of the resistivity in lightly doped manganites around a metal-insulator phase transition. *Jetp Letters*, 70(7):481–487, 1999.

[80] E. Dagotto, T. Hotta, and A. Moreo. Colossal magnetoresistant materials: the key role of phase separation. *Physics Reports*, 344(1-3):1–153, 2001.

[81] P.H. Larsen. Personal communication. 2007.

[82] J. Blasco, J. Garcia, J.M. Teresa, M.R. Ibarra, P.A. Algarabel, and C. Marquina. A systematic study of structural, magnetic and electrical properties of (image) perovskites. *Journal of Physics: Condensed Matter*, 8(40):7427–7442, 1996.

[83] M.C. Sanchez, J. Blasco, J. Garcia, J. Stankiewicz, J.M. De-Teresa, and M.R. Ibarra. Study of structural, magnetic, and electrical properties of $La_{(2/3)}Ca_{(1/3)}Mn_{(1-x)}In_{(x)}O_3$ perovskites. *J. Solid State Chem.*, 138:226, 1998.

[84] M.S. Kim, J.B. Yang, J. Medvedeva, W.B. Yelon, P.E. Parris, and W.J. James. Electronic structure of $La_{0.7}Sr_{0.3}Mn_{1-x}Cu_xO_3$. *Journal of Physics-Condensed Matter*, 20(25), 2008.

[85] M. S. Kim, J. B. Yang, P. E. Parris, Q. Cai, X. D. Zhou, W. J. James, W. B. Yelon, D. Buddhikot, and S. K. Malik. The effect of Cu-doping on the magnetic and transport properties of $La_{0.7}Sr_{0.3}MnO_3$. *49th Annual Conference on Magnetism and Magnetic Materials*, 97(10), 2005.

[86] C.L. Yuan, Y. Zhu, and P.P. Ong. The effects of Cu doping on the magnetoresistive behavior of perovskites $La_{0.7}Ca_{0.3}MnO_3$. *Solid State Communications*, 120(12):495–499, 2001.

[87] S. Hirosiwa, H. Tomizawa, and R. Kogure. Magnetic alloy material and method of making the magnetic alloy material. United States Patent 0231163 Al, 2006.

[88] Z.M. Wang, G. Ni, Q.Y. Xu, H. Sang, and Y.W. Du. Magnetocaloric effect in perovskite manganites $La_{0.7-x}Nd_xCa_{0.3}MnO_3$. *Journal of Applied Physics*, 90(11):5689–5691, 2001.

[89] MolyCorp. www.molycorp.com/data_sheets/lanthanum/5210.htm, 2008.

[90] Tianjiao. http://www.baotou.com/cp/cp.htm, 2008.

[91] P. Srivastava, O.N. Srivastava, H.K. Singh, and P.K. Siwach. Synthesis and magnetotransport properties of Mm-doped $La_{0.7}Ca_{0.3}MnO_3$. *Journal of Alloys and Compounds*, 459(1-2):61–65, 2008.

[92] J.E. Gayone, M. Abbate, G. Alejandro, D.G. Lamas, M. Tovar, and G. Zampieri. Ce valence in $La_{0.47}Ce_{0.20}Ca_{0.33}MnO_3$. *Journal of Alloys and Compounds*, 369(1-2):252–255, 2004.

[93] L Sudheendra and CNR Rao. Electronic phase separation in the rare-earth manganates $(La_{1-x}Ln_x)_{0.7}Ca_{0.3}MnO_3$ (Ln = Nd, Gd and Y). *Journal of Physics Condensed Matter*, 15(19):3029–3040, 2003.

[94] J. Philip and T.R.N. Kutty. Effect of valence fluctuations in A sites on the transport properties of $La_{1-x}R_xMnO_3$ (R = Ce, Pr). *Journal of Physics: Condensed Matter*, 11(43):8537–8546, 1999.

Risø DTU